Large Eddy Simulation and Wavelet Analysis of the Flow Field around a Surface Mounted Prism

Mohamed Aly Khamis Elsayed

Dissertation submitted to the Faculty of the
Virginia Polytechnic Institute and State University
in partial fulfillment of the requirements for the degree of

Doctor of Philosophy

in

Engineering Mechanics

Dr. Saad A. Ragab, Co-Chair
Dr. Muhammad R. Hajj, Co-Chair
Dr. Henry W. Tieleman
Dr. Yuriko Renardy
Dr. Surot Thangjitham
Dr. Ziyad N. Masoud

May, 2005
Blacksburg, Virginia

Keywords: Wind Loads, Large eddy simulation, Peak pressures, Wavelet analysis, Bicoherence

Large Eddy Simulation and Wavelet Analysis of the Flow Field around a Surface Mounted Prism

Mohamed Aly Khamis Elsayed

(ABSTRACT)

Unsteady large-scale vortices, formed by the roll-up of free shear layers separating along sharp edges, are the dominant flow characteristics of the turbulent flow over buildings. These vortical structures interact with each other and with the building surface resulting in secondary separation and severe pressure fluctuations. Moreover, the interaction of the large-scale vortices with the multiplicity of turbulence scales in the incoming wind exacerbates their unsteady motion and hence significantly affects the pressure fluctuations spectra experienced by the building.

Large-eddy simulations are conducted to study the interaction of homogeneous turbulence in the incident flow with a surface-mounted prism. A compact fifth-order upwind difference scheme is used to effectively and accurately perform the simulations. Three cases of incident flow are considered. In one case, the prism is placed in a smooth uniform flow. In the second case, homogeneous isotropic turbulence with von Karman spectrum is superimposed on the uniform flow at the inflow boundary. The integral length scale is one-half the prism height. In the third case, the integral length scale is equal to the prism height.

The numerical results are compared with experimental measurements reported by Tieleman et al. [11]. The results show that the highest negative mean value of the pressure coefficient on the roof and the sides is about 30% larger in case two of turbulent inflow and takes place closer to the windward edge of the prism. Moreover, the pressure coefficients on the roof and sides of the prism in the case of turbulent inflow show a higher level of variations in comparison with the case of smooth inflow conditions. The predicted mean characteristics of the pressure coefficients in the turbulent case match the experimental values in terms of both magnitude and location on the roof of the prism reported in Tieleman et al. [38] and Tieleman

et al. [11]. As for the peak value, the peak value of -2 obtained in the turbulent inflow case two is about 20% smaller than the values measured experimentally by Tieleman et al. [11]. On the other hand, it is stressed that the peak value in the simulations would increase as the duration of the simulation is increased to match that of the experimental measurement. The results also show that the turbulent case yields a non-exceedence probability for the peak pressure coefficient that is closer to the one obtained from the measured data than the smooth case data.

Also, spectral and cross-spectral analysis are carried out using complex Morlet wavelet transform to investigate pressure-velocity relation. The study shows that the nonlinearity in the relationship of velocity-pressure is detected using wavelet bicoherence.

Acknowledgements

I would like to thank both Dr. Hajj and Dr. Ragab for their continued support during my PhD work at Virginia Tech. Their guidance and encouragment helped me conduct this study.

I would like also to thank my commitee members Dr. Tieleman, Dr. Renardy, Dr. Thangjitham, and Dr. Masoud for their encouragement and constructive comments.

Finally I would like to thank my wife and my parents because they have offered support in many different aspects throughout my study.

Contents

List of Figures

List of Tables

Chapter 1

Introduction

1.1 Motivation

The complex characteristics of the flow field over structures makes the prediction of peak values for wind loads extremely difficult. Consequently, design codes such as ASCE 7-02 are based on several simplifications. For instance, design values for the pressure coefficients are obtained from wind tunnel measurements that are assumed to simulate open terrain conditions. Gust effects are accounted for by a 3-second gust ratio of probable maximum speed to hourly mean speed. Peak values in a suburban terrain are obtained from open terrain values through a multiplication by the ratio of the square of their respective mean wind speeds. There are several issues that need to be addressed when making these and other simplifications. In setting the wind tunnel simulation procedures of wind loads, the ASCE code refers to the necessity of modeling the relevant macro and micro length scales of the longitudinal component of the atmospheric turbulence and of minimizing the Reynolds number effects. Yet, recent experimental evidence shows that the turbulence level in the lateral component significantly affects the peak value of pressure coefficients. Moreover, there is no physical background for the 3-second duration, the value of the ratio used for this duration or for the ratio used to relate peak values in different terrains.

The simplifications presented above and issues raised vis-a-vis these simplifications are all related to the effects of turbulence in the incident flow on extreme wind loads on structures. Consequently, there is a need to establish procedures that allow for the simulation of turbulence in different exposure categories or terrains and that would not truncate the effects of turbulence to simple ratios or factors. To this end, recent advances made in computational power, technologies and methodolgies allow for the development of numerical codes capable of predicting the dynamic characteristics of wind loads on structures under different incident flow conditions. Numerical simulation of a complex turbulent flow such wind flow over a structure is indeed a challenge. The high Reynolds numbers typical of wind engineering applications makes it difficult to resolve all of the dynamic scales, from the largest scales imposed by the size of the building or incident flow to the smallest dissipative scales.

Resolving all of the dynamic scales in a turbulent flow is known as direct numerical simulation (DNS), which is presently not feasible for wind engineering applications because of the disparity between the large and small scales. This disparity increases with increasing the Reynolds number. Techniques such as Reynolds-average Navier-Stokes (RANS) solvers that model all the turbulent scales and only compute the slowly varying components of the motion, are inadequate for wind engineering applications. This is because there is no clear separation in the frequency domain between what is turbulent and what might constitute an unsteady phase-averaged motion. Furthermore, turbulence models for RANS are notoriously difficult to derive and their performance is always questionable for unsteady turbulent flows.

Since the basic dynamics of the turbulent flow around buildings is contained in large-scale vortices and shear layers instabilities, it is essential that all large-scale motions are accurately resolved and one may use a turbulence model to account for the effects of the small scales. This is the basic idea of Large eddy simulation (LES). LES can be used very effectively to simulate turbulent flows over buildings and address issues related to the effects of the turbulence scales of the incoming flow on the surface pressure fluctuations. In LES, turbulence modeling is required only for eddies (scales) not resolvable by the computational grid. Small-scale eddies are less dependent on the flow geometry. Hence, sub-grid scale (SGS)

turbulence models are expected to be less complicated than the models for (RANS) solvers where the SGS model accounts for all the scales other than the mean flow. Because of its simplicity, a dynamic-eddy-viscosity model is used in the present work.

1.2 Large Eddy Simulation

Analyzing the complex flow around surface-mounted prisms with different shapes using large eddy simulation has been carried out by many researchers. Dahai and Kareem [1, 2, 3] conducted several LES computations to study the characteristics of the flow field around rectangular prisms. In these studies, finite volume method was used to solve Navier-Stokes equations in the LES framework and subgrid scale viscosity was computed using Smagorinsky closure model. Their results showed that the flow field patterns are sensitive to the stream wise length of the body [1]. Power spectra of the pressure and velocity fluctuations and their probability distributions were also calculated. In another study [2], they compared their results with experimental data. Their results showed good agreement with the experimental results. Based on a parametric investigation to study the flow field around rectangular prisms of different aspect ratios for a Reynolds number of 10^5. They noted that the flow reattachment occurred for prisms with aspect ratios of $1:3$ and $1:4$. In all of these simulations, the incident flow was uniform and did not contain any turbulence.

Kawamoto [4] developed a turbulence model for predicting wind loads on building. In this study, two types of the K-ε-φ model are used. The results showed that the computed mean pressure coefficients using these two models are more accurate in comparison with coefficients computed by K-ε turbulence model. Thomas and Williams [5] carried out LES to analyze the vortex shedding from a cubic obstacle placed in a turbulent wind environment. The results showed that the vortex shedding has an approximate periodicity and the flow in the wake region is highly assymmetric. Furthermore, the results showed, that accurate prediction of the extreme pressure peaks requires additional resolution to capture the small

scale of the vortices near the upstream corner of the roof. Nozawa and Tamura [6] conducted LES to simulate the flow around low-rise buildings. Their results showed that the size of the separation bubble over the roof depends on the strength of turbulence intensities of the incoming flow. Tamura and Ono [7] studied the aeroelastic instability of square and rectangular cylinders using the results from LES. Their study shows that LES was an effective tool in predicting the turbulent effect on the unstable oscillation of two-dimensional prisms and in understanding the physical mechanism of the flow separation around prisms in both cases of including homogeneous turbulence and smooth inflow boundary conditions.

In comparison to the above studies, the large eddy simulations conducted in this work aim at studying the characteristics of the flow field around a low rise building under three different conditions of the incident flow. In the first simulation, the incident flow is uniform and smooth. In the other two simulations, homogeneous turbulence with different integral length scales is introduced in the incident flow. The flow patterns under these different conditions as well as mean, rms and peak pressure coefficients are compared with each other and with experimental results.

1.3 Spectral and Wavelet Analysis

In the analysis of the flow field and associated extreme wind loads on structures, the question remains as to what parameters should be analyzed. This question arises because the dynamic similarity of the full scale Reynolds number is not achievable in wind tunnel or numerical simulations. Moreover, matching all turbulence parameters such as turbulence intensities, integral length scales, small scale parameters and aerodynamic roughness lengths has been shown to be extremely difficult. These difficulties have lead to different approaches regarding the ability to predict pressure fluctuations from the flow field. One of these approaches is the quasi-steady approach whereby the pressure fluctuations are directly related to the incident flow. This approach basically sums the effects of the near flow field into a time varying

coefficient. Several studies have shown that the quasi-steady approach fails to predict the pressure fluctuations. As such, there is a need to establish analysis procedures for wind loads on structures whereby the relation between the velocity fluctuations in the far field and the near field and their contributions to the surface pressure fluctuations can be quantified. Hajj et al.[13] investigated the linear and nonlinear correlations between velocity and pressure fluctuations on a surface mounted prisms. The results revealed that the frequency-domain analysis is not accurate in determining the relation between incident velocity and fluctuating pressures. Tieleman et al.[14] analyzed the velocity-pressure correlation around a surface-mounted prism by computing the nonlinear cross-bicoherence and linear cross-coherence between far-field and near-field velocity fluctuations and surface pressure fluctuations. It was found that the significance of the far-field velocity contributions is limited to the low-frequency range. Hajj et al.[15] applied orthonormal wavelets to velocity records to quantify the percentage of energy contribution of each scale to the total energy. The study shows that the energy of the smaller turbulence scales relative to that of the larger scales have significant effects on mean and peak pressures observed on the top surface of a prism.

In this study, a hierarchy of wavelet-based spectral and cross-spectral moments is used to determine the linear and nonlinear relations between the different components of velocity fluctuations in the flow field and surface pressure fluctuations. The interest in using wavelet analysis arises from the need to analyze transient or intermittent phenomena such as pressure peaks and associated velocity events.

1.4 Objectives

The objectives of the present study can be summarized as follows:

(1) Study the effects of turbulence length scales of an incoming flow on the pressure fluctuations above a surface-mounted prism.

(2) Investigate the pressure-velocity relations using wavelet-based higher order spectral mo-

ments in the flow over prisms.

Chapter 2

Mathematical Model for Large Eddy Simulation

In this chapter, we present the governing equations of the flow field in dimensional and nondimensional forms, the equations for large eddy simulation, and finally, we discuss the subgrid scale model for the momentum and the energy equations.

2.1 Navier-Stokes Equations

Using standard notation, we write the Navier-Stokes equations as:

Continuity Equation:

$$\frac{\partial \rho^*}{\partial t^*} + \frac{\partial (\rho^* u_j^*)}{\partial x_j^*} = 0 \tag{2.1}$$

Momentum Equation:

$$\frac{\partial (\rho^* u_i^*)}{\partial t^*} + \frac{\partial}{\partial x_j^*}(\rho^* u_i^* u_j^* + p^* \delta_{ij}) = \frac{\partial \sigma_{ij}^*}{\partial x_j^*} \tag{2.2}$$

Energy Equation:

$$\frac{\partial(\rho^* E^*)}{\partial t^*} + \frac{\partial}{\partial x_j^*}\left[(\rho^* E^* + p^*)u_j^*\right] = \frac{\partial}{\partial x_j^*}(\sigma_{ij}^*\, u_i^* - q_j^*) \tag{2.3}$$

Equation of State:

$$p^* = \rho^* R^* T^* \tag{2.4}$$

where

$$E^* = \frac{p^*}{(\gamma-1)\rho^*} + \frac{1}{2}u_i^* u_i^* \tag{2.5}$$

$$\sigma_{ij}^* = \mu^*\left(\frac{\partial u_i^*}{\partial x_j^*} + \frac{\partial u_j^*}{\partial x_i^*} - \frac{2}{3}\frac{\partial u_k^*}{\partial x_k^*}\delta_{ij}\right) \tag{2.6}$$

$$q_j^* = -\kappa^*\frac{\partial T^*}{\partial x_j^*} \tag{2.7}$$

2.2 Navier-Stokes Equations in Nondimensional Form

Using the prism height (H^*) and the free stream flow variables as reference values, we define the following dimensionless variables:

$$t = \frac{t^*\, U_\infty^*}{H^*}, \quad x_i = \frac{x_i^*}{H^*}, \quad u_i = \frac{u_i^*}{U_\infty^*}, \quad \rho = \frac{\rho^*}{\rho_\infty^*}, \quad p = \frac{p^*}{\rho_\infty^* {U_\infty^*}^2},$$

$$T = \frac{T^*}{T_\infty^*}, \quad E = \frac{E^*}{{U_\infty^*}^2}, \quad \mu = \frac{\mu^*}{\mu_\infty^*}, \quad \kappa = \frac{\kappa^*}{\kappa_\infty^*}, \quad c_p = \frac{c_p^*}{c_{p_\infty}^*}$$

Using the above dimensionless variables, we rewrite the Navier-Stokes equations in nondimensional form as follows:

Continuity Equation:

$$\frac{\partial \rho}{\partial t} + \frac{\partial(\rho u_j)}{\partial x_j} = 0 \tag{2.8}$$

Momentum Equations:

$$\frac{\partial(\rho u_i)}{\partial t} + \frac{\partial(\rho u_i u_j + p\delta_{ij})}{\partial x_j} = \frac{1}{Re}\frac{\partial \sigma_{ij}}{\partial x_j} \tag{2.9}$$

Energy Equation:

$$\frac{\partial(\rho E)}{\partial t} + \frac{\partial\left[(\rho E + p)\, u_j\right]}{\partial x_j} = \frac{1}{Re}\frac{\partial}{\partial x_j}\left[\sigma_{ij}\; u_i - \frac{1}{Pr\;(\gamma-1)\;M^2}\; q_j\right] \tag{2.10}$$

Equation of State:

$$p = \rho\, R\, T \tag{2.11}$$

where

$$E = \frac{p}{(\gamma-1)\rho} + \frac{1}{2}u_i u_i \tag{2.12}$$

$$\sigma_{ij} = \mu\left(\frac{\partial u_i}{\partial x_j} + \frac{\partial u_j}{\partial x_i} - \frac{2}{3}\frac{\partial u_k}{\partial x_k}\delta_{ij}\right) \tag{2.13}$$

$$q_j = -\kappa\frac{\partial T}{\partial x_j} \tag{2.14}$$

The Reynolds number Re, the Mach number M and the Prandtl number Pr are given by

$$Re = \frac{\rho^*_\infty\; U^*_\infty\; H^*}{\mu^*_\infty} \tag{2.15}$$

$$M = \frac{U^*_\infty}{\sqrt{\gamma R^* T^*_\infty}} \tag{2.16}$$

$$Pr = \frac{\mu^*_\infty\; c^*_{p_\infty}}{\kappa^*_\infty} \tag{2.17}$$

The nondimensional gas constant is given by

$$R = \frac{R^*\, T^*_\infty}{U^{*2}_\infty} = \frac{1}{\gamma M^2} \tag{2.18}$$

Here, we assume that μ and κ are functions of temperature, but we assume that c_p^* to be constant, hence $c_p = 1$.

2.3 Equations For Large Eddy Simulation

The Favre-filtered governing equations for the resolved scales are (see Erlebacher et al. [16] and Ragab and Sheen [17]):

Continuity Equation:

$$\frac{\partial \bar{\rho}}{\partial t} + \frac{\partial (\bar{\rho}\widetilde{u}_j)}{\partial x_j} = 0 \tag{2.19}$$

Momentum Equation:

$$\frac{\partial (\bar{\rho}\widetilde{u}_i)}{\partial t} + \frac{\partial (\bar{\rho}\widetilde{u}_i\widetilde{u}_j + \bar{p}\delta_{ij})}{\partial x_j} = \frac{1}{Re}\frac{\partial \widetilde{\sigma}_{ij}}{\partial x_j} - \frac{\partial \tau_{ij}}{\partial x_j} \tag{2.20}$$

Energy Equation:

$$\begin{aligned}\frac{\partial (\bar{\rho}\widetilde{E})}{\partial t} + \frac{\partial [(\bar{\rho}\widetilde{E} + \bar{p})\widetilde{u}_j]}{\partial x_j} = \frac{1}{Re}\frac{\partial}{\partial x_j}\left[\widetilde{\sigma}_{ij}\widetilde{u}_i - \frac{1}{Pr\,(\gamma-1)\,M^2}\,\widetilde{q}_j\right] \\ - \frac{\partial}{\partial x_j}\left[c_p \mathcal{Q}_j\right]\end{aligned} \tag{2.21}$$

Equation of State:

$$\bar{p} = \bar{\rho}\, R\, \widetilde{T} \tag{2.22}$$

where

$$\widetilde{E} = \frac{\bar{p}}{(\gamma-1)\bar{\rho}} + \frac{1}{2}\widetilde{u}_i\widetilde{u}_i \tag{2.23}$$

$$\widetilde{\sigma}_{ij} = \widetilde{\mu}\left(\frac{\partial \widetilde{u}_i}{\partial x_j} + \frac{\partial \widetilde{u}_j}{\partial x_i} - \frac{2}{3}\frac{\partial \widetilde{u}_k}{\partial x_k}\delta_{ij}\right) \tag{2.24}$$

$$\widetilde{q}_j = -\widetilde{\kappa}\,\frac{\partial \widetilde{T}}{\partial x_j} \tag{2.25}$$

$$\tau_{ij} = \bar{\rho}\left(\widetilde{u_i u_j} - \widetilde{u}_i \widetilde{u}_j\right) \tag{2.26}$$

$$\mathcal{Q}_j = \bar{\rho}\left(\widetilde{u_j T} - \widetilde{u}_j \widetilde{T}\right) \tag{2.27}$$

Here τ_{ij}, and $\mathcal{Q}_j$ represent the SGS (subgrid scale) stress tensor and heat flux, respectively. These terms need to be modeled in order to close the system of equations.

2.4 Subgrid-scale Model

There is only one unclosed term in the momentum equation, i.e., the SGS stress τ_{ij}. The dynamic version of the Smagorinsky's eddy-viscosity model [18] introduced by Germano *et al.* [19] is used to model the SGS stress. The model is

$$\tau_{ij} - \frac{1}{3}\tau_{kk}\delta_{ij} = -2C\bar{\rho}\bar{\Delta}^2\left|\widetilde{S}\right|\left(\widetilde{S}_{ij} - \frac{1}{3}\widetilde{S}_{kk}\delta_{ij}\right) \tag{2.28}$$

where

$$\widetilde{S}_{ij} = \frac{1}{2}\left(\frac{\partial \widetilde{u}_i}{\partial x_j} + \frac{\partial \widetilde{u}_j}{\partial x_i}\right), \tag{2.29}$$

$$\left|\widetilde{S}\right| = \left(2\widetilde{S}_{ij}\widetilde{S}_{ij}\right)^{\frac{1}{2}}, \tag{2.30}$$

$$\bar{\Delta} = \left(\Delta_1\,\Delta_2\,\Delta_3\right)^{\frac{1}{3}}, \tag{2.31}$$

$$\widehat{\Delta} = (\widehat{\Delta}_1\,\widehat{\Delta}_2\,\widehat{\Delta}_3)^{\frac{1}{3}}. \tag{2.32}$$

Here C is the Smagorinsky coefficient that is assumed to be independent of filter width. In the present study, $\widehat{\Delta}_i = 2\bar{\Delta}_i$ is used, where $(\widehat{\ })$ implies test filtering.

We let

$$\mathcal{L}_{ij} = \widehat{\bar{\rho}\,\widetilde{u}_i\,\widetilde{u}_j} - \frac{\widehat{\bar{\rho}\,\widetilde{u}_i}\;\widehat{\bar{\rho}\,\widetilde{u}_j}}{\widehat{\bar{\rho}}}\ , \tag{2.33}$$

$$\mathcal{M}_{ij} = -2\widehat{\Delta}^2\widehat{\bar{\rho}}|\widehat{\widetilde{S}}|\widehat{\widetilde{S}^d_{ij}} + 2\bar{\Delta}^2\widehat{\bar{\rho}|\widetilde{S}|\widetilde{S}^d_{ij}}\ , \tag{2.34}$$

$$\widehat{\widetilde{S}^d_{ij}} = \widehat{\widetilde{S}}_{ij} - \frac{1}{3}\widehat{\widetilde{S}}_{kk}\delta_{ij}\ , \tag{2.35}$$

$$\widetilde{S}^d_{ij} = \widetilde{S}_{ij} - \frac{1}{3}\widetilde{S}_{kk}\delta_{ij}\ . \tag{2.36}$$

Then Smagorinsky coefficient is given by

$$C = \frac{\left(\mathcal{L}_{ij} - \frac{1}{3}\mathcal{L}_{kk}\delta_{ij}\right)\mathcal{M}_{ij}}{\mathcal{M}_{ij}\mathcal{M}_{ij}} \tag{2.37}$$

To avoid the large fluctuations in the values of C that may cause instability of numerical solutions, we follow Zhang and Chen [22] and determine C as follows:

$$C = \frac{\widehat{\overline{\mathcal{L}^d_{ij}}\,\overline{\mathcal{M}_{ij}}}}{\widehat{\overline{\mathcal{M}_{ij}}\,\overline{\mathcal{M}_{ij}}}}, \qquad \mathcal{L}^d_{ij} = \mathcal{L}_{ij} - \frac{1}{3}\mathcal{L}_{kk}\delta_{ij} \tag{2.38}$$

where the symbol $\widehat{=}$ represents double filtering, i.e., a grid filter $(\bar{\ })$ is applied first followed by a test filter $(\widehat{\ })$.

The unclosed term in the total energy equation is the SGS heat flux $\mathcal{Q}_j$.

Using the Smagorinsky's eddy-diffusivity model, $\mathcal{Q}_j$ is modeled as

$$\mathcal{Q}_j = \frac{\bar{\rho}\nu_T}{Pr_T}\frac{\partial \widetilde{T}}{\partial x_j} = -C\frac{\Delta^2 \bar{\rho}\,|\widetilde{S}|}{Pr_T}\frac{\partial \widetilde{T}}{\partial x_j} \tag{2.39}$$

where C is the eddy-viscosity coefficient given by Equation (2.38) and Pr_T is the turbulent Prandtl number. Here, we assume $Pr_T = 0.7$.

Chapter 3

Numerical Method and Boundary Conditions

Our approach is based on solving the grid-filtered compressible Navier-Stokes equations at low Mach numbers. The sub-grid scale turbulence is modelled by a dynamic Smagorinsky eddy viscosity model. Our LES code uses a low dissipation fifth-order compact finite-difference scheme in space [28] and a fourth order Runge-Kutta integration for time stepping [29]. It also uses non-reflecting boundary conditions at inflow and characteristic boundary conditions at outflow. We developed a method for generating divergence-free isotropic turbulence with control over its integral length scale and its 3D energy spectrum.

3.1 Temporal Discretization

Consider the model equation

$$\frac{dq}{dt} = L(q) \tag{3.1}$$

where q is a flow variable, t is time and L is a spatial operator. The five-stage fourth-order

explicit Runge-Kutta scheme [29] is used to advance the solution in time. To advance the solution from step n to $n+1$, we use the algorithm

$$q^0 = q^n \tag{3.2}$$

$$H^0 = L(q^0) \tag{3.3}$$

Then for $m = 1, ..., 4$, we use

$$q^m = q^{m-1} + b^m \Delta t H^{m-1} \tag{3.4}$$

$$H^m \leftarrow q^m + a^m H^{m-1} \tag{3.5}$$

and for the final step, we use

$$q^5 = q^4 + b^5 H^4 \tag{3.6}$$

$$q^{n+1} = q^5 \tag{3.7}$$

Table 3.1 gives the values of a^m while Table 3.2 gives the values of b^m.

3.2 Space Discretization

3.2.1 Compact Upwind Difference (CUD) Scheme

We consider the x-operator of the Euler equations

m	a^m
1	-0.41789047
2	-1.19215169
3	-1.69778469
4	-1.51418344

Table 3.1: The a^m coefficients of fourth-order Runge-Kutta scheme [29]

m	b^m
1	0.14965902
2	0.37921031
3	0.82295502
4	0.69945045
5	0.15305724

Table 3.2: The b^m coefficients of fourth-order Runge-Kutta scheme [29]

$$\frac{\partial q}{\partial t} + \frac{\partial F(q)}{\partial x} = 0 \tag{3.8}$$

where $q = (\rho, \rho u, \rho v, \rho w, \rho E)^T$ is the vector of conservative variables, and

$$F(q) = \left\{ \begin{array}{l} \rho u \\ \rho u^2 + p \\ \rho uv \\ \rho uw \\ (\rho E + p)u \end{array} \right\} \tag{3.9}$$

is the flux vector. To apply an upwind scheme we split the flux,

$$F = F^+ + F^- \tag{3.10}$$

We used Lax-Friedrichs (LF) flux vector splitting in the form

$$F^{\pm} = \frac{1}{2} \left[F(q) \pm C_5 \lambda q \right] \tag{3.11}$$

where $\lambda = |u| + a$, and C_5 is an arbitrary constant that controls the level of artificial dissipation and its value is greater than zero. Similar expressions are used for the y- and z-fluxes. The first derivative is approximated by Tolstykh's [28] CUD-II-5 scheme

$$(\frac{\partial F}{\partial x})_j \approx (\frac{\delta^+ F^+}{\delta x})_j + (\frac{\delta^- F^-}{\delta x})_j \tag{3.12}$$

where

$$(\frac{\delta^{\pm}}{\delta x})_j = \frac{1}{\Delta x} \left[\Delta(s) + \frac{s}{2} R^{-1} Q (I + \frac{1}{12} \Delta_2)^{-1} \Delta_2 \right] \tag{3.13}$$

$$\Delta(s) = \frac{1}{2}(\Delta_0 - s\Delta_2) \tag{3.14}$$

$$\Delta_0 F_j = F_{j+1} - F_{j-1} \tag{3.15}$$

$$\Delta_2 F_j = F_{j+1} - 2F_j + F_{j-1} \tag{3.16}$$

The operators R and Q are

$$R = I + (\frac{(1/5s)}{2} - \frac{s_1}{4})\Delta_0 + (\frac{1}{6} - \frac{(1/5s)}{2})\Delta_2 \tag{3.17}$$

$$Q = I + (\frac{(-2/15s)}{2} - \frac{s_1}{4})\Delta_0 + (\frac{1}{6} - \frac{(-2/15s)}{2})\Delta_2 \tag{3.18}$$

where $s = 2\sqrt{5}$ and s_1/s is a positive constant, here we use $s_1/s = 0.75$. Tolstykh [28] proved that, for a scalar equation,

$$\frac{\delta^+ F^+}{\delta x} + \frac{\delta^- F^-}{\delta x} = (\frac{\partial F}{\partial x})_j - \frac{|s|}{2} C_5 B \lambda (\Delta x)^5 \frac{\partial^6 q}{\partial x^6} \tag{3.19}$$

where λ is assumed to be constant and

$$B = \frac{\sqrt{5}}{288} + \frac{1}{720} \tag{3.20}$$

Hence, the leading term in the truncation error is of fifth-order and it is proportional to C_5. We control the level of artificial damping by adjusting the value of C_5. Results presented in this dissertation are obtained with $C_5 = 0.5$, which is the minimum value that resulted in stable solution.

3.3 Algorithm and Numerical Boundary Conditions

The first derivative of the flux at grid point i is approximated by

$$(\frac{\partial F}{\partial x})_i = \frac{1}{\Delta x}(\hat{F}_{i+\frac{1}{2}} - \hat{F}_{i-\frac{1}{2}}) \tag{3.21}$$

where

$$\hat{F}_{i+\frac{1}{2}} = \frac{\hat{F}_{i+1} + \hat{F}_i}{2} - \frac{s}{2}\left[(I - R^{-1}Q(I + \frac{\Delta_2}{12})^{-1})\right](\hat{F}_{i+1} - \hat{F}_i) \tag{3.22}$$

The algorithm for computing Equation (3.22) is as follows:

(i) Solve tri-diagonal system for v_i

$$(I + \frac{\Delta_2}{12})v_i = \hat{F}_{i+1} - \hat{F}_i, \qquad i = 1, ...N - 1 \tag{3.23}$$

(ii) Solve tri-diagonal system for w_i

$$Rw_i = Qv_i \tag{3.24}$$

(iii) Finally compute

$$\hat{F}_{i+\frac{1}{2}} = 0.5(\hat{F}_{i+1} + \hat{F}_i) - 0.5s(\hat{F}_{i+1} - \hat{F}_i - w_i) \tag{3.25}$$

For programming purpose, we write Equation (3.21) as

$$(\frac{\partial F}{\partial x})_i = \frac{1}{\Delta x}(\hat{F}_i - \hat{F}_{i-1}), \qquad i = 1, ...N \tag{3.26}$$

Flow variables q_i are defined at grid points i=1,...,N. The points i=0 and i=N+1 are ghost points introduced for computational purposes.

Algorithm for $\hat{F}_i$, i=0,1,...,N. The algorithm is applicable to both F^+ and F^-, hence we let $F = F^{\pm}$

(1) Compute $F_i = F^{\pm}(q_i)$, i=1,...,N. We extrapolate the flux to the points i=0 and i=N+1 by fifth-order polynomials at points i=1 and i=N.

$$F = a_0 + a_1 x + a_2 x^2 + a_3 x^3 + a_4 x^4 + a_5 x^5 \tag{3.27}$$

The coefficients a_0,...,a_5 can be determined in terms of F_1,...,F_6, and the extrapolated F_0 is.

$$F_0 = 6F_1 - 15F_2 + 20F_3 - 15F_4 + 6F_5 - F_6 \tag{3.28}$$

We also compute the first and second derivatives at point $i = 1$ using the same fifth-order polynomial. This gives a fifth-order one-sided difference for $F_1^{'}$ and fourth-order one-sided difference for $F_1^{''}$.

$$\Delta x F_1^{'} = -\frac{137}{60}F_1 + 5F_2 - 5F_3 + \frac{10}{3}F_4 - \frac{5}{4}F_5 + \frac{1}{5}F_6 \tag{3.29}$$

$$(\Delta x)^2 F_1^{''} = 45F_1 - 154F_2 + 214F_3 - 156F_4 + 61F_5 - 10F_6 \tag{3.30}$$

Similarly, at point i=N

$$F = a_0 + a_1 x + a_2 x^2 + a_3 x^3 + a_4 x^4 + a_5 x^5 \tag{3.31}$$

$$F_{N+1} = 6F_N - 15F_{N-1} + 20F_{N-2} - 15F_{N-3} + 6F_{N-4} - F_{N-5} \tag{3.32}$$

$$\Delta x F_N^{'} = \frac{137}{60}F_N - 5F_{N-1} + 5F_{N-2} - \frac{10}{3}F_{N-3} + \frac{5}{4}F_{N-4} - \frac{1}{5}F_{N-5} \tag{3.33}$$

$$(\Delta x)^2 F_N^{''} = 45F_N - 154F_{N-1} + 214F_{N-2} - 156F_{N-3} + 61F_{N-4} - 10F_{N-5} \tag{3.34}$$

(2) Solve tridiagonal system for v_i, i=1,...,N-1

For i=1, the algorithm takes the form

$$v_i + \frac{1}{12}(v_{i+1} - 2v_i + v_{i-1}) = F_{i+1} - F_i \tag{3.35}$$

hence,

$$v_1 + \frac{1}{12}(v_2 - 2v_1 + v_o) = F_2 - F_1 \tag{3.36}$$

We eliminate v_o by interpreting the difference $v_1 - v_o$ as the second derivative at i=1.

$$v_1 - v_o = (\Delta x)^2 F_1'' \tag{3.37}$$

F_1'' is the second derivative at i=1, it must be of fourth order in Δx.

$$\frac{11}{12}v_1 + \frac{1}{12}v_2 = F_2 - F_1 + \frac{1}{12}(\Delta x)^2 F_1'' \tag{3.38}$$

Equation (3.38) is the first equation in the tri-diagonal system for v_i where $(\Delta x)^2 F_1''$ is given by Equation (3.30)

At i=N-1, the algorithm gives

$$v_{N-1} + \frac{1}{12}(v_N - 2v_{N-1} + v_{N-2}) = F_N - F_{N-1} \tag{3.39}$$

We eliminate v_N by interpreting the difference $v_N - v_{N-1}$ as the second derivative at i=N.

$$v_N - v_{N-1} = (\Delta x)^2 F_N'' \tag{3.40}$$

$$\frac{11}{12}v_{N-1} + \frac{1}{12}v_{N-2} = F_N - F_{N-1} - \frac{1}{12}h^2 F_N'' \tag{3.41}$$

Equation (3.41) is the N^{th} equation in the tri-diagonal system for v_i where $(\Delta x)^2 F_N''$ is given by Equation (3.34)

After solving the tridiagonal system for v_i i=1,...,N-1, we determine v_o and v_N by

$$v_0 = v_1 - (\Delta x)^2 F_1'' \tag{3.42}$$

and

$$v_N = v_{N-1} + (\Delta x)^2 F_N'' \tag{3.43}$$

Hence, we have v_i for i=0,1,...,N

(3) Next We compute Qv_i using Equation (3.18)

$$Qv_i = \left[I + (\frac{a_1}{2} - \frac{s_1}{4})\Delta_0 + (\frac{1}{6} - \frac{a_1}{2}s_1)\Delta_2 \right] v_i \tag{3.44}$$

for i=1,...,N-1

where

$$\Delta_0 f_i = f_{i+1} - f_{i-1} \tag{3.45}$$

$$\Delta_2 f_i = f_{i+1} - 2f_i + f_{i-1} \tag{3.46}$$

$$a_1 = -\frac{2}{15s} \tag{3.47}$$

$$b_1 = \frac{1}{5s} \tag{3.48}$$

Thus, we write Equation (3.44) as

$$Qv_i = c_1 v_{i-1} + c_2 v_i + c_3 v_{i+1} \tag{3.49}$$

where

$$c_1 = \frac{1}{6} + \frac{s_1}{4} + \frac{1+s_1}{15s} \tag{3.50}$$

$$c_2 = \frac{2}{3} - \frac{2s_1}{15s} \tag{3.51}$$

$$c_3 = \frac{1}{6} - \frac{s_1}{4} - \frac{1-s_1}{15s} \tag{3.52}$$

(4) Next we solve tri-diagonal system for w_i:

$$Rw_i = Qv_i \tag{3.53}$$

for i=1,...,N-1

$$bw_{i-1} + dw_i + uw_{i+1} = Qv_i \tag{3.54}$$

i=2,...,N-2

for i=1, we have

$$bw_0 + dw_1 + uw_2 = Qv_1 \tag{3.55}$$

To eliminate w_0, we use

$$\hat{F}_1 - \hat{F}_0 = \Delta x F_1' \tag{3.56}$$

using Equation (3.25) at i=1 and i=0, we rewrite Equation (3.56) as

$$\frac{1}{2}(F_2 + F_1) - \frac{1}{2}s(F_2 - F_1 - w_1) - \frac{1}{2}(F_1 + F_0) + \frac{1}{2}s(F_1 - F_0 - w_0) = (\Delta x)F_1^{'} \tag{3.57}$$

hence, we obtain

$$sw_1 - sw_0 + F_2 - F_0 - s(F_2 - 2F_1 + F_0) = 2\Delta x F_1^{'} \tag{3.58}$$

$$w_1 - w_0 = \frac{1}{s}\left[2\Delta x F_1^{'} - (F_2 - F_0) + s(F_2 - 2F_1 + F_0)\right] \tag{3.59}$$

Multiply by b and add to Equation (3.55)

$$(d + b)w_1 + uw_2 = Qv_1 + \frac{b}{s}\left[2\Delta x F_1^{'} - (F_2 - F_0) + s(F_2 - 2F_1 + F_0)\right] \tag{3.60}$$

This is the first equation in the tri-diagonal system for w_i.

At i=N-1, we have

$$bw_{N-2} + dw_{N-1} + uw_N = Qv_{N-1} \tag{3.61}$$

To eliminate w_N, we use

$$\hat{F}_N - \hat{F}_{N-1} = \Delta x \hat{F}_N \tag{3.62}$$

using Equation (3.25) at i=N and i=N-1, we rewrite Equation (3.62) as

$$\frac{1}{2}(F_{N+1}+F_N) - \frac{1}{2}s(F_{N+1} - F_N - w_N) - \frac{1}{2}(F_N + F_{N-1}) + \frac{1}{2}s(F_N - F_{N-1} - w_{N-1}) = \Delta x F_N^{'} \tag{3.63}$$

$$sw_N - sw_{N-1} + F_{N+1} - F_{N-1} - s(F_{N+1} - 2F_N + F_{N-1}) = 2\Delta x F_N^{'} \tag{3.64}$$

$$w_N - w_{N-1} = \frac{1}{s}\left[2\Delta x F_N^{'} - (F_{N+1} - F_{N-1}) + s(F_{N+1} - 2F_N + F_{N-1})\right] \tag{3.65}$$

Multiplying Equation (3.65) by u and subtracting from Equation (3.61), we obtain

$$bw_{N-2} + (d+u)w_{N-1} = Qv_{N-1} - \frac{u}{s}\left[2\Delta x F_N^{'} - (F_{N+1} - F_{N-1}) + s(F_{N+1} - 2F_N + F_{N-1})\right] \tag{3.66}$$

This is the last equation in the tri-diagonal system for w_i

After we solve for w_i, i=1,...,N-1, we find

$$w_0 = w_1 - \frac{1}{s}\left[2\Delta x F_1^{'} - (F_2 - F_0) + s(F_2 - 2F_1 + F_0)\right] \tag{3.67}$$

and

$$w_N = w_{N-1} + \frac{1}{s}\left[2\Delta x F_N^{'} - (F_{N+1} - F_{N-1}) + s(F_{N+1} - 2F_N + F_{N-1})\right] \tag{3.68}$$

(5) Finally, we compute the numerical flux,

$$\hat{F}_i = \frac{1}{2}(F_{i+1} + F_i) - \frac{1}{2}s(F_{i+1} - F_i - w_i) \tag{3.69}$$

for i=0,1,...,N and hence the flux derivative

$$(\frac{\partial F}{\partial x})_i = \frac{\hat{F}_i - \hat{F}_{i-1}}{\Delta x} \tag{3.70}$$

for i=1,.....N.

3.3.1 Inflow Boundary

At the inflow boundary we specify the three velocity components and temperature. The pressure is extrapolated from inside the domain and density is computed from the equation of state. The computational domain extends from the inflow boundary at $x = -10$ to the outflow boundary at $x = 15$. We recall that the reference length is the prism height. The velocity components at $x = -10$ are prescribed by Fourier series in time

$$u(y,z,t) = 1 + \sum_{n=1}^{N} A_u^n(y,z)cos\omega_n t + B_u^n(y,z)sin\omega_n t \tag{3.71}$$

$$v(y,z,t) = \sum_{n=1}^{N} A_v^n(y,z)cos\omega_n t + B_v^n(y,z)sin\omega_n t \tag{3.72}$$

$$w(y,z,t) = \sum_{n=1}^{N} A_w^n(y,z)cos\omega_n t + B_w^n(y,z)sin\omega_n t \tag{3.73}$$

where the coefficients of the series are functions of y and z. To generate the Fourier coefficients, we first generate a box of isotropic homogeneous turbulence in the wave number space (k_x, k_y, k_z) using a method given by Durbin and Rief [26] (page 241). The 3D energy spectrum function is given by von Karman spectrum [26]

$$E(k) = q^2 L C_{vk} \frac{(kL)^4}{[1 + (kL)^2]^p} \tag{3.74}$$

where $p = \frac{17}{6}$ and

$$C_{vk} = \frac{\Gamma(p)}{\Gamma(\frac{5}{2})\Gamma(p - \frac{5}{2})} = 0.484254 \tag{3.75}$$

where q^2 is twice the turbulence kinetic energy. Here we use $q^2 = 0.0675U_\infty^2$. In the two cases considered with turbulence at the inflow, we use $L = 0.5H$ and H. For $p = \frac{17}{6}$, the

integral length scale $L_{11} \approx (\frac{\pi}{4})L$ ([26] page 244), however, we refer to L as an integral length scale.

Next, we take the inverse Fourier transform in the y and z plane and interpret the wave number in the x-direction as a frequency in time by using Taylor hypothesis, $\omega_n = U_\infty k_{xn}$.

3.3.2 Outflow Boundary

At the outflow boundary, we apply characteristic boundary conditions in the direction normal to the boundary, which is the x-direction. At a point B on the outflow boundary, the characteristic equations of the one-dimensional Euler equations are

$$\Delta u + \frac{\Delta p}{\rho c} = 0 \qquad on \quad C^+ : \frac{dx}{dt} = u + a \tag{3.76}$$

$$\Delta u - \frac{\Delta p}{\rho c} = 0 \qquad on \quad C^- : \frac{dx}{dt} = u - a \tag{3.77}$$

$$\Delta s = 0 \qquad on \quad C^0 : \frac{dx}{dt} = u \tag{3.78}$$

where s is the entropy. Figure 3.1 shows the three characteristic curves in the x-t plane at point B. Points A and C are inside the computational domain, whereas point D is outside. Thus all flow variables are available at points A and C from previous time steps. The characteristic equations give

$$(u_B - u_A) + \frac{1}{\bar{\rho}\bar{a}}(p_B - p_A) = 0 \tag{3.79}$$

$$(u_B - u_D) - \frac{1}{\bar{\rho}\bar{a}}(p_B - p_D) = 0 \tag{3.80}$$

solving for u_B and p_B,we get

$$u_B = \frac{1}{2}(u_A + u_D) + \frac{1}{2\bar{\rho}\bar{a}}(p_A - p_D) \tag{3.81}$$

$$p_B = \frac{1}{2}(p_A + p_D) + \frac{1}{2}\bar{\rho}\bar{a}(u_A - u_D) \tag{3.82}$$

We use the approximations $u_D = U_\infty$, $p_D = p_\infty$, and $\bar{\rho}\bar{a} = \frac{1}{4}(\rho_A + \rho_\infty)(u_A + u_\infty)$, and determine u_B and p_B from the above equations. The density is computed from the entropy equation $s_B = s_C$ hence

$$\rho_B = \rho_C(\frac{p_B}{p_C})^{\frac{1}{\gamma}} \tag{3.83}$$

The temperature is computed from the equation of state

$$T_B = \frac{P_B}{\rho_B R} \tag{3.84}$$

The remaining velocity components v and w are extrapolated along the C^o characteristic, hence

$$v_B = v_C \tag{3.85}$$

$$w_B = w_C \tag{3.86}$$

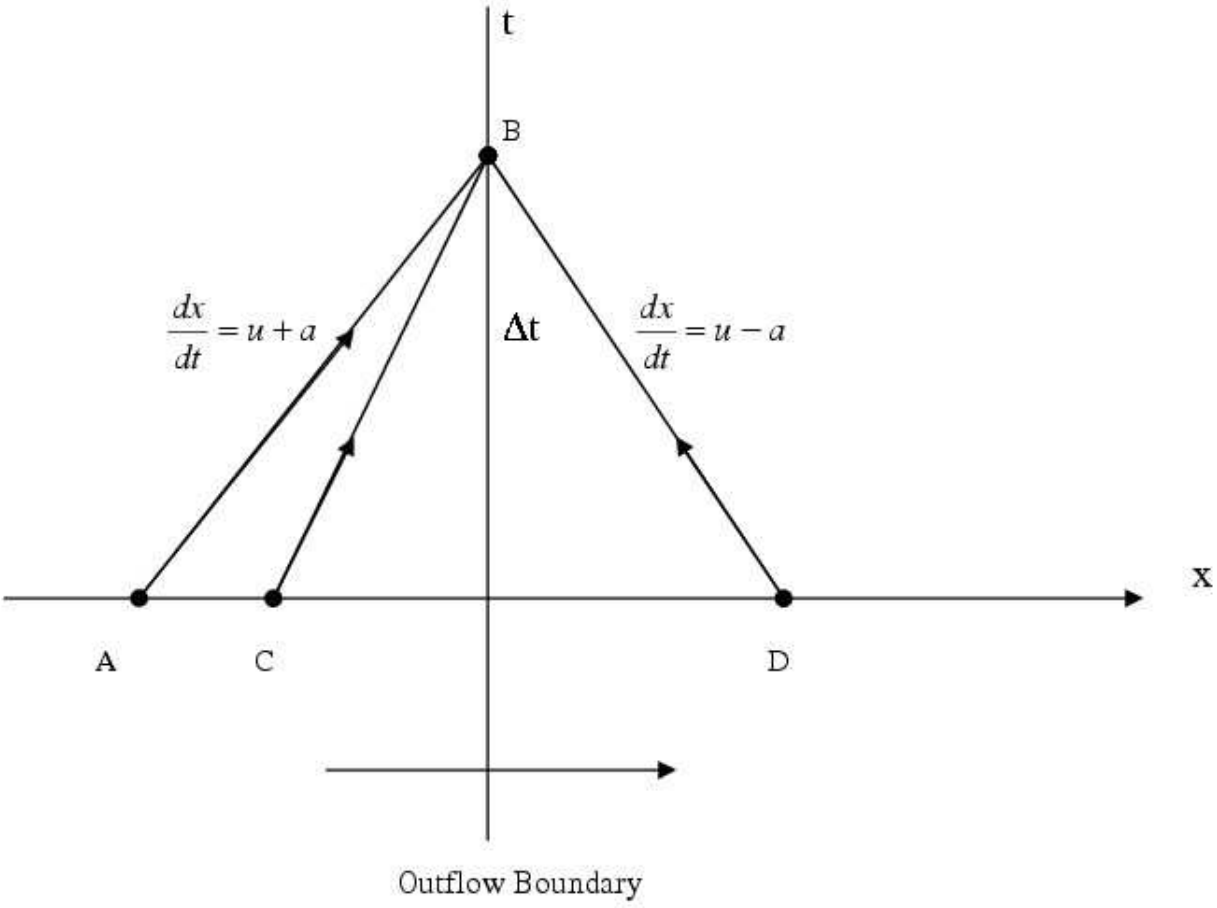

Figure 3.1: Characteristic curves at the outflow boundary condition

Chapter 4

Flow Pattern

In this chapter, we discuss the overall characteristics of the flow pattern. First, we present the instantaneous stream lines and the mean stream lines, then we present the instantaneous vorticity, the mean vorticity, and the 3D-vortex structure.

4.1 Interaction of Homogeneous Turbulence with a Surface Mounted Prism

Our LES code has been validated for standard test cases including:(a) isolated vortices and comparison with exact analytic solutions, (b) comparison with results from hydrodynamic stability (temporal and spatial) theory, (c) Blasius boundary layer, and (d) temporal decaying homogeneous turbulence (see El-okda [30] for more details).

In this section, results of LES of the flow over a surface-mounted prism with the geometric ratios (length/height=3.425 and span/height=2.275) are presented. The prism is placed in a uniform stream in one case, and in a convected homogeneous turbulence that is introduced at the inflow boundary in two cases. The homogeneous turbulence is divergence free and its integral length scale is approximately half of the prism height in one case, while it equals

the prism height in the second case. The 3D energy spectrum is specified by Von Karman spectrum, and turbulence kinetic energy is 0.034 (based on free stream velocity as reference velocity). Taylor hypothesis is used to generate the velocity time series at the inflow by transforming the wave number in one space direction into frequency. The Reynolds number is 30,000 based on prism height, and the Mach number is 0.2. A stretched Cartesian grid of (181x81x101) points is used. The minimum step size next to the solid surface is 0.007.

The velocity field and streamlines in the middle plane are shown for the case of smooth inflow in Figure 4.1a and for the two cases of homogeneous turbulence in Figures 4.1b, and 4.2. The separation region on top of the structure extends beyond the middle of the prism for smooth flow but it is smaller for the case with turbulence. The interaction of the free stream turbulence with the shear layer emanating from the sharp edge accelerates its breakdown, and hence results in sooner reattachement. Also, mean flow velocity for the three cases of smooth inflow and homogeneous turbulence with different integral length scale are given in Figures 4.3a, 4.3b and 4.4, respectively.

A snap shot of the instantaneous vorticity magnitude in the middle plane are shown for the case of smooth inflow in Figure 4.5a, and for homogeneous turbulence (case 1) in Figure 4.5b, while homogeneous turbulence (case 2) is given in Figure 4.6. The free stream turbulence is stretched by the strain field of the prism before it interacts with the free shear layer emanating from the sharp edge. The large scale structures formed by the separation shear layer on top of the prism are more coherent for smooth inflow than for turbulent incoming flow. Mean flow vorticity magnitude for the three cases of smooth inflow and homogeneous turbulence with different integral length scale are given in Figures 4.7a,4.7b, and 4.8 respectively.

Coherent vortical structures are identified by a procedure introduced by Jeong and Hussain [27]. They proposed a definition of a vortex in an incompressible flows in terms of the eigenvalues of the symmetric tensor $s^2+\Omega^2$; here s and Ω are respectively the symmetric and antisymmetric parts of the velocity gradient tensor $\nabla\vec{v}$. If λ_1, λ_2, and λ_3 are the eigenvalues, and $\lambda_1 \geq \lambda_2 \geq \lambda_3$, vortex core is identified by the region where λ_2 is less than zero. Figure

4.9 gives the 3D-vortex plot for the first case of isotropic homogeneous turbulent inflow boundary condition. According to this definition, the coherent structures are the horse-shoe vortex in front of the prism; this vortex interacts with rolled-up shear layers on the prism sides. The rolled-up shear layer on roof of prism breaks up into hair-pin vortices.

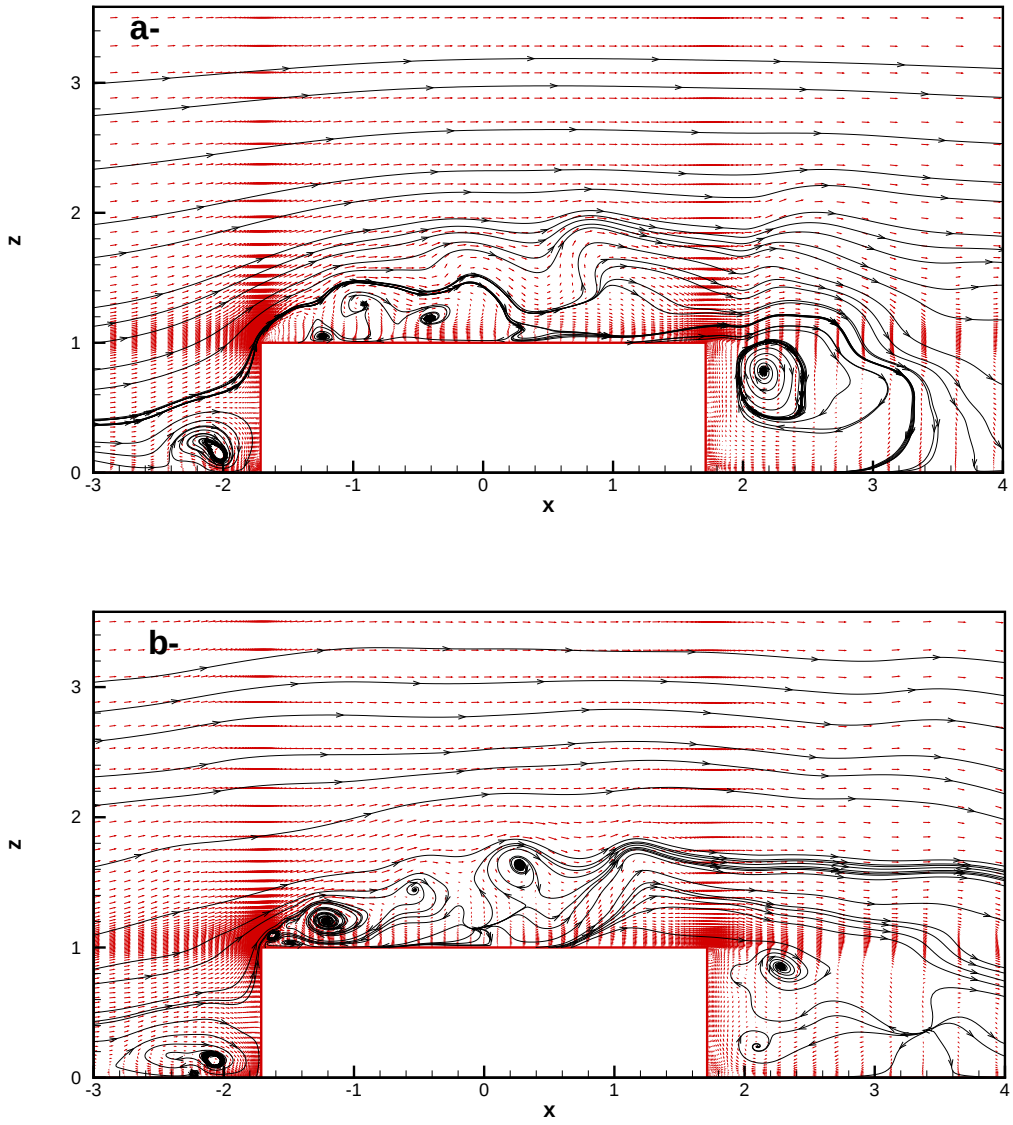

Figure 4.1: Instantaneous velocity, (a) smooth inflow and (b) homogeneous turbulence inflow (case one)

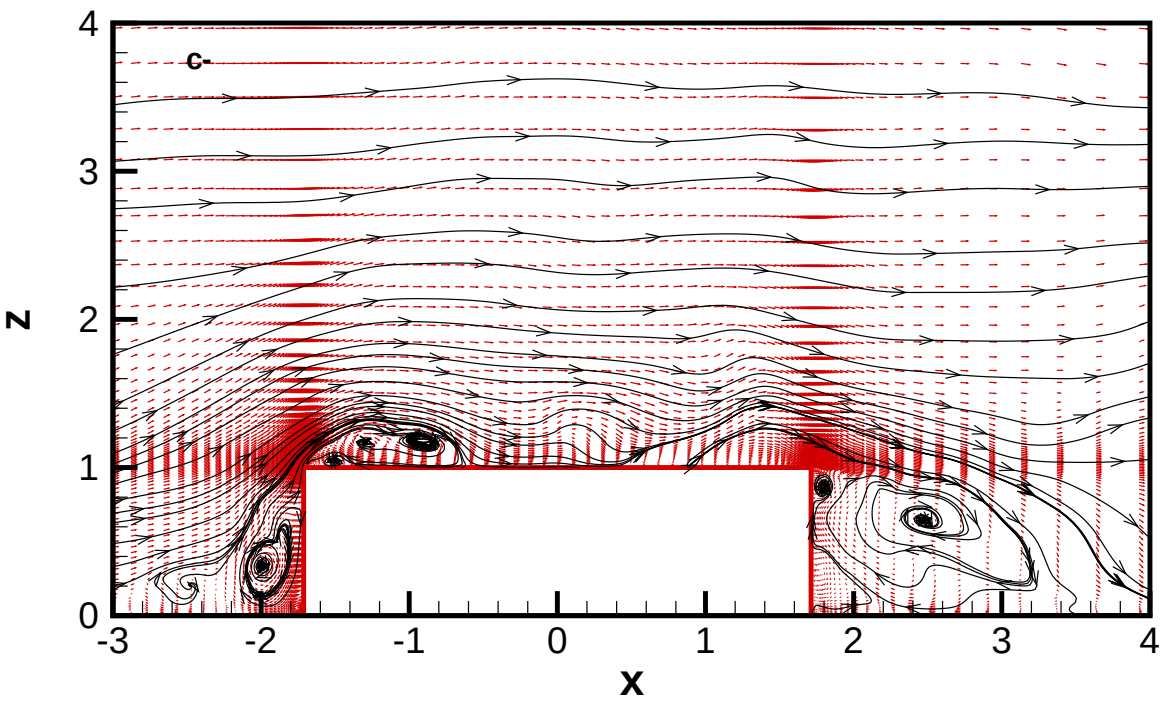

Figure 4.2: Instantaneous velocity for homogeneous turbulence inflow (case two)

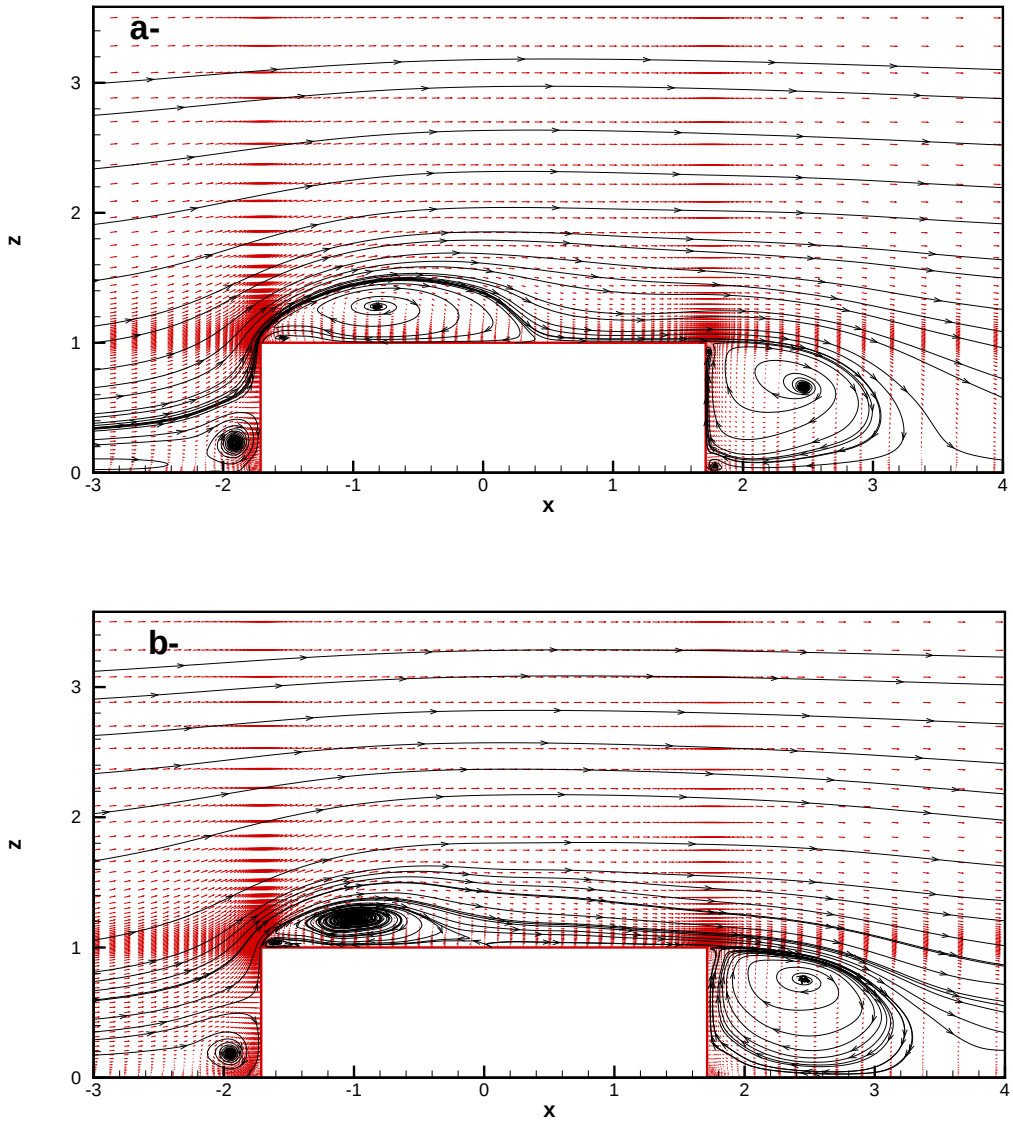

Figure 4.3: Mean velocity, (a) smooth inflow and (b) homogeneous turbulence inflow (case one)

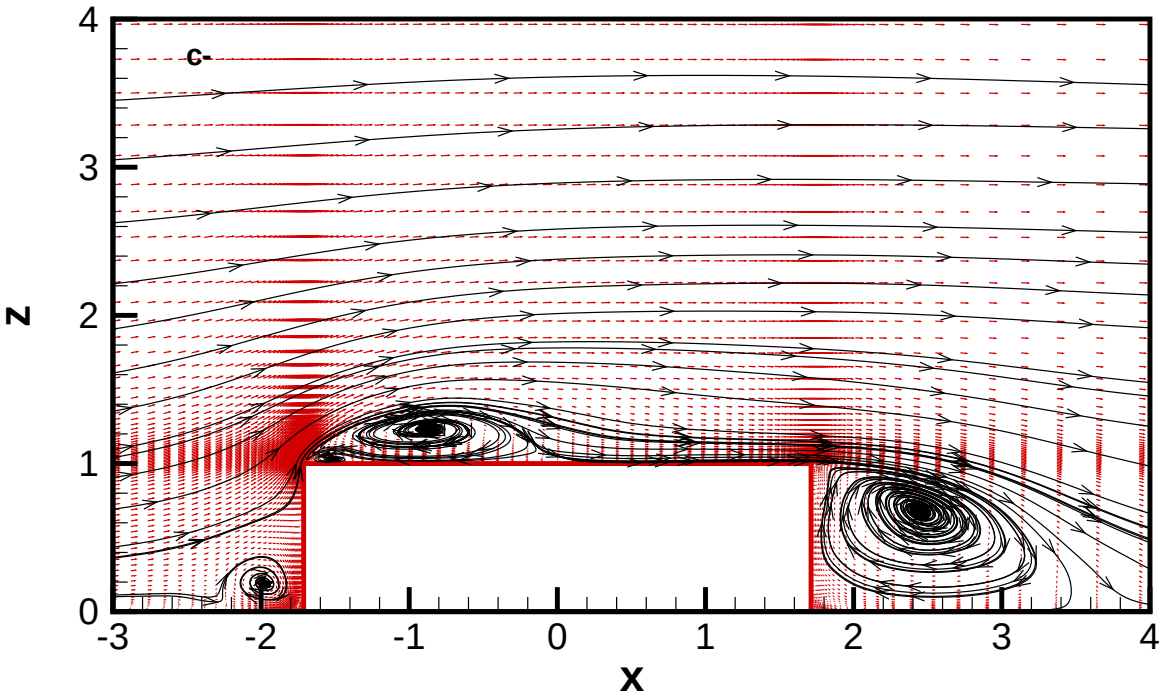

Figure 4.4: Mean velocity for homogeneous turbulence inflow (case two)

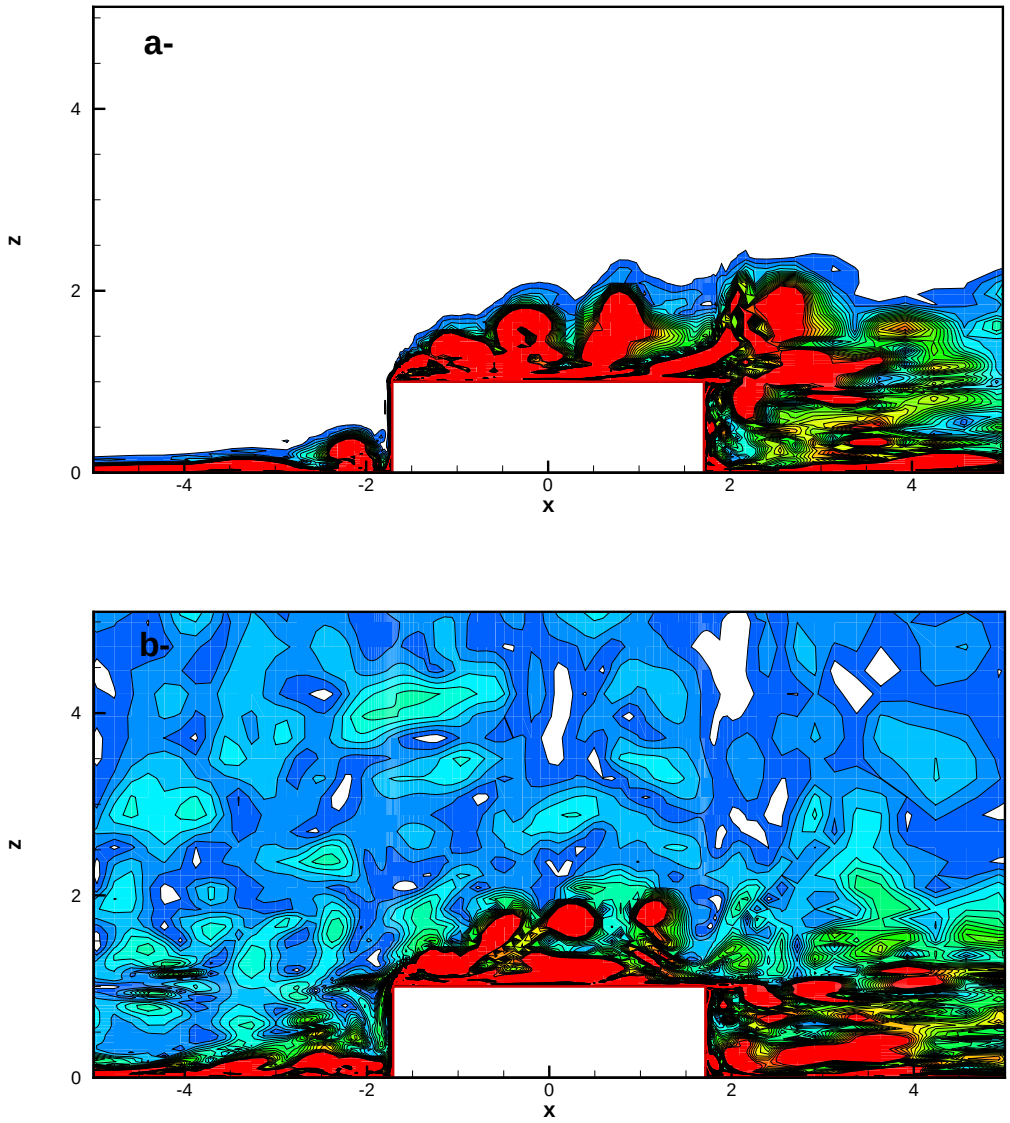

Figure 4.5: Instantaneous vorticity magnitude, (a) smooth inflow and (b) homogeneous turbulence inflow (case one)

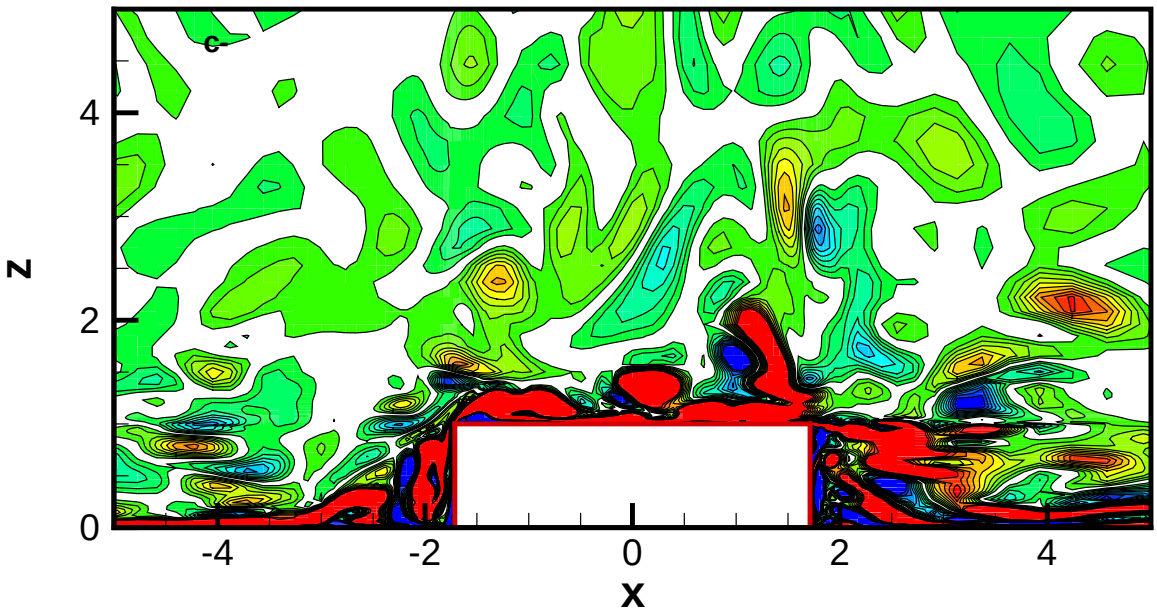

Figure 4.6: Instantaneous vorticity magnitude, homogeneous turbulence inflow (case two)

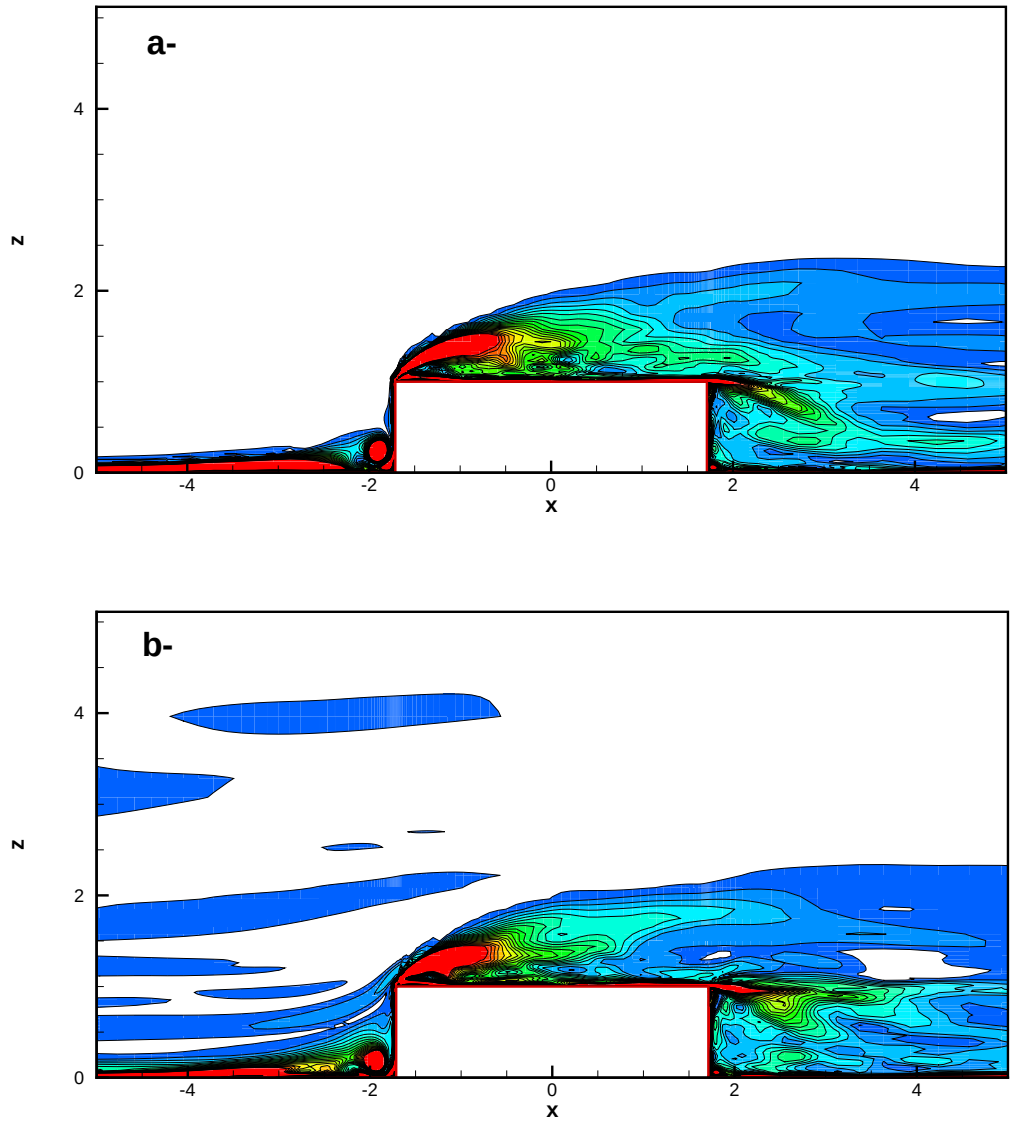

Figure 4.7: Mean flow vorticity magnitude, (a) smooth inflow and (b) homogeneous turbulence inflow (case one)

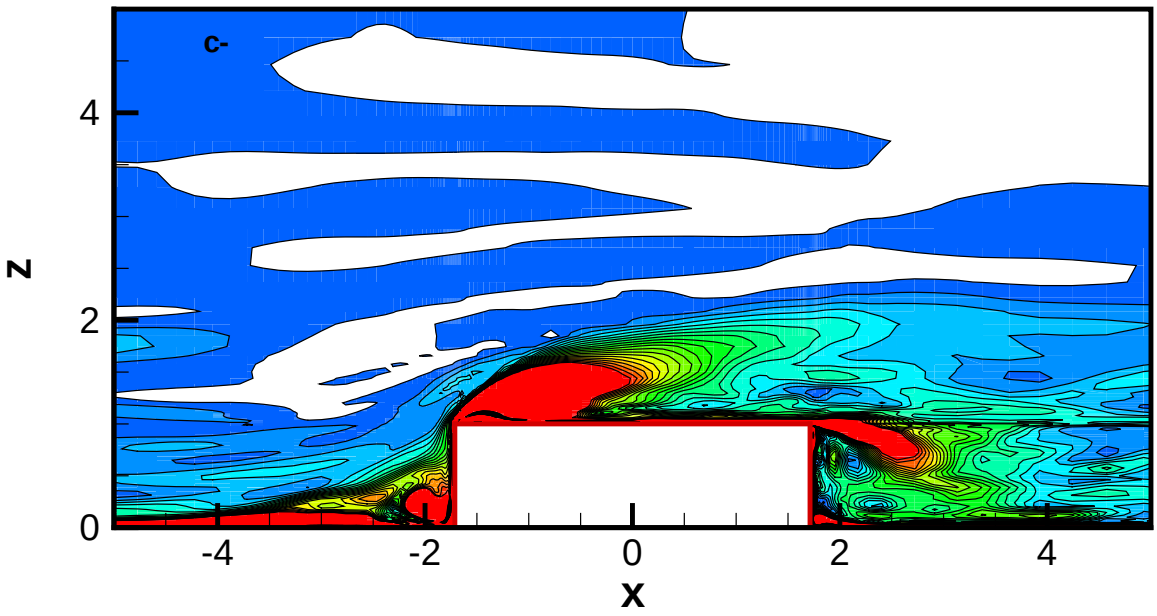

Figure 4.8: Mean flow vorticity magnitude for homogeneous turbulence inflow (case two)

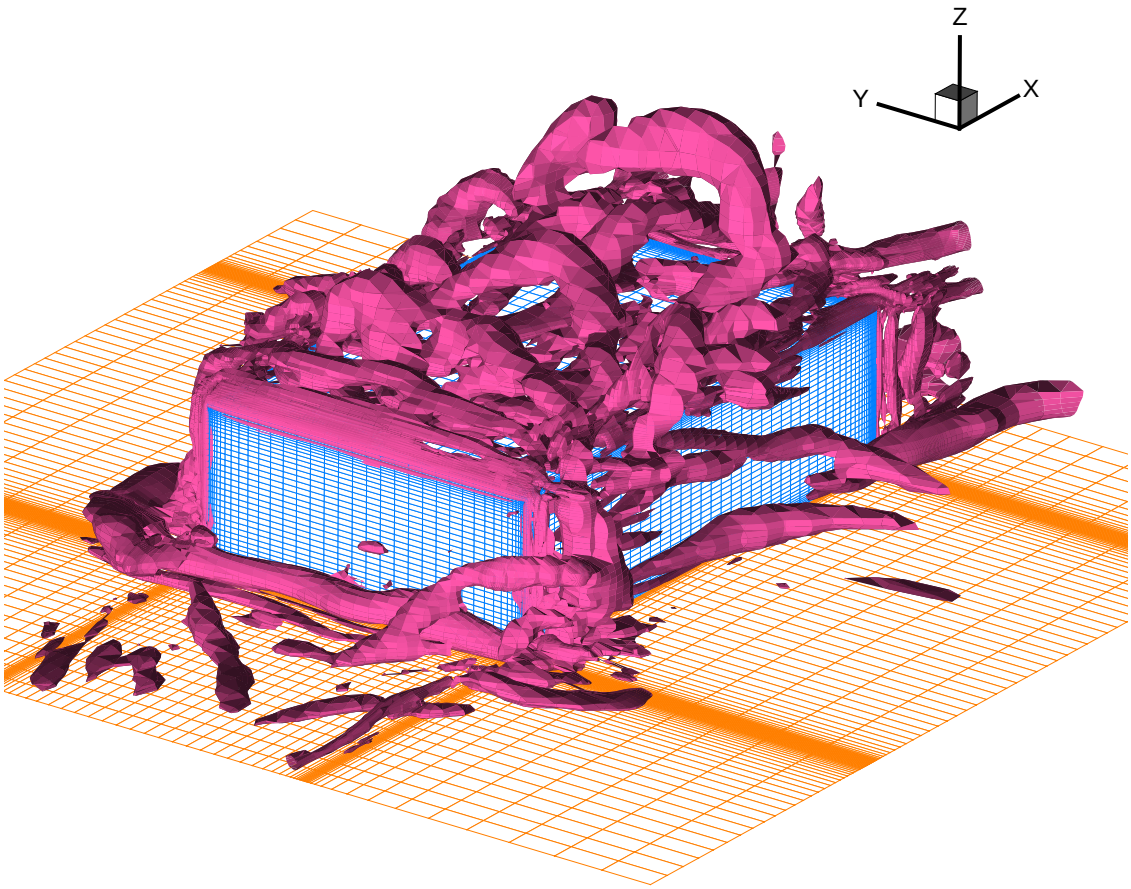

Figure 4.9: Instantaneous coherent structures around a surface-mounted prism

Chapter 5

Surface Pressure Coefficients Under Smooth and Turbulence Inflows

In this chapter, the pressure coefficients on the surface of the prism under two cases of smooth and turbulent inflow conditions are presented. Moreover, the numerical results are compared with experimental measurements reported by Tieleman et al. [11]. The comparison is made on the basis of mean flow characteristics, extreme or peak levels, as well the probability of non-exceedence of these levels. The relation between observed pressure peak and coherent structures in the flow is also discussed.

5.1 Numerical model

The CUD-II-5 scheme, discussed in chapter 3, is used to study the effects of free stream homogeneous turbulence on the flow structure and pressure distribution over a surface-mounted prism. In one case, the prism is placed in a smooth uniform flow, and in another case homogeneous isotropic turbulence with von Karman spectrum is superimposed on the uniform flow at the inflow boundary. The integral length scale of the incoming turbulence

is set at half the prism height, and turbulence intensity at the inflow boundary is set equal to 15% of the mean free stream velocity.

The prism height H, the mean free stream velocity U_∞ and temperature T_∞ are used as reference length, velocity and temperature values. The prism has a length/height ratio of 3.425 and span/height ratio of 2.275. The prism is placed on a flat plate ($z = 0$) with its longer side parallel to the free stream velocity. The Reynolds number Re is 30,000 and the Mach number M_∞ is 0.2. In a Cartesian coordinate system, the bounding surfaces of the prism are $x = \pm 1.7125$, $y = \pm 1.1375$, $z = 0$ and $z = 1$. The computational domain extends from the inflow boundary at $x = -10$ to the outflow boundary at $x = 15$. The spanwise boundaries are at $y = \pm 5$. The no-slip wall condition is assumed at $z = 0$. The free stream boundary condition is assumed at $z = 10$. At the inflow boundary, the velocity and temperature are specified, while the pressure is extrapolated from inside the domain. At the outflow boundary, the transverse velocity components (v and w) and temperature are extrapolated. The pressure and streamwise velocity component u are determined using one-dimensional characteristic boundary conditions. The density is obtained from the equation of state. Symmetry conditions are applied at the spanwise planes $y = \pm 5$. On solid walls, no-slip and adiabatic wall conditions are used.

The computational domain, including the prism, is shown in figure 5.1 with all dimensions scaled with the prism height H. The flow field is divided into non-overlapping rectangular domains. A Cartesian grid is generated in each domain in such a way as to ensure the continuity of the grid Jacobian and its derivatives at the interfaces. This continuity is important to achieve high order accuracy. A nonuniform Cartesian grid of $(161 \times 81 \times 101)$ points is used for smooth oncoming flow and a grid of $(181 \times 81 \times 101)$ is used for turbulent incident flow. The minimum step size next to the solid surface is 0.007 in the $x-$direction and 0.01 in the $y-$ and $z-$directions.

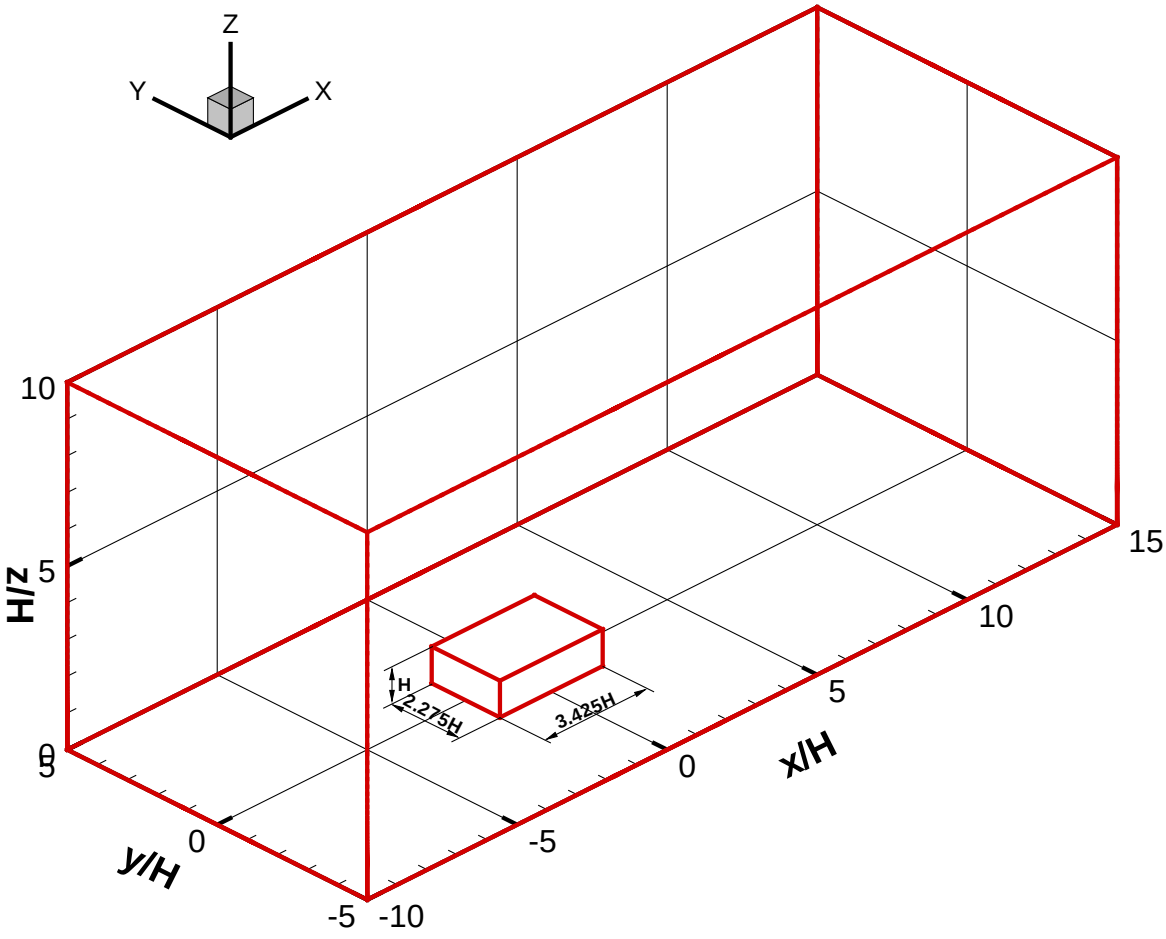

Figure 5.1: Computational domain for surface-mounted prism

5.2 Mean characteristics of surface pressure

Contour plots of the mean pressure coefficients on the roof, side and the upwind and backward faces of the prism in the case of smooth inflow and corresponding plots of vorticity field and coherent vortical structures as defined in section 4.1 over the prism in midplane are presented in figures 5.2, 5.3, and 5.4 respectively. The counterpart plots in the case of

isotropic homogeneous inflow are presented in figures 5.5, 5.6, and 5.7.

A comparison of the pressure coefficients in figures 5.2 and 5.5 shows that, in both cases, the pressure coefficient has a value of one on the upwind face in the stagnation region. On the other hand, the maximum values of the mean pressure coefficient on the roof and sides in the case of isotropic homogeneous turbulent inflow are larger by about 30% than their counterpart values in the case of smooth inflow. The values of mean surface pressure coefficients on the backward side are larger by about 50% in the case of turbulent inflow. In the case of smooth flow, the highest negative mean pressure coefficient on the roof takes place near $x = -1$ which places it at a distance of about $0.7H$ from the windward edge. By comparison, the highest negative peak in the case of turbulent inflow is near $0.4H$ from the windward edge.

The contour plot of the mean vorticity in the case of smooth flow, presented in figure 5.3 shows the separating shear layer and a large area of high level of vorticity in the region $-1 \leq x \leq 0$ and $1 \leq y \leq 1.6$. The plot also shows the secondary separation region that forms between the leading edge of the prism and $x = -1$. A comparison of figures 5.2 and 5.3 shows that the maximum value of the mean pressure coefficient is observed near $x = -1$, which is at the edge between the two separating regions. The contour plot of the mean coherent vortical structures in figure 5.4 shows the basic coherent structures of the mean flow which include, the primary vortex, in front of the prism, a smaller (in size) counter rotating vortex that forms in the corner as a result of the interaction between the primary vortex and the solid walls, the two separating shear layers at the leading corner and the coherent structures in the reattachment and on the backward regions of the prism.

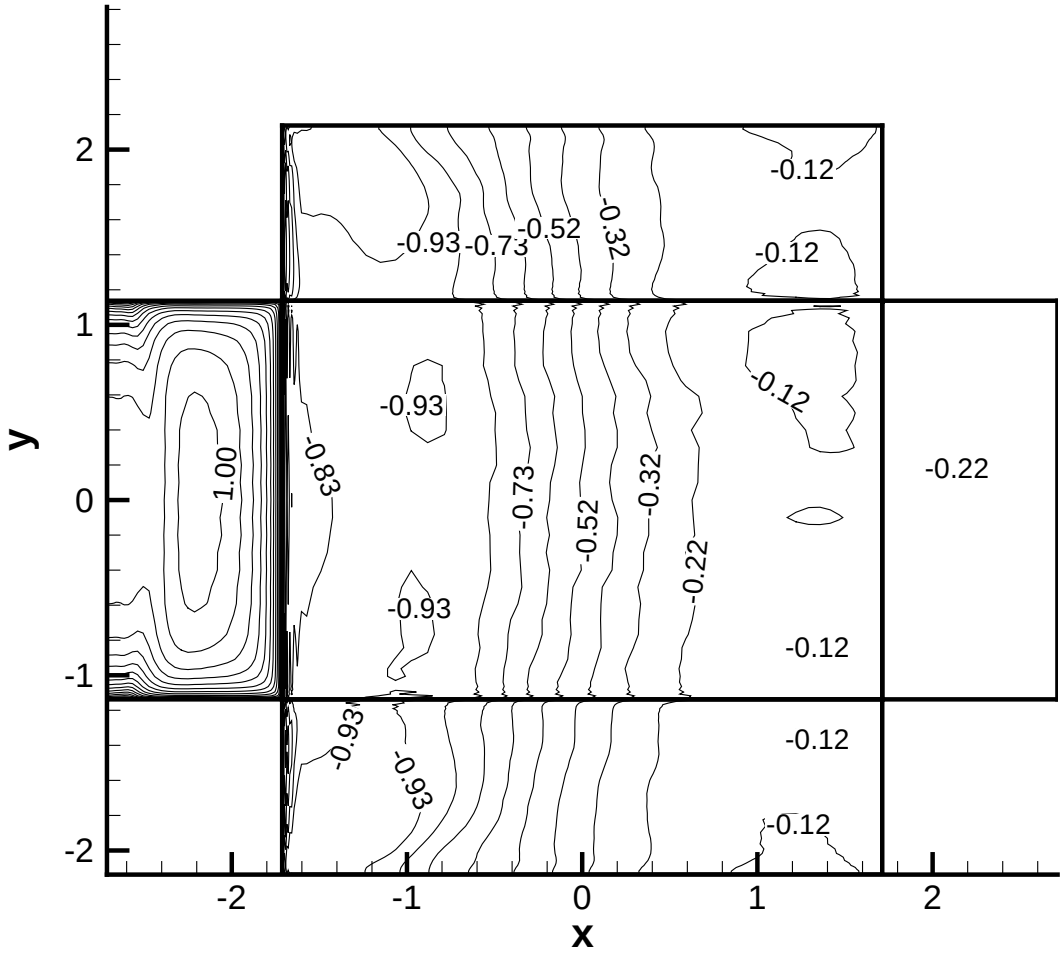

Figure 5.2: Contour plots of mean pressure coefficients on the surface of the prism under smooth inflow conditions

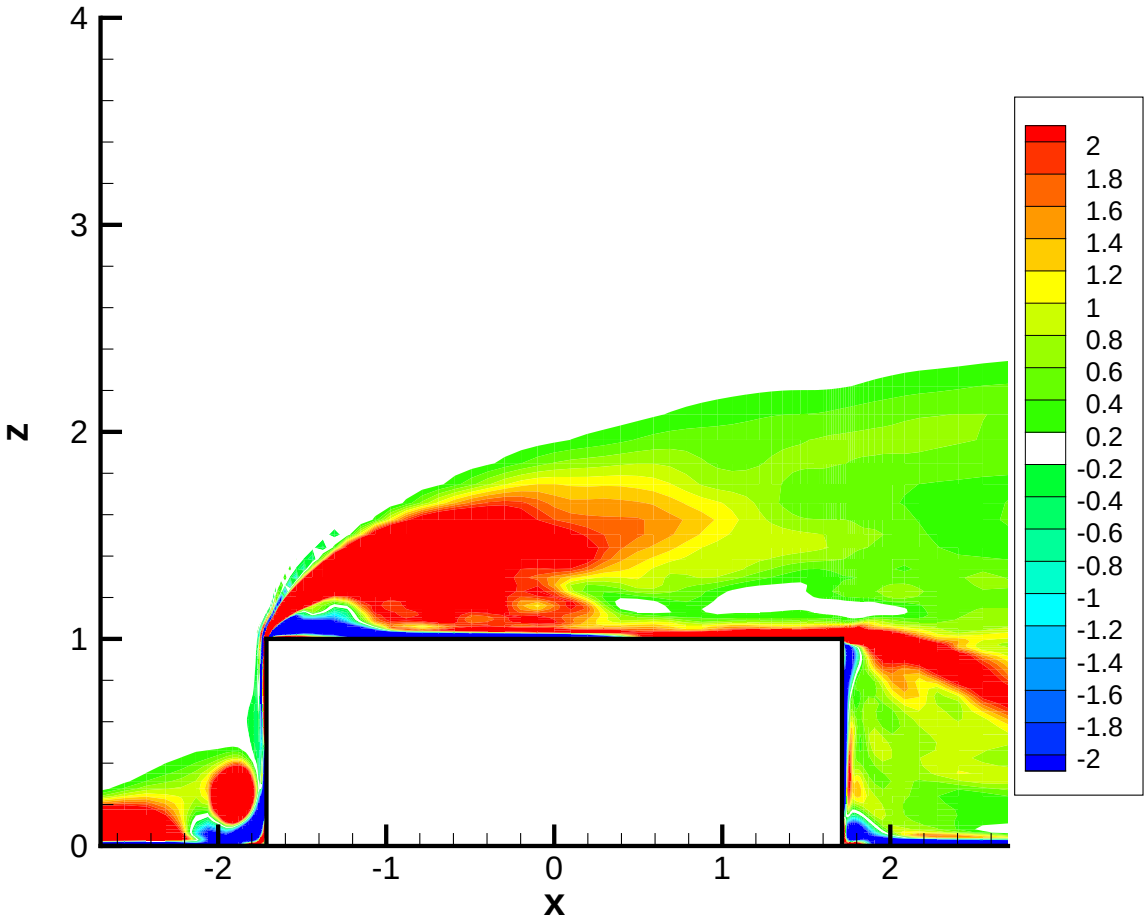

Figure 5.3: Contour plots of mean vorticity under smooth inflow conditions

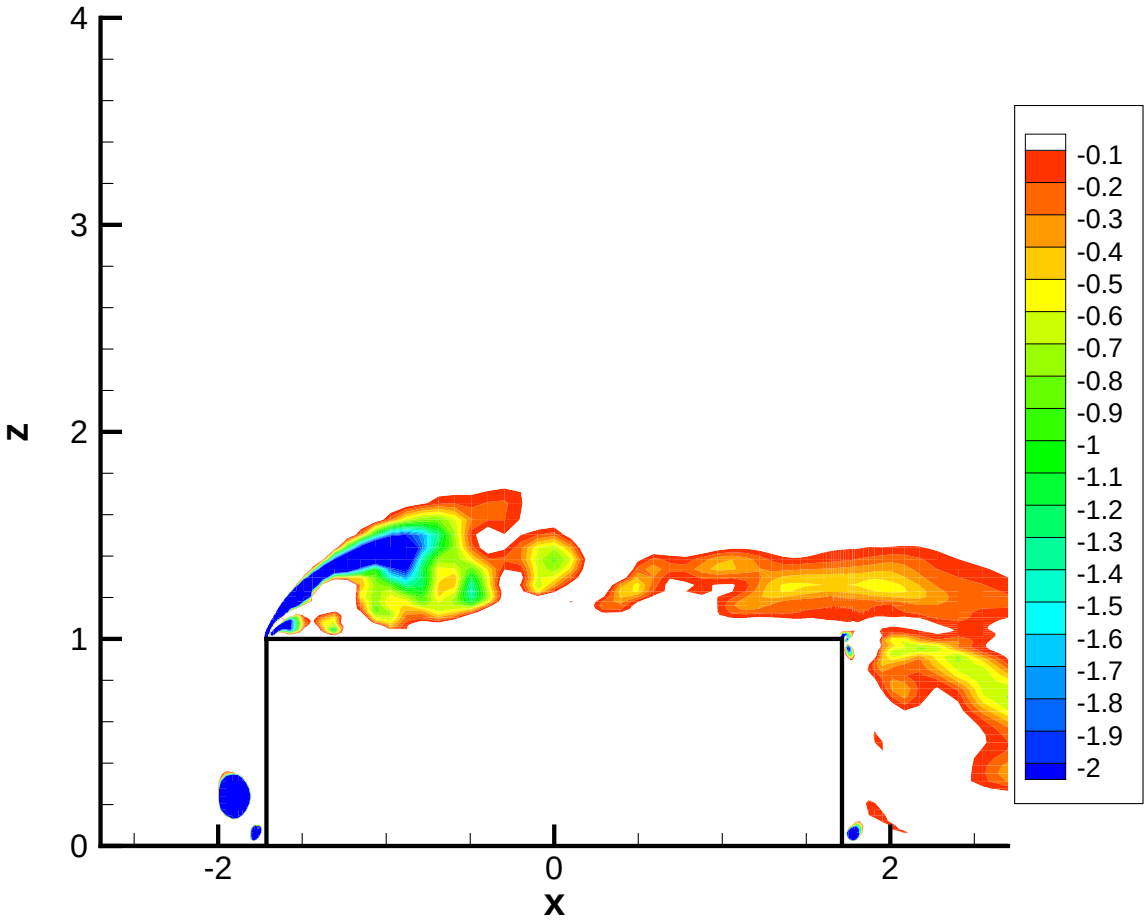

Figure 5.4: Contour plots of mean coherent vortical structures under smooth inflow conditions

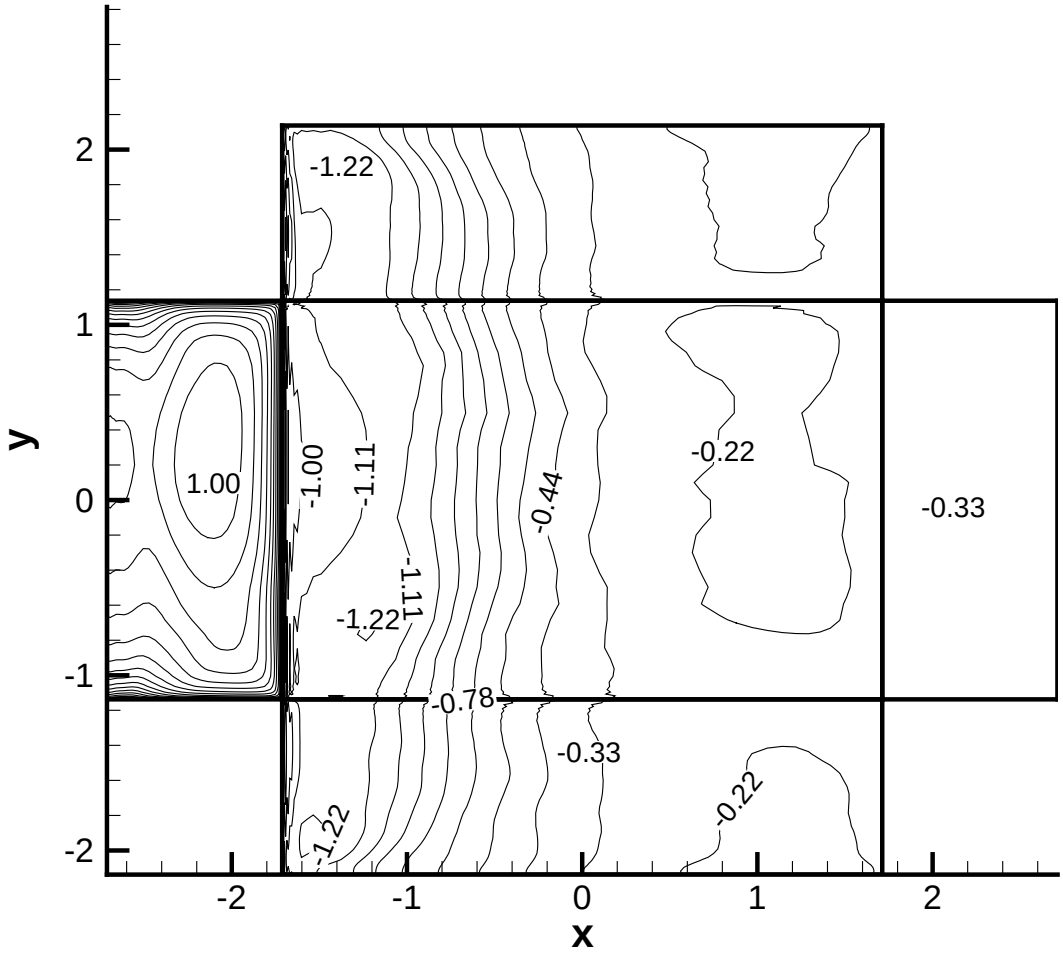

Figure 5.5: Contour plots of mean pressure coefficients on the surface of the prism under turbulent inflow conditions

The contour plot of the mean vorticity in the case of isotropic homogeneous inflow conditions, presented in figure 5.6 shows the separating shear layer over the prism. In comparison with figure 5.3, it is noted that the separating layer covers a smaller region. The secondary separation is also smaller. Again, one could associate the maximum observed mean pressure coefficient with the region between primary and secondary separations.

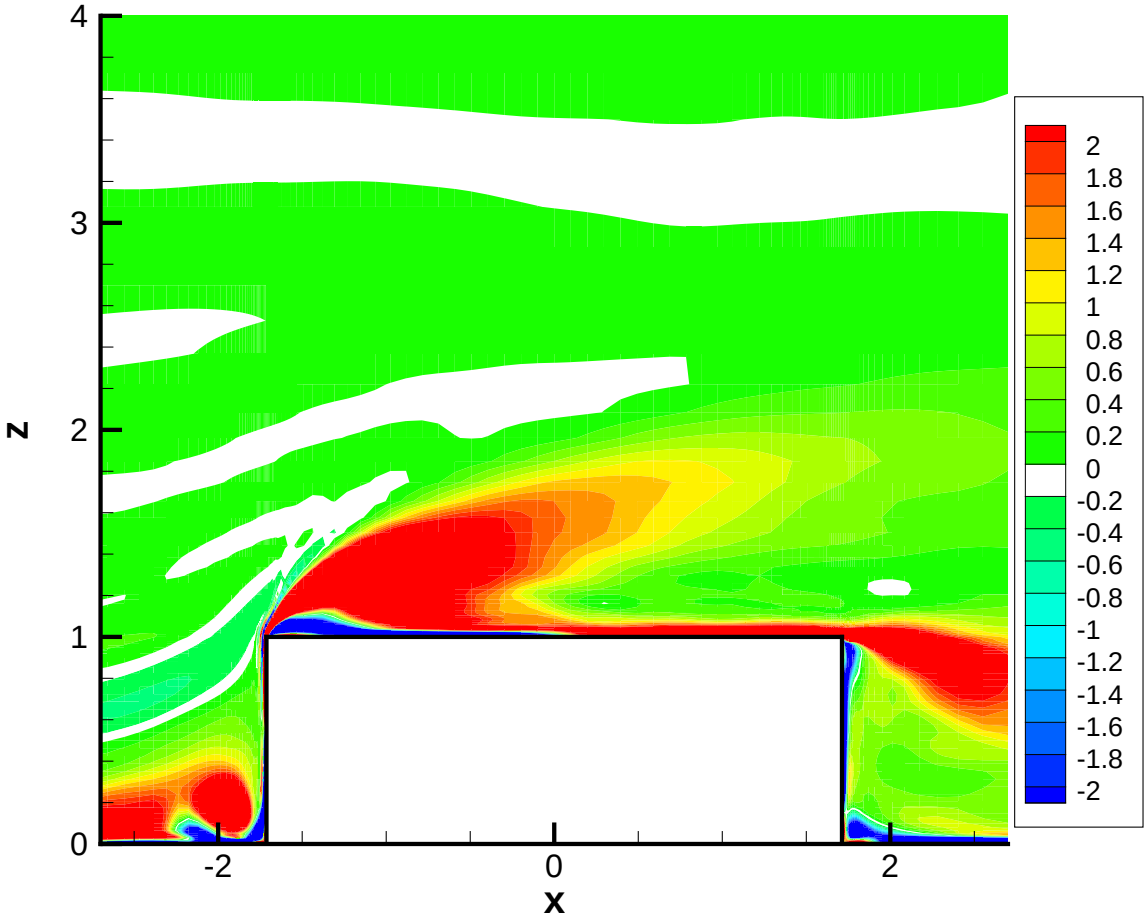

Figure 5.6: Contour plots of mean vorticity under turbulent inflow conditions

The plot of the mean coherent vortical structures in figure 5.7 shows the horseshoe vortex in front of the prism, the two separating shear layers at the leading edge of the prism and the coherent structures in the separation over the backside of the prism. A comparison of figures 5.4 and 5.7 shows that the mean coherent vortical structures in the case of homogeneous turbulence are concentrated over smaller regions.

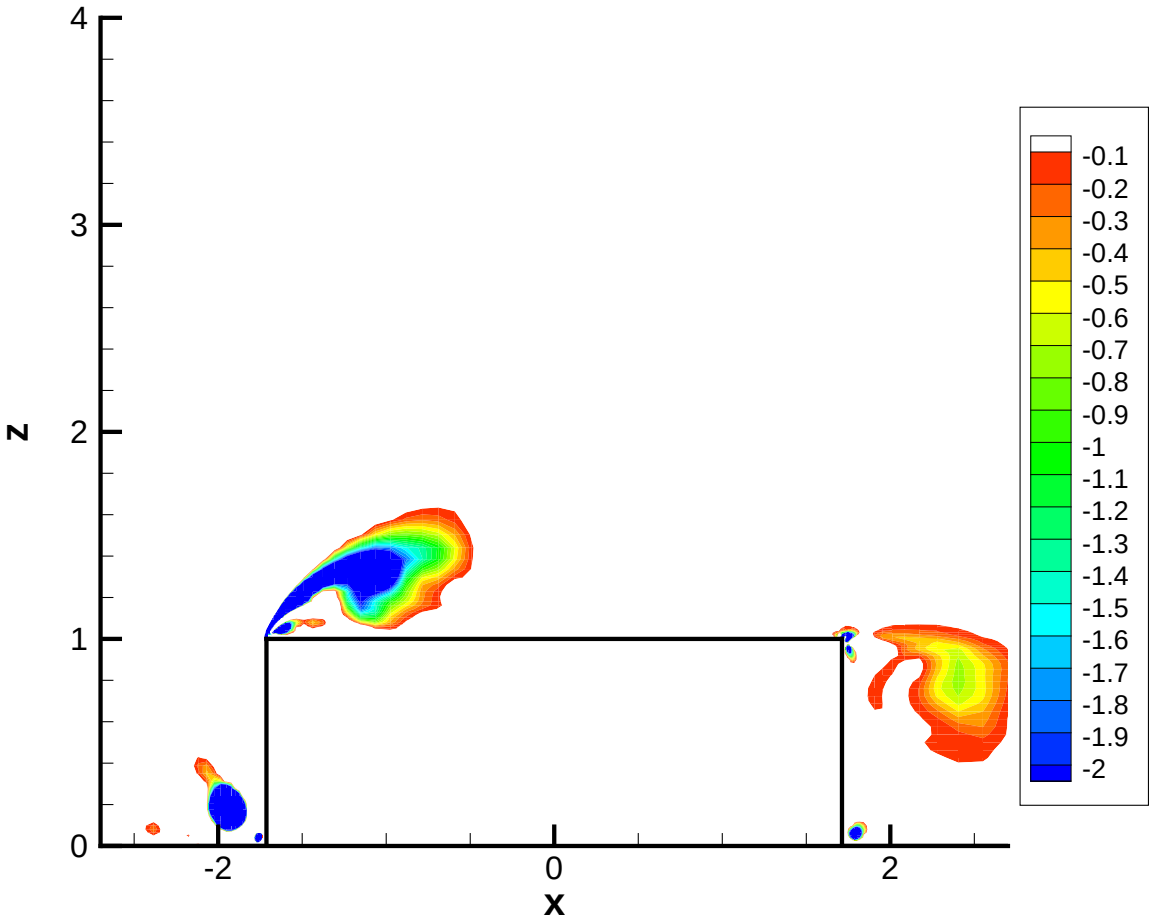

Figure 5.7: Contour plots of mean coherent vortical structures under turbulent inflow conditions

Contour plots of the root-mean-square (rms) pressure coefficients under smooth and turbulent inflow conditions are presented in figures 5.8 and 5.9 respectively. The results clearly show a higher level of variations on the roof and sides of the prism in the case of turbulent inflow in comparison with the case of smooth inflow. Figures 5.10 and 5.11 respectively present a comparison of the profiles of the simulated mean and rms pressure coefficients along the symmetry line on the roof with values measured in configuration 1a of the wind tunnel

experiments reported in Tieleman et al. [14]. The choice of this configuration is based on the fact that the turbulence intensities at the prism's location in the experimental setup of the longitudinal, lateral and vertical velocity components were 6.67%, 4.9% and 4.3% which are close to the near 5% value of the numerical simulations in the case of isotropic homogeneous turbulent inflow. The results clearly show that the predicted mean characteristics of the pressure coefficients in the turbulent case match the experimental values in terms of both magnitude and location on the roof of the prism.

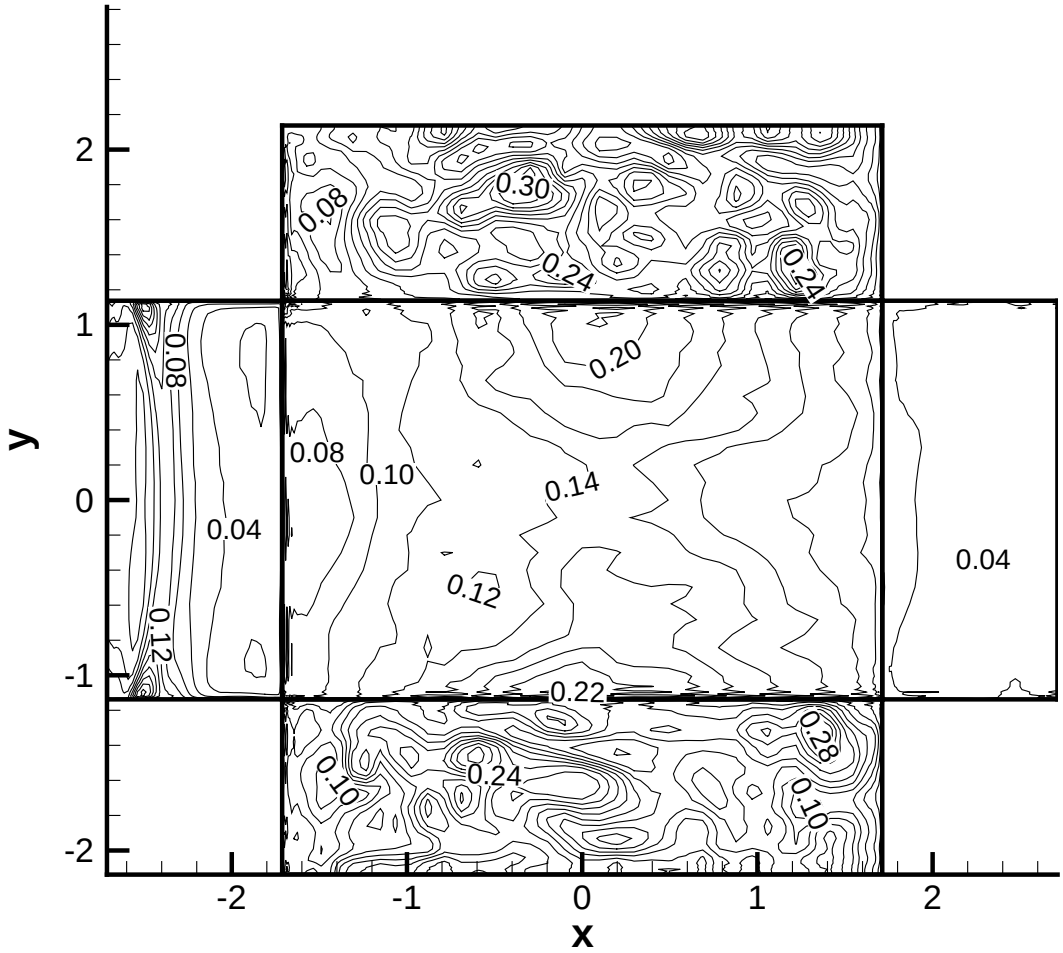

Figure 5.8: Contour plots of rms pressure coefficients on the surface of the prism under smooth inflow conditions

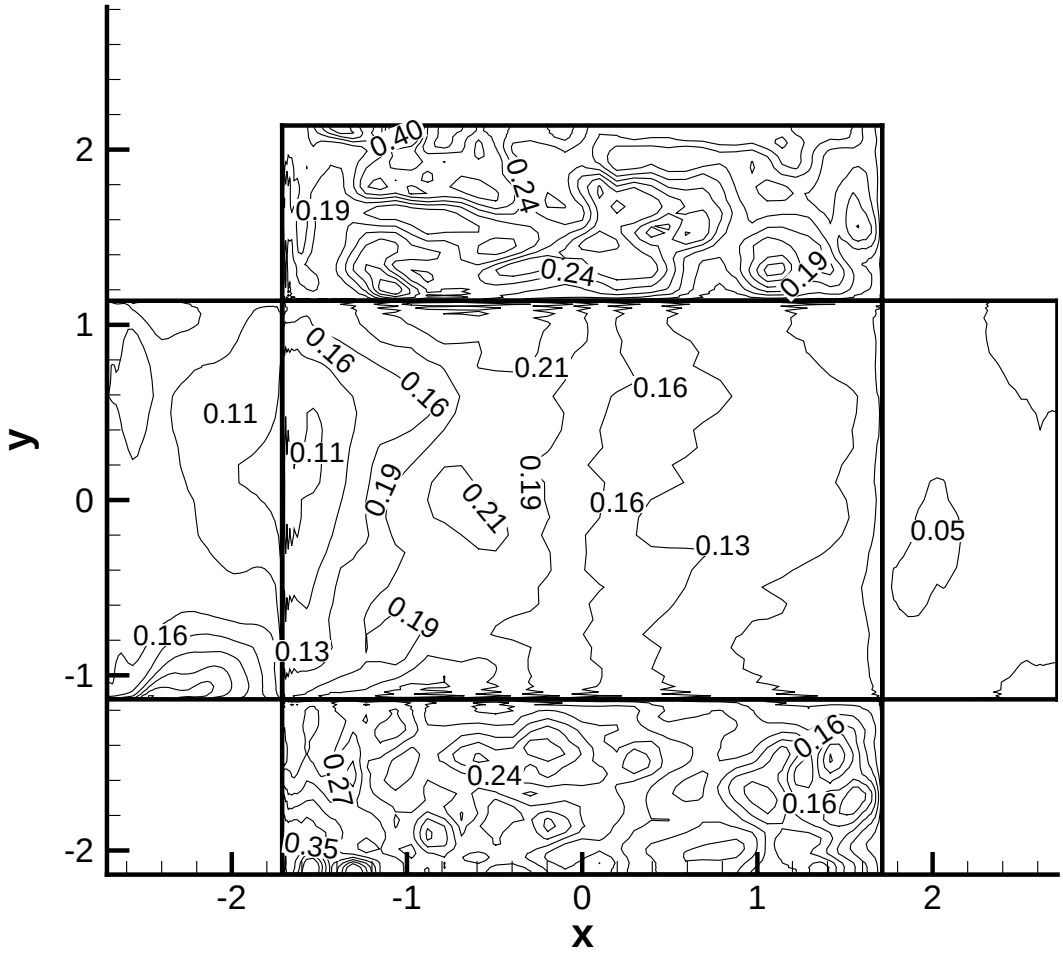

Figure 5.9: Contour plots of rms pressure coefficients on the surface of the prism under turbulent inflow conditions

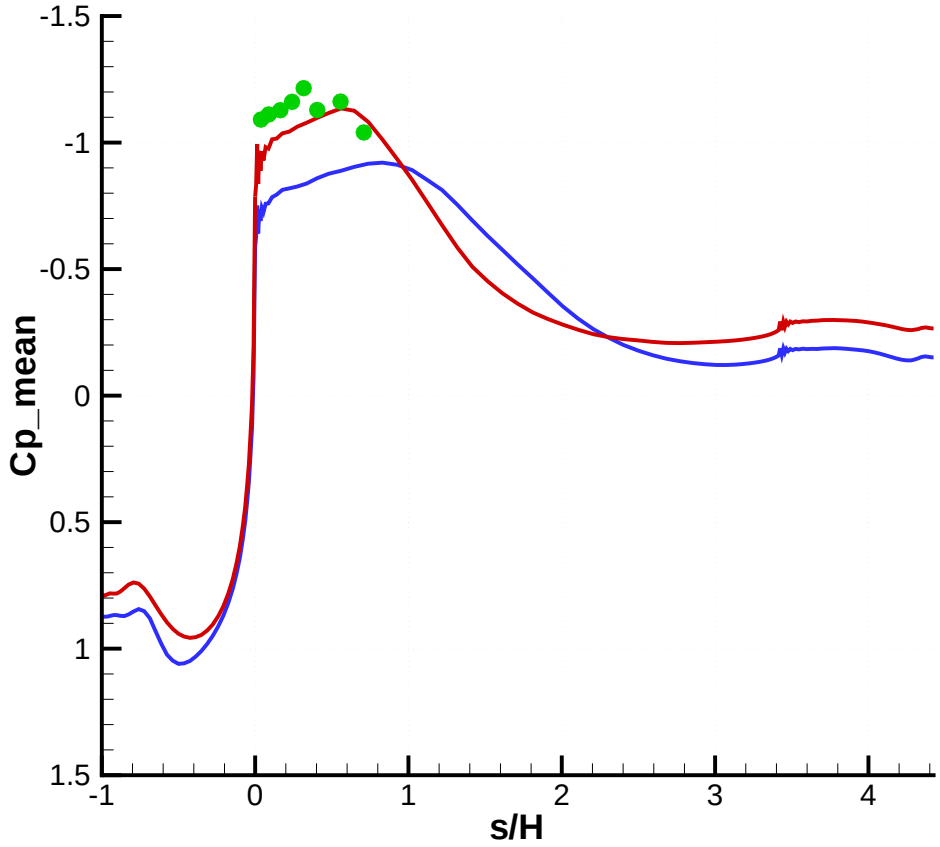

Figure 5.10: Comparison of the mean pressure coefficient as predicted in the smooth and turbulent inflow conditions with experimental values measured in configuration 1 by Tieleman et al. (1998)

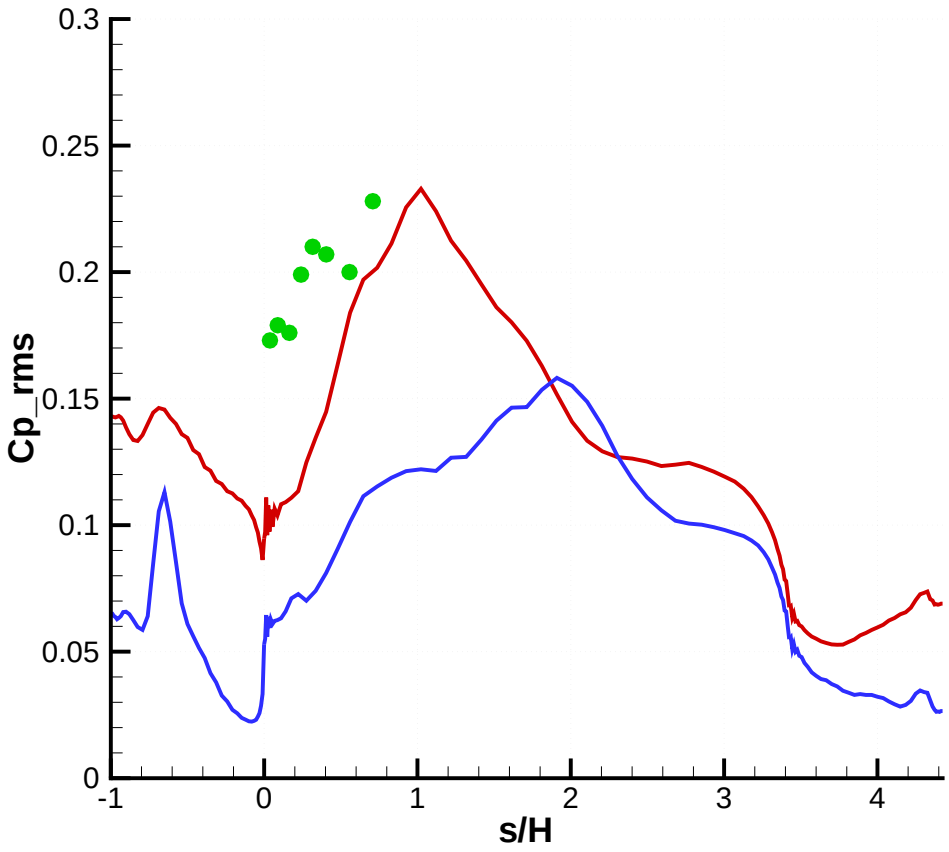

Figure 5.11: Comparison of the rms pressure coefficient as predicted in the smooth and turbulent inflow conditions with experimental values measured in configuration 1 by Tieleman et al. (1998)

5.3 Peak surface pressure

Figures 5.12 and 5.13 show time series of the surface pressure coefficients as determined in the numerical simulations of the smooth and turbulent inflow conditions. The time series are determined at the points on the roof where peak values were observed in both cases. These points are both near tap # 8 in the experiments reported by Tieleman et al. [14]. The

results clearly show that the measured peak value in the turbulent inflow case is about 30% larger than the one observed in the case of smooth inflow. The peak value of -2 obtained in the turbulent inflow case is about 20% smaller than the values measured experimentally by Tieleman et al. [14] at tap # 8 in configuration 1. Yet, it is important to note that the peak value reported by Tieleman et al. [14] were obtained from a record with a nondimensional duration $UT/H = 1091$. By comparison, the peak value reported for the case of turbulent inflow is obtained from a record with a duration $UT/H = 25$. Consequently, one would expect that the peak value would increase as this duration is increased.

A contour plot of the instantaneous pressure coefficient near the time when peak values were observed on the roof is presented in figure 5.14 for the case of smooth inflow boundary condition. The corresponding vorticity and coherent vortical structures over the midplane are presented in figures 5.15 and 5.16, respectively. The contour plot in figure 5.14 shows a peak with a value of -1.4 near $x = -0.6$ and at the midplane ($y = 0$) section of the prism. By examining figures 5.15 and 5.16 one could associate this peak with a vortex that forms in the flow and that gets closer to the roof of the prism.

Figures 5.17-5.21 show contour plots of the instantaneous pressure coefficients at five instants of time in the case of turbulent inflow conditions. These instants correspond to an instant when a peak was observed ($t = 147.146$), two times before and two others after. For these same instants, contour plots of the instantaneous vorticity and coherent vortical structures are presented in figures 5.22-5.31. The vorticity plots clearly show a relation between the separating shear layer, its roll-up and rotation towards the roof and the observed pressure peak in figure 5.19. The instantaneous coherent vortical structures plots in figures 5.27-5.31 show that the pressure peak is associated with a coherent structure that forms and moves closer to the roof.

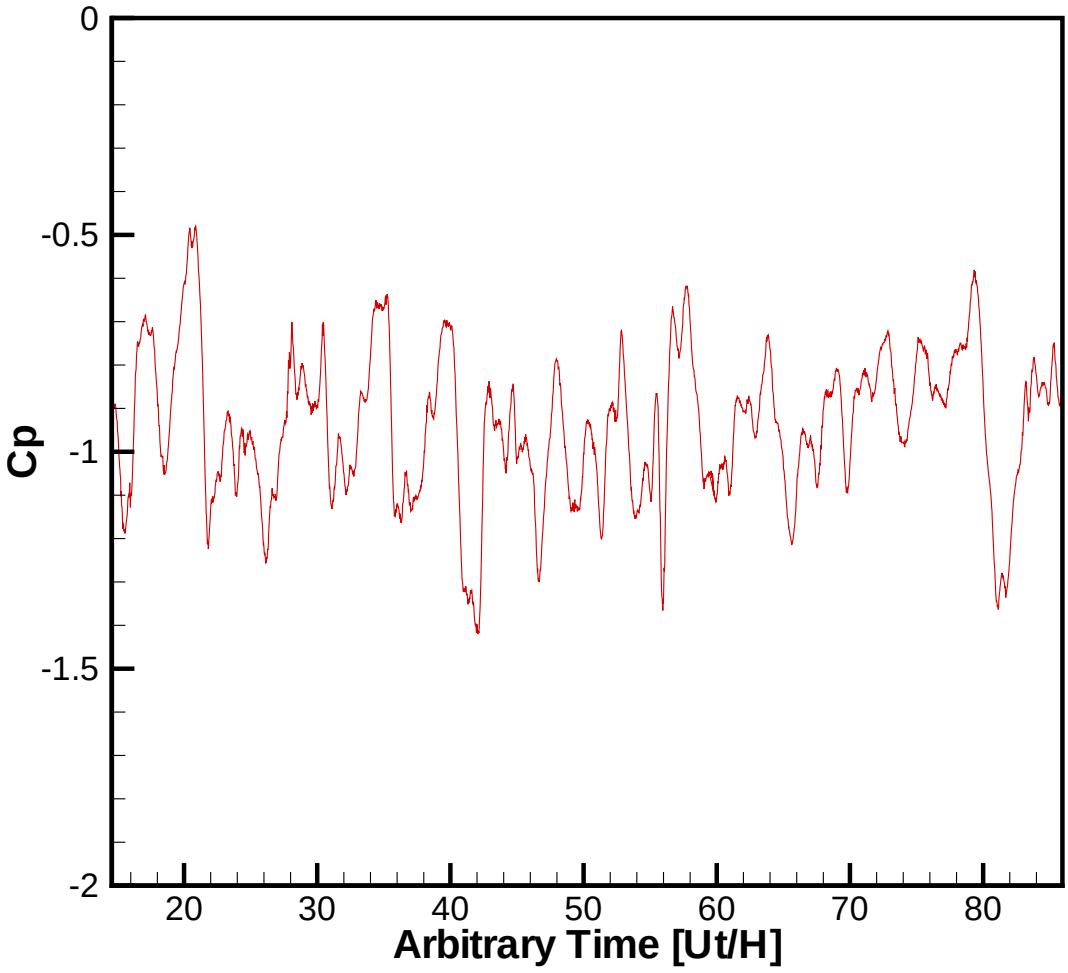

Figure 5.12: Time series of the surface pressure coefficients on the roof at the point where peak value was observed in the case of smooth inflow

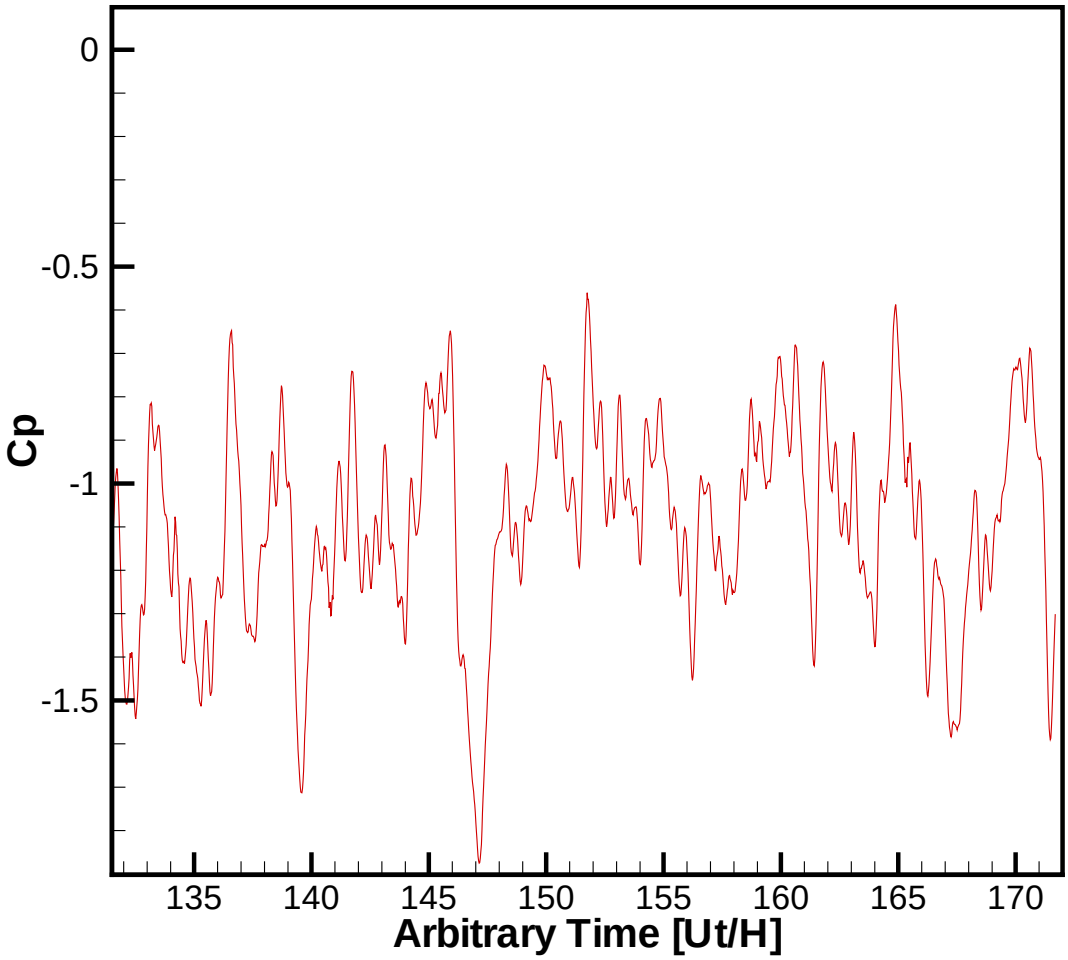

Figure 5.13: Time series of the surface pressure coefficients on the roof at the point where peak value was observed in the case of turbulent inflow

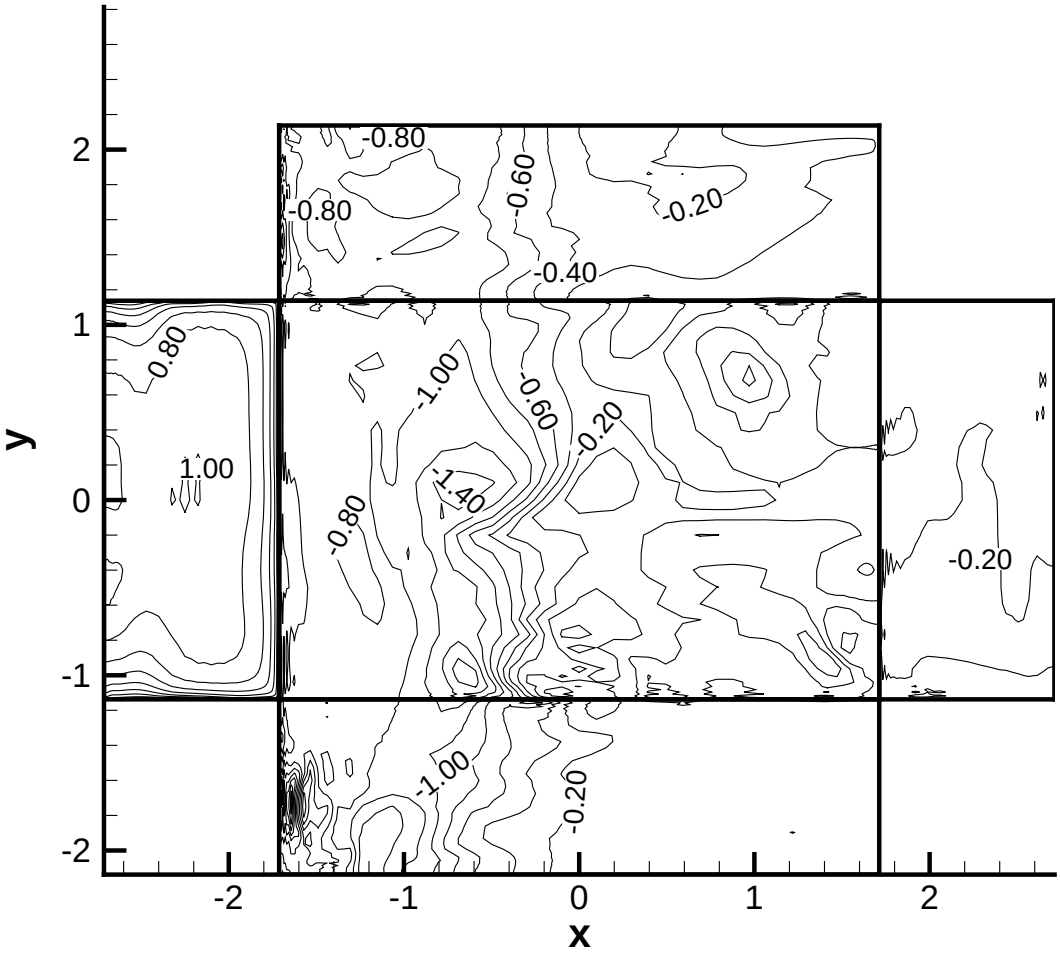

Figure 5.14: Contour plots of the instantaneous pressure coefficients near the time when peak values were observed on the surface of the prism under smooth inflow conditions at the relative time t=41

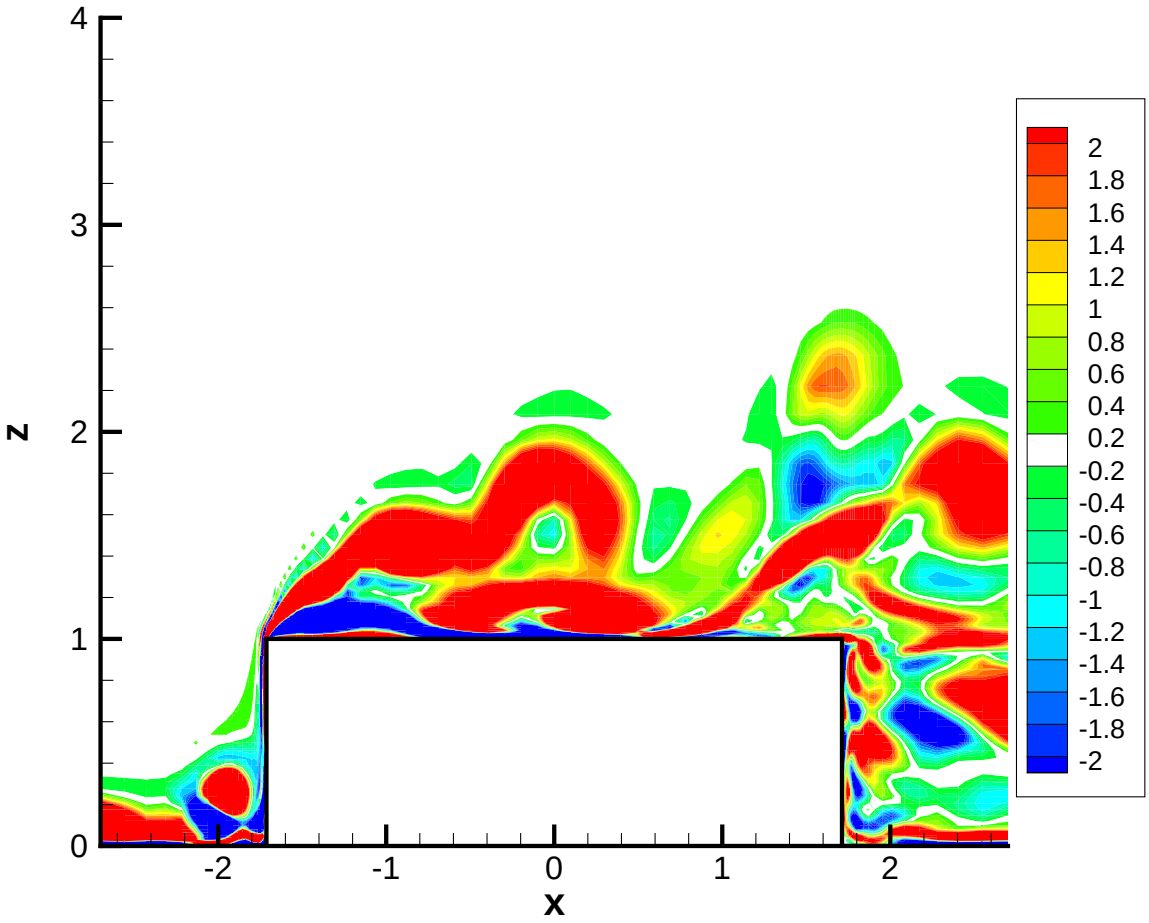

Figure 5.15: Contour plots of instantaneous vorticity near the time when peak values of pressure coefficients were observed on the surface of the prism under smooth inflow conditions at the relative time t=41

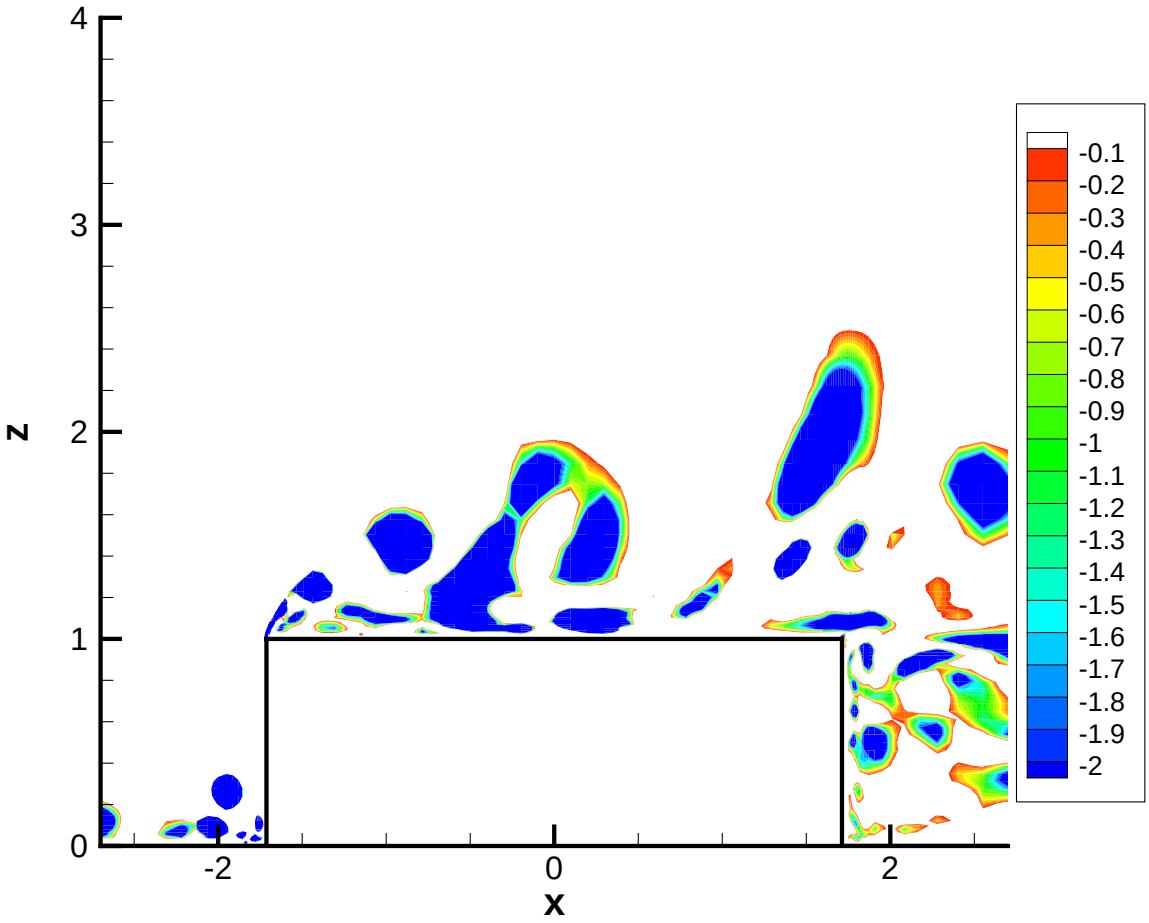

Figure 5.16: Contour plots of instantaneous coherent vortical structures near the time when peak values of pressure coefficients were observed on the surface of the prism under smooth inflow conditions at the relative time t=41

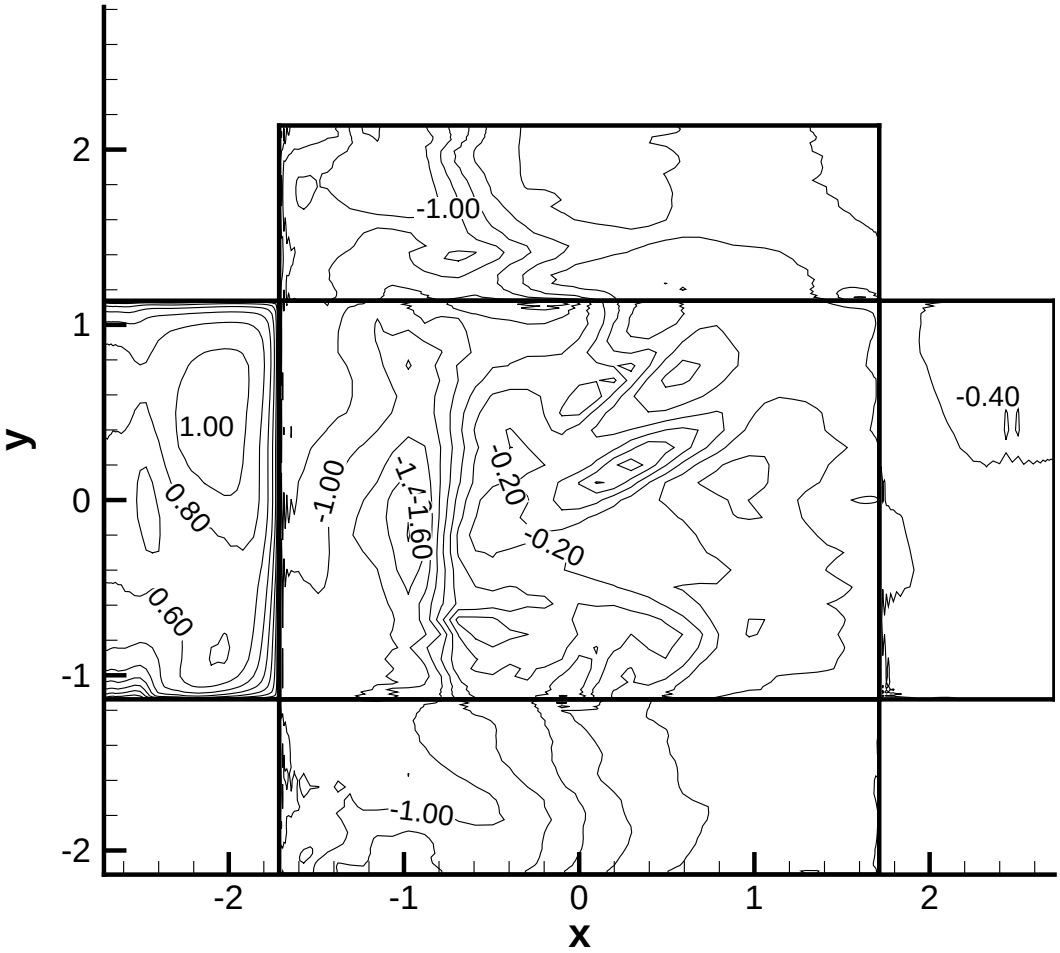

Figure 5.17: Contour plots of the instantaneous pressure coefficients on the surface of the prism under turbulent inflow conditions at the relative time t=146.674

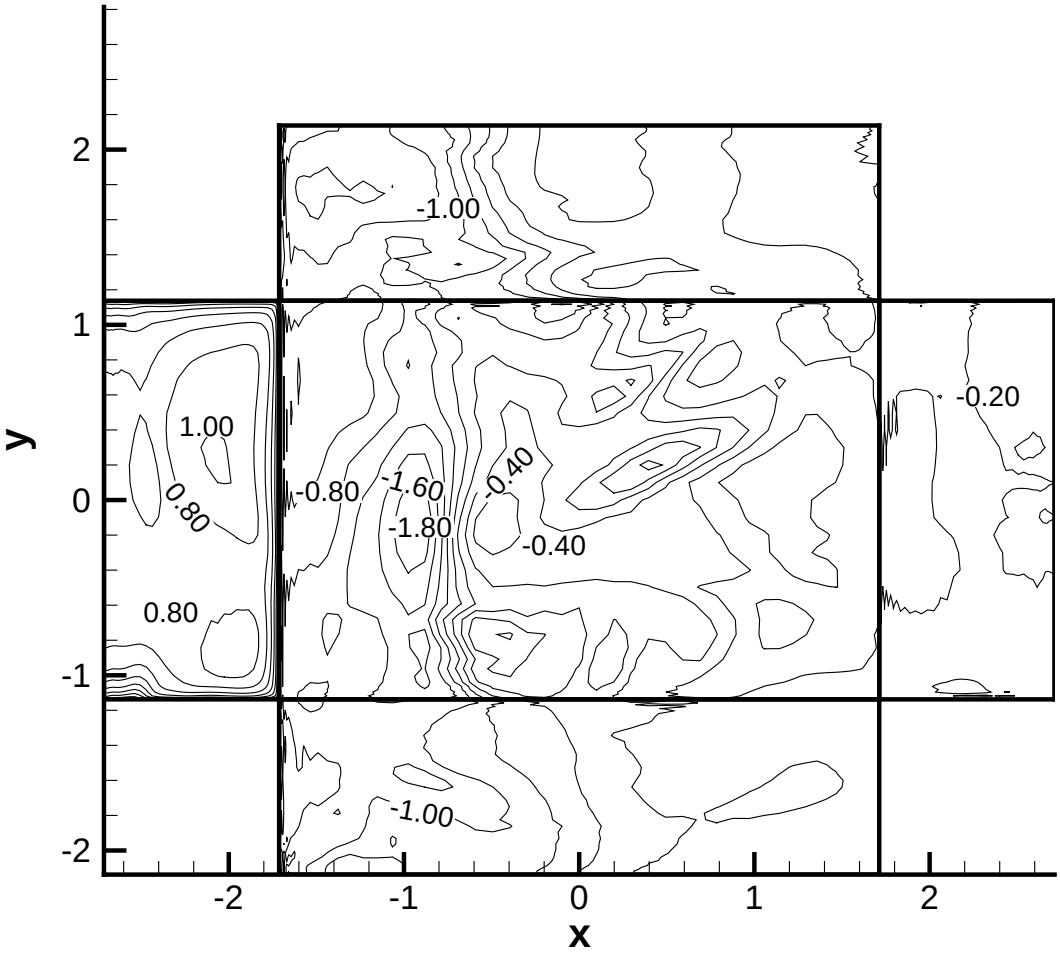

Figure 5.18: Contour plots of the instantaneous pressure coefficients on the surface of the prism under turbulent inflow conditions at the relative time t=146.91

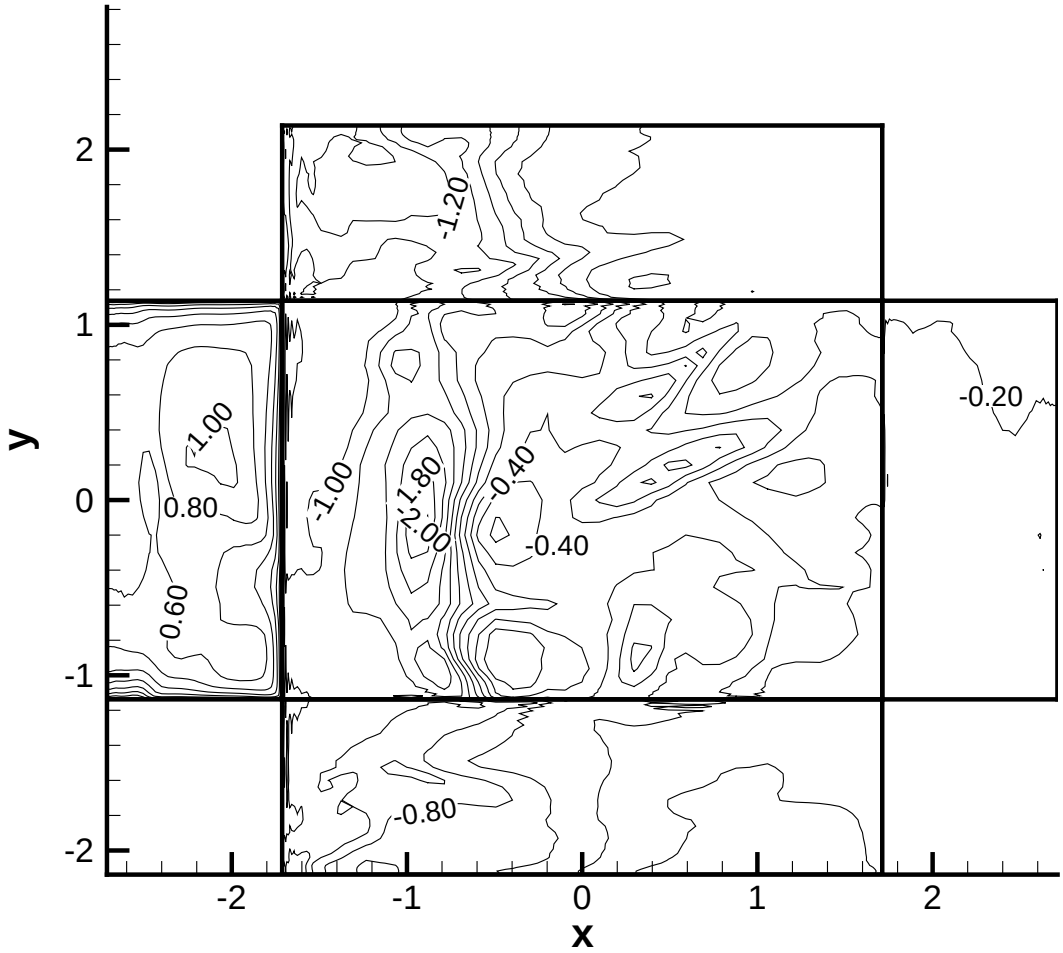

Figure 5.19: Contour plots of the instantaneous pressure coefficients near the time when peak values were observed on the surface of the prism under turbulent inflow conditions at the relative time t=147.146

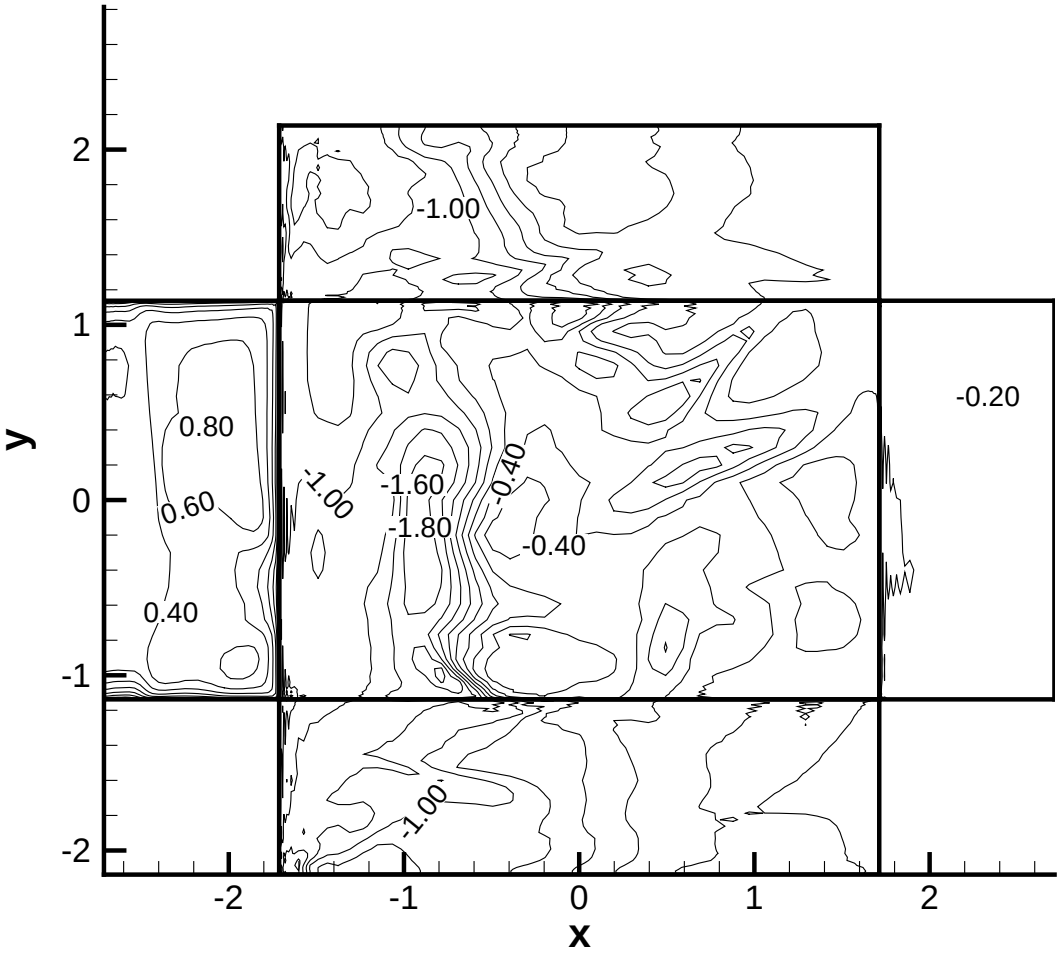

Figure 5.20: Contour plots of the instantaneous pressure coefficients on the surface of the prism under turbulent inflow conditions at the relative time t=147.382

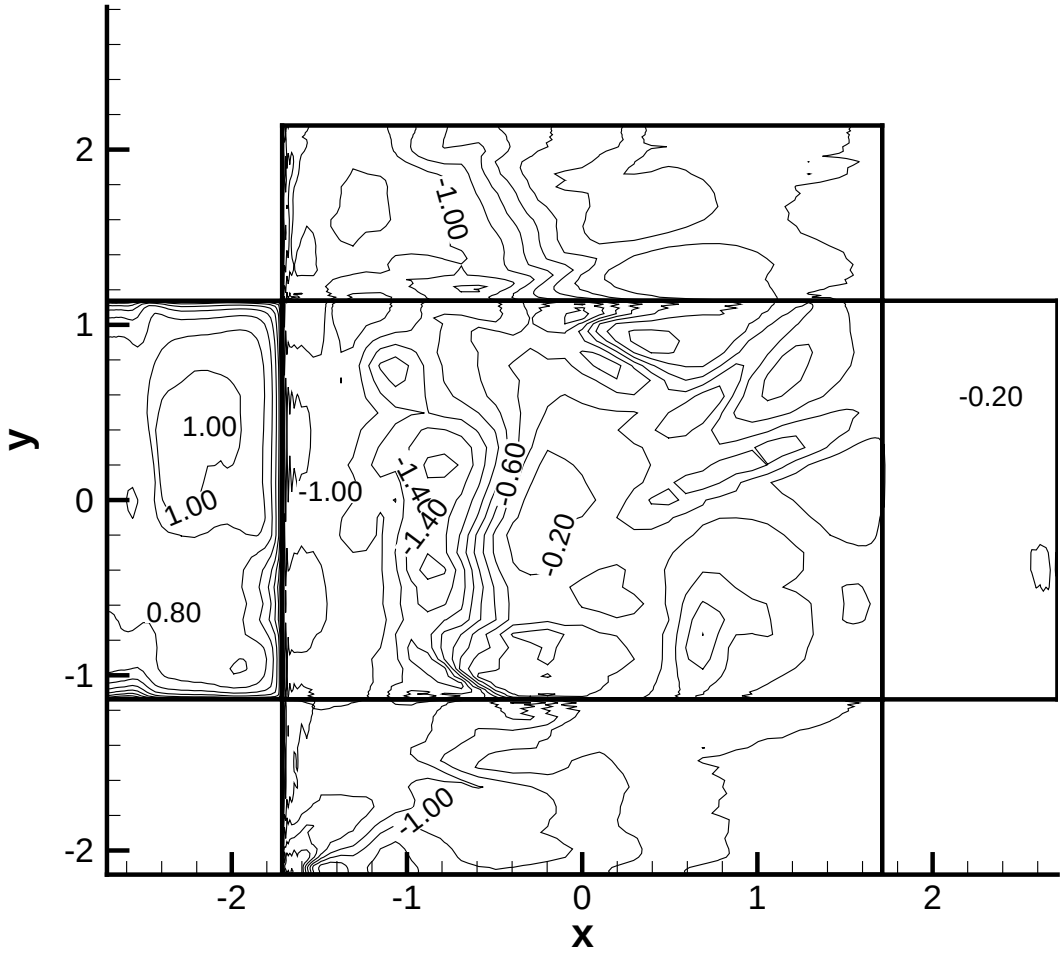

Figure 5.21: Contour plots of the instantaneous pressure coefficients on the surface of the prism under turbulent inflow conditions at the relative time t=147.618

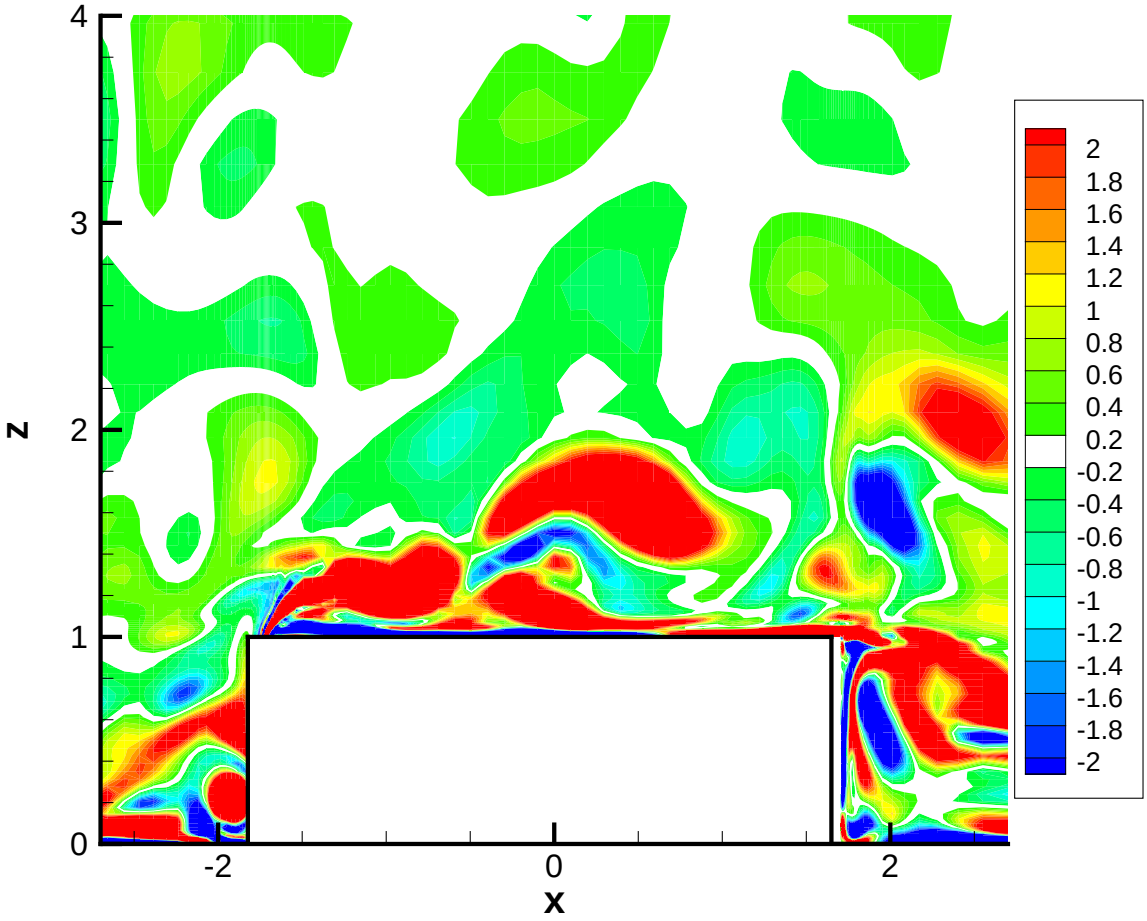

Figure 5.22: Contour plots of instantaneous vorticity under turbulent inflow conditions at the relative time t=146.674

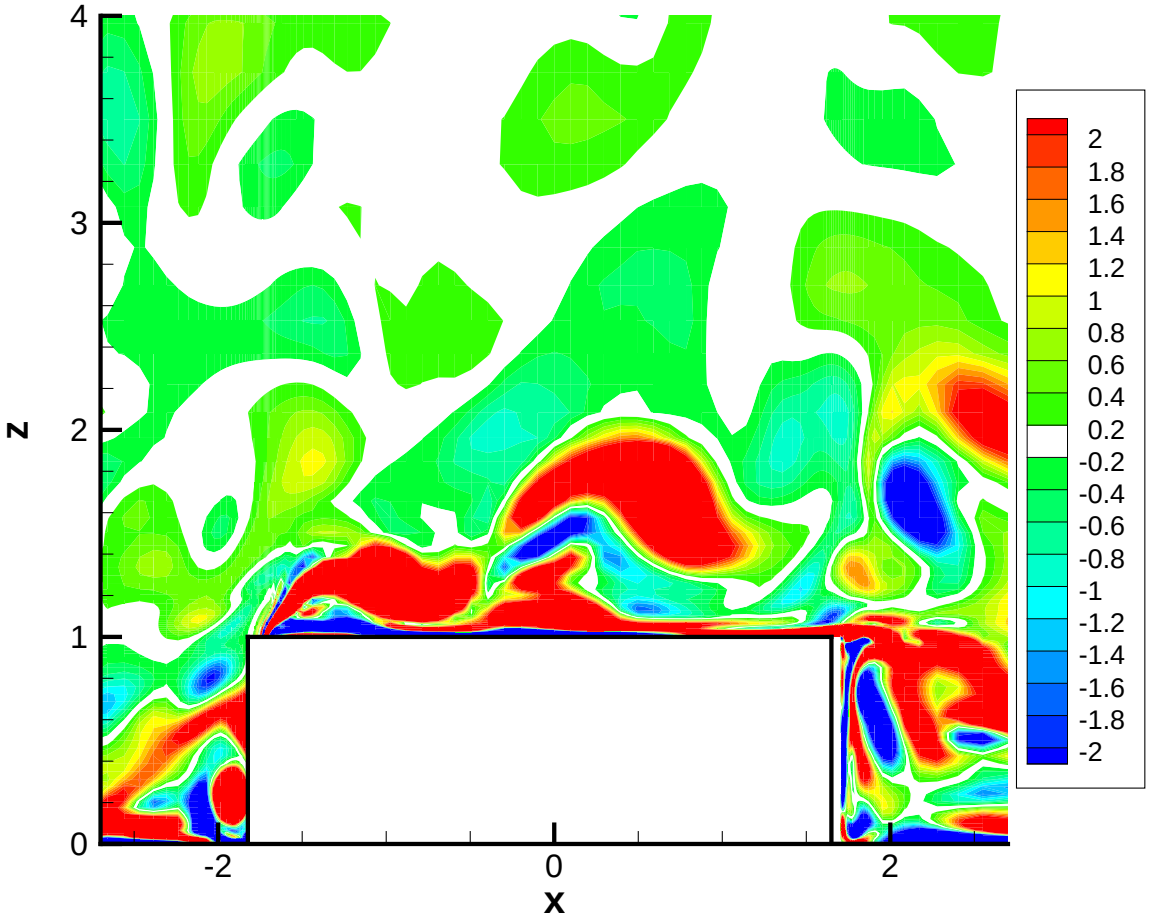

Figure 5.23: Contour plots of instantaneous vorticity under turbulent inflow conditions at the relative time t=146.91

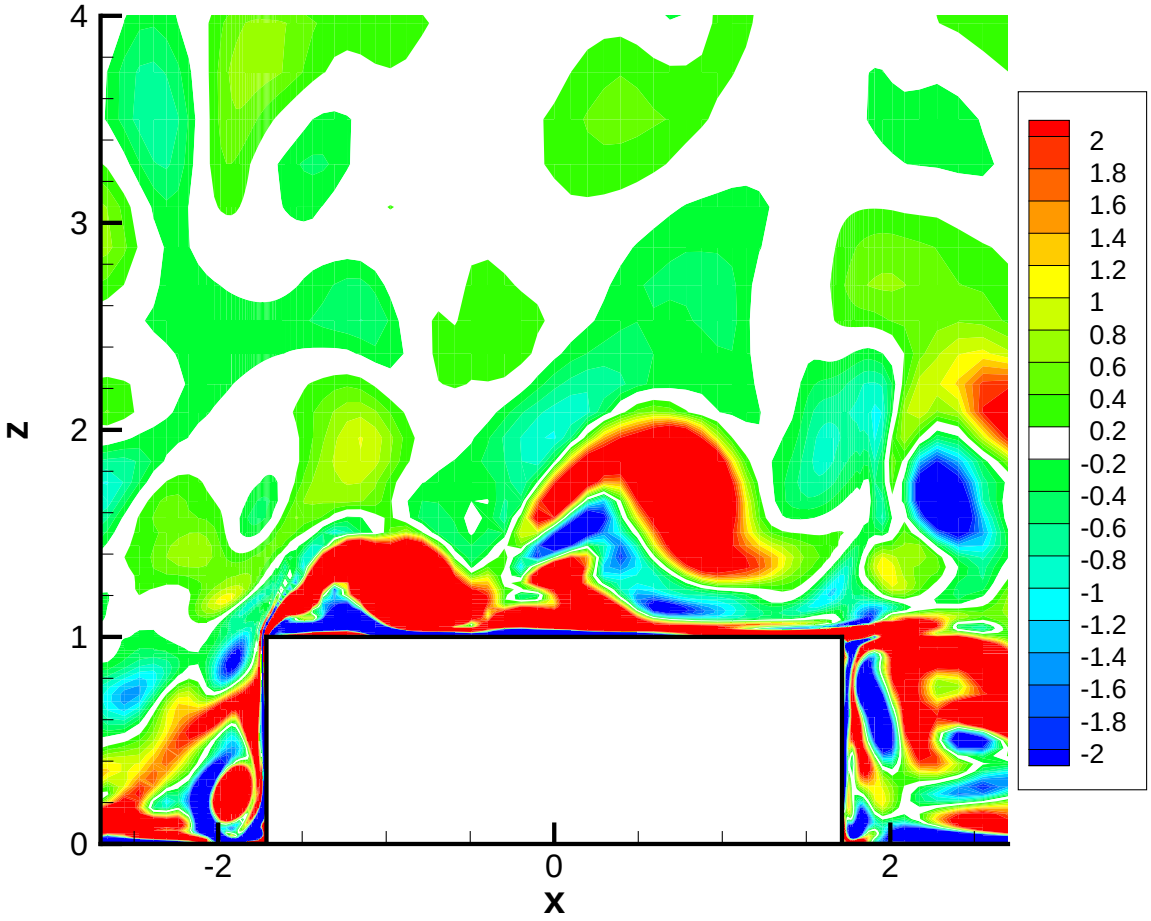

Figure 5.24: Contour plots of instantaneous vorticity near the time when peak values of pressure coefficients were observed on the surface of the prism under turbulent inflow conditions at the relative time t=147.146

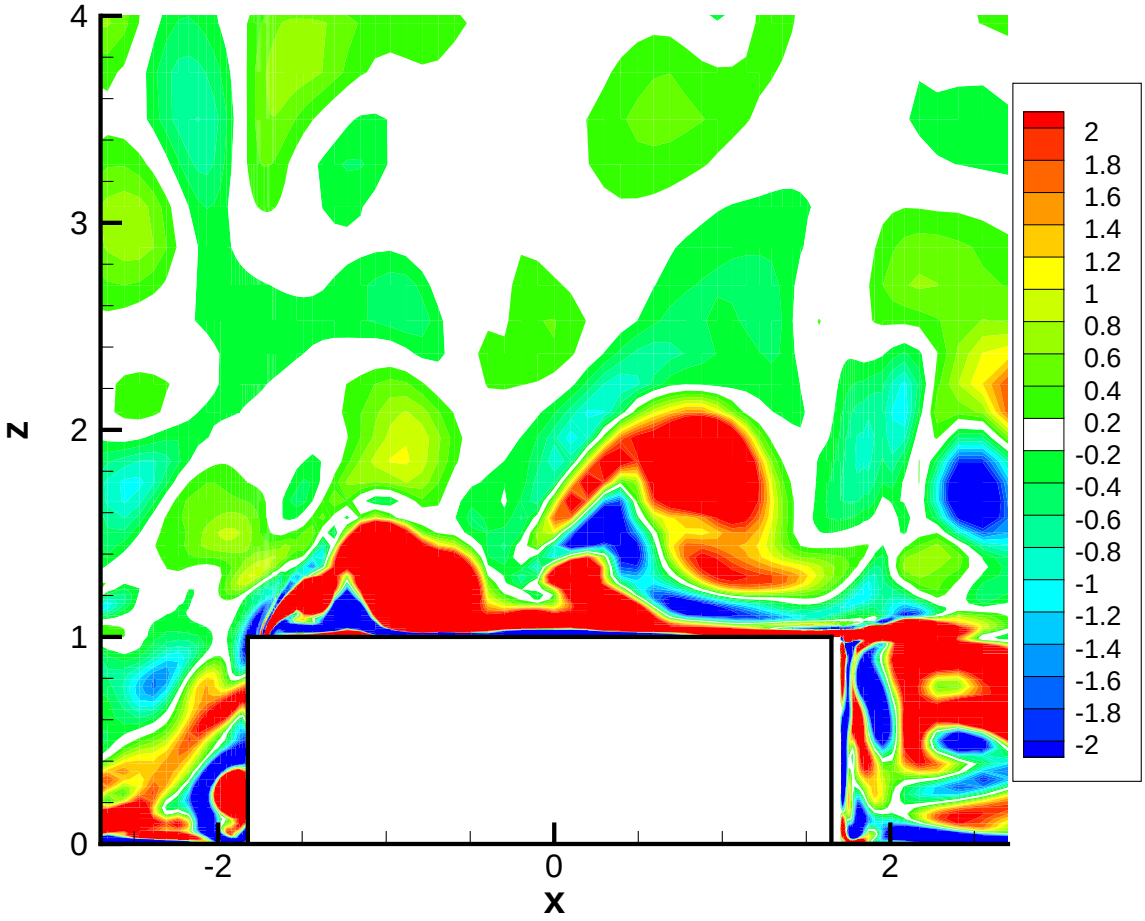

Figure 5.25: Contour plots of instantaneous vorticity under turbulent inflow conditions at the relative time t=147.382

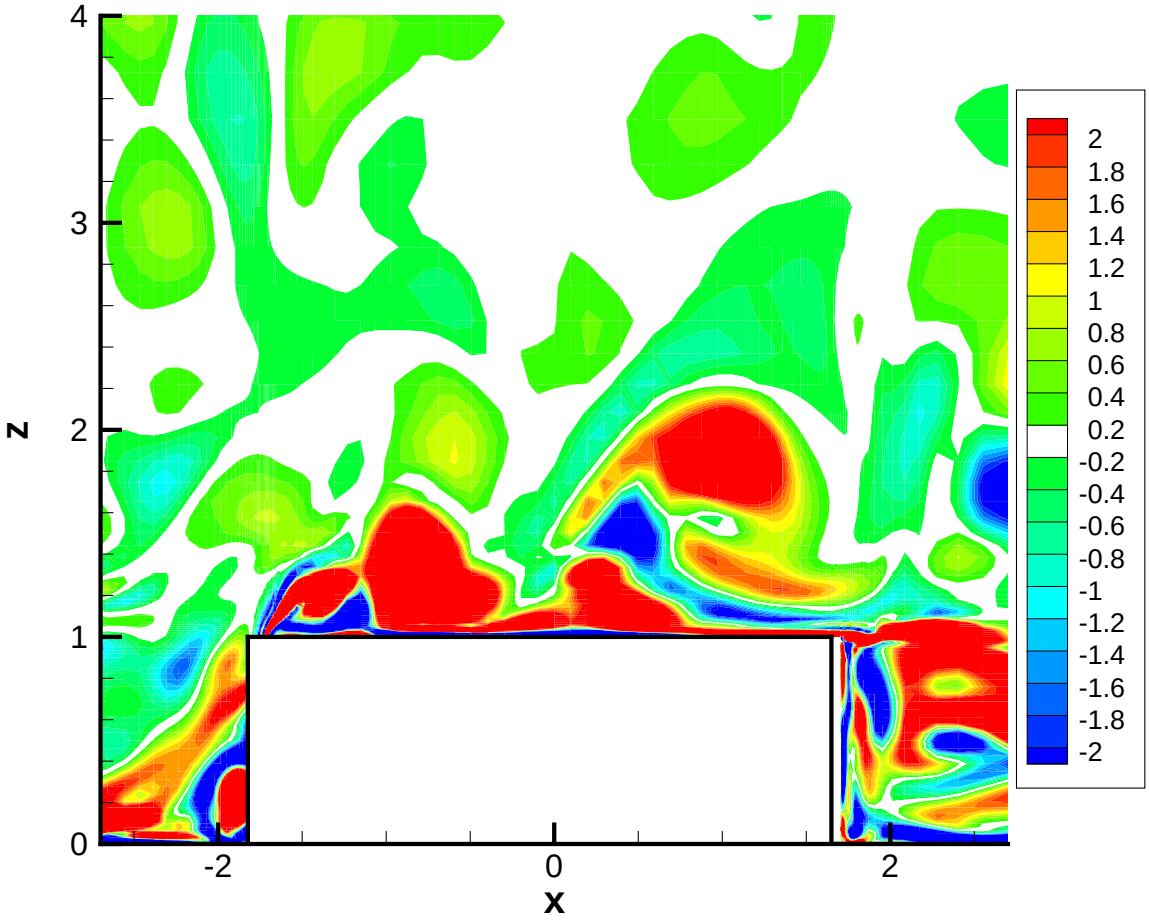

Figure 5.26: Contour plots of instantaneous vorticity under turbulent inflow conditions at the relative time t=147.618

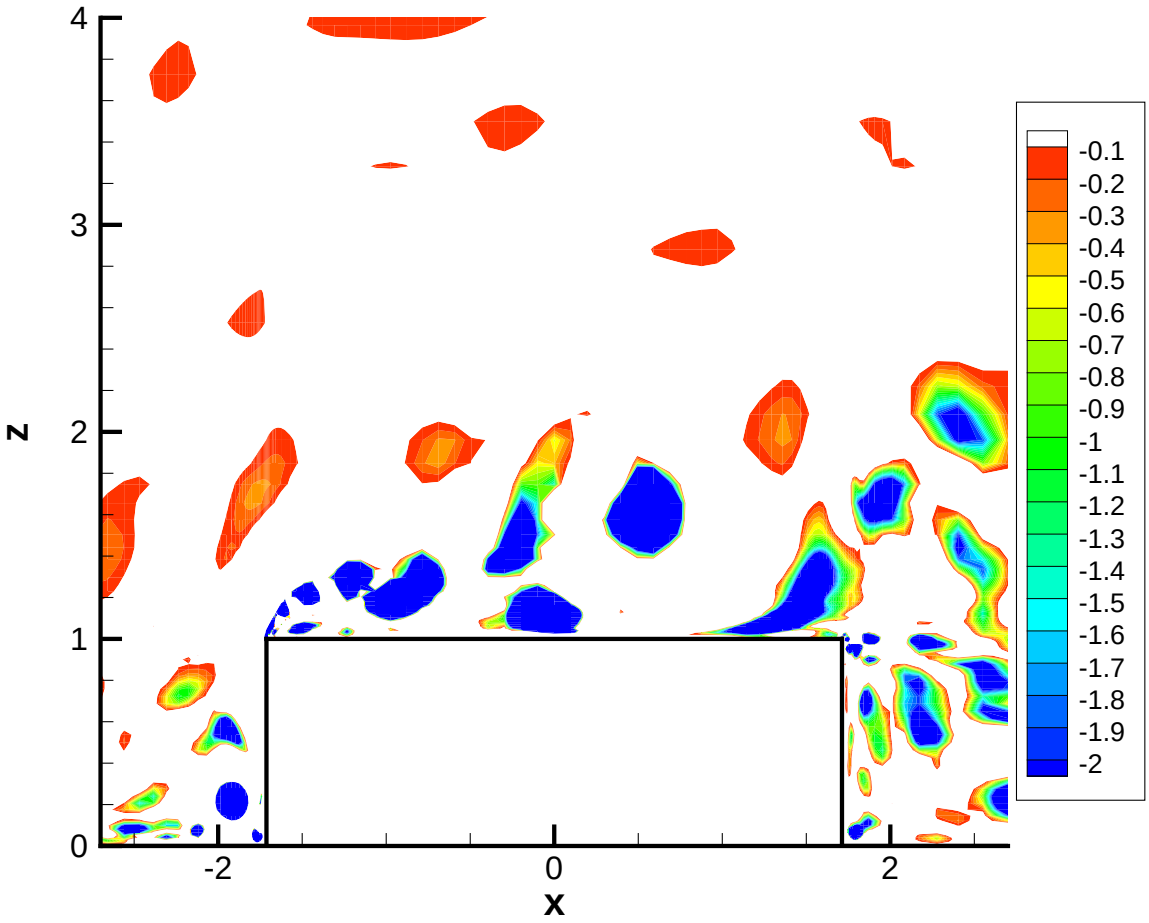

Figure 5.27: Contour plots of instantaneous coherent vortical structures near the time when peak values of pressure coefficients were observed on the surface of the prism under turbulent inflow conditions at the relative time t=146.674

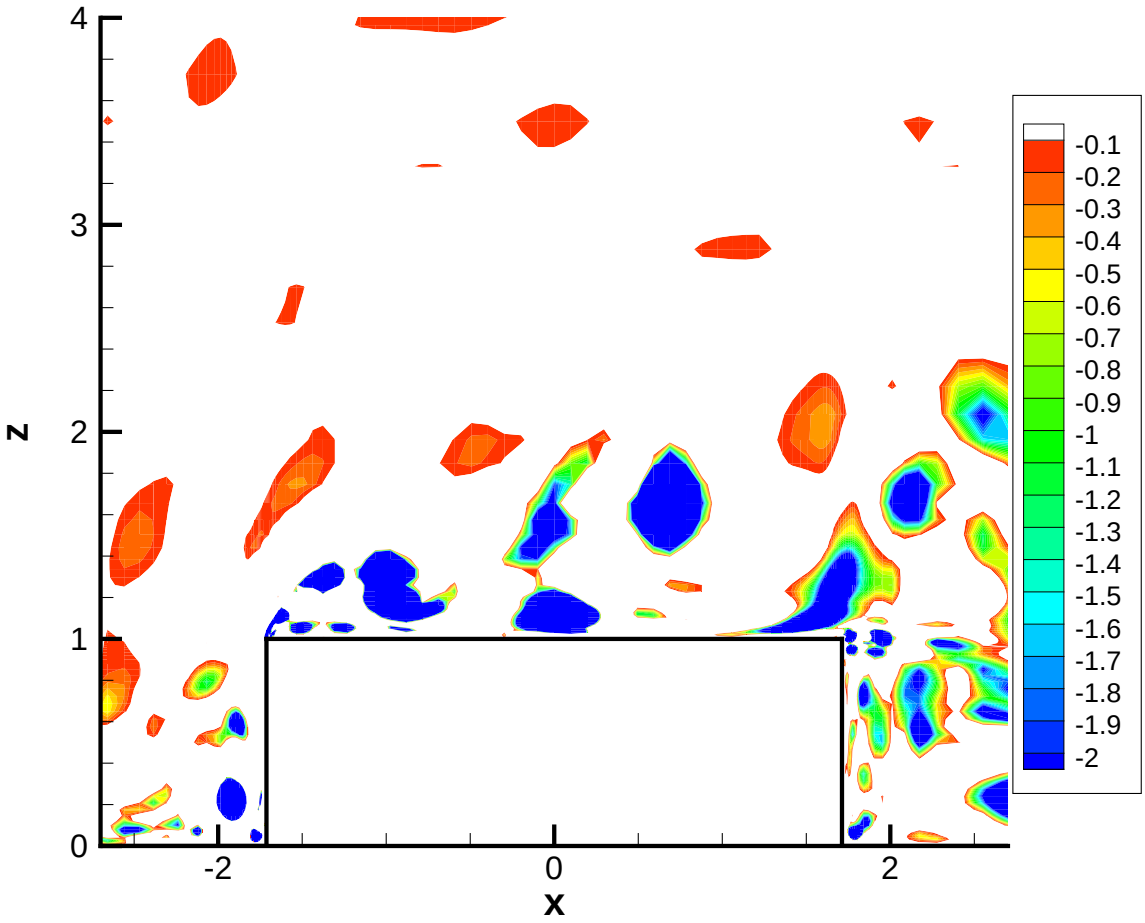

Figure 5.28: Contour plots of instantaneous coherent vortical structures near the time when peak values of pressure coefficients were observed on the surface of the prism under turbulent inflow conditions at the relative time t=146.91

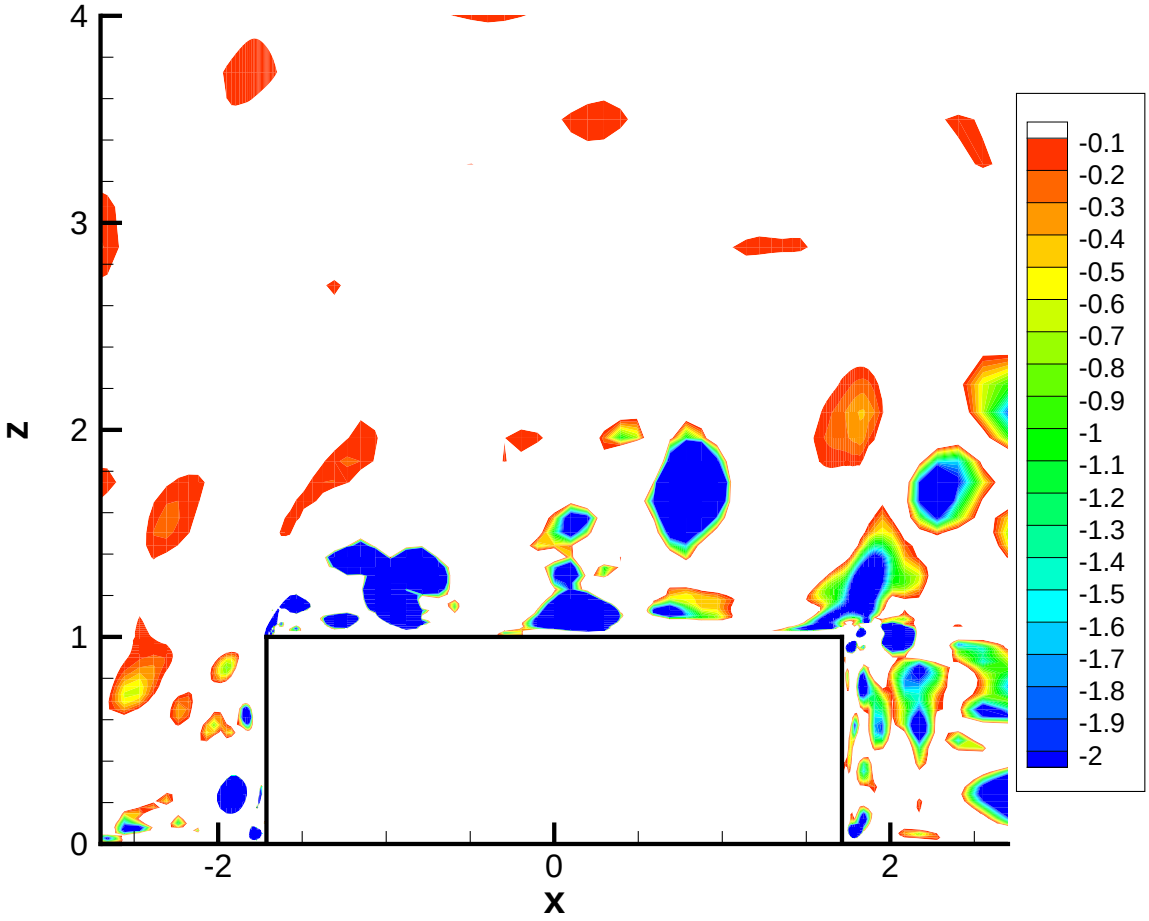

Figure 5.29: Contour plots of instantaneous coherent vortical structures near the time when peak values of pressure coefficients were observed on the surface of the prism under turbulent inflow conditions at the relative time t=147.146

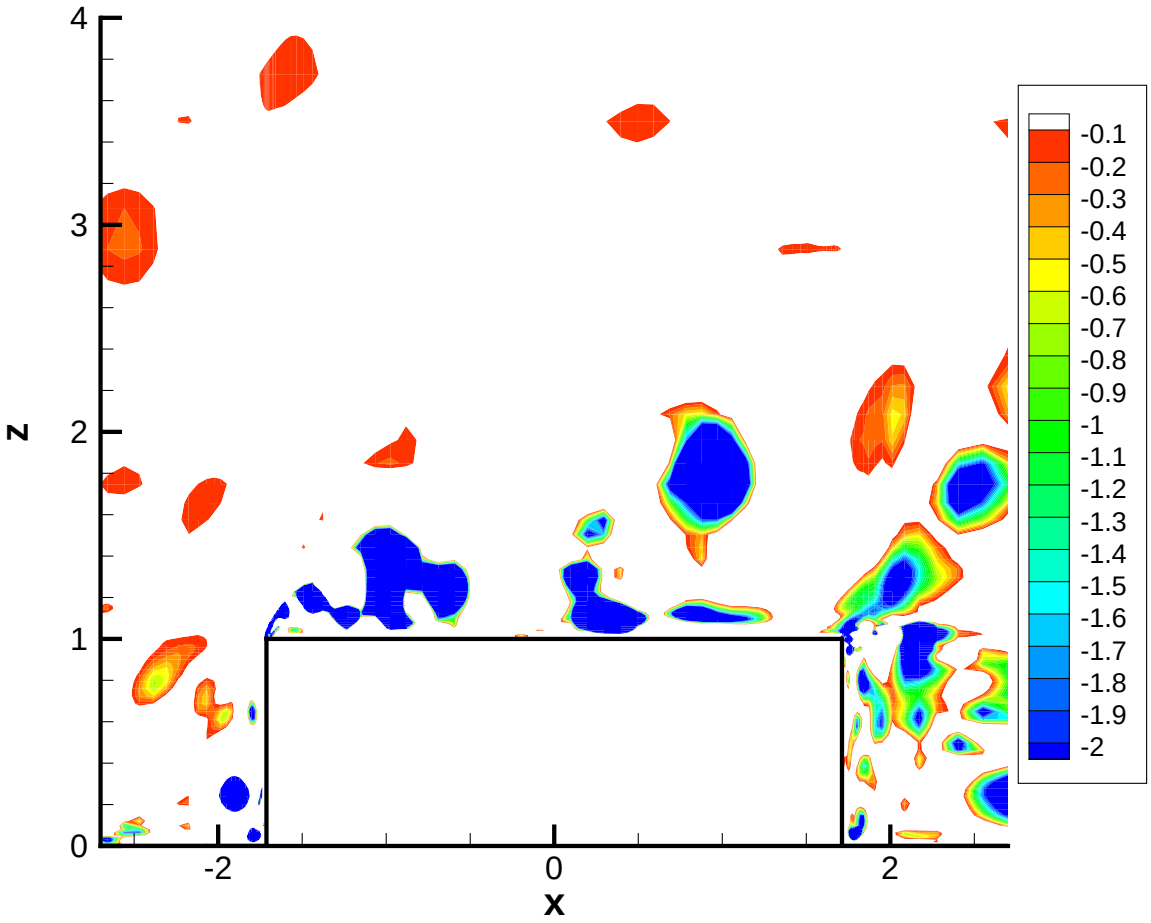

Figure 5.30: Contour plots of instantaneous coherent vortical structures near the time when peak values of pressure coefficients were observed on the surface of the prism under turbulent inflow conditions at the relative time t=147.382

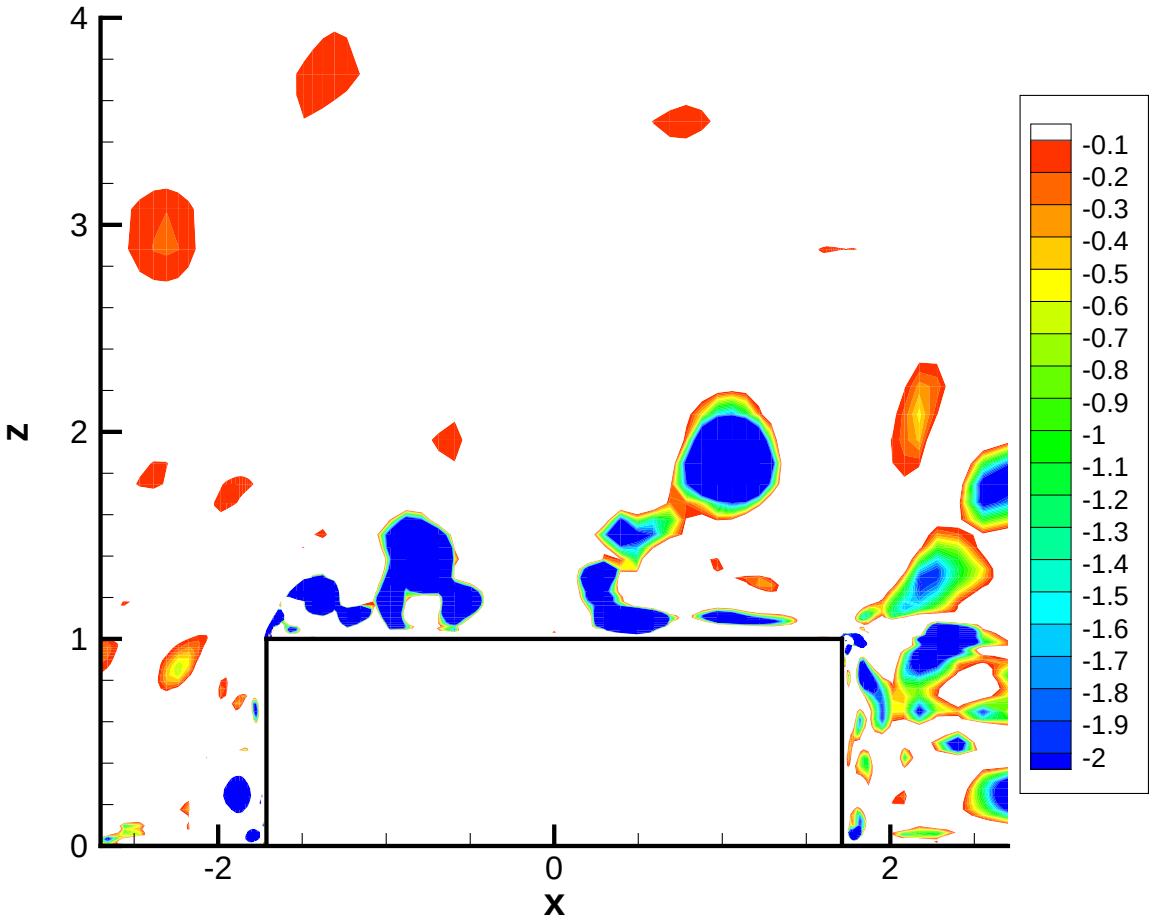

Figure 5.31: Contour plots of instantaneous coherent vortical structures near the time when peak values of pressure coefficients were observed on the surface of the prism under turbulent inflow conditions at the relative time t=147.618

5.4 Probability of non exceedence

The dependence of the peak surface pressure coefficient on the record duration as explained above, makes a direct comparison of peak values ineffective. To overcome this problem,

Tieleman et al. [11] and Tieleman et al. [38] proposed using a procedure developed by Sadek and Simiu [40] to obtain the distribution of peak pressure pressure coefficient from a single sample record. When only a single pressure or load record is available, a theoretical procedure is used for the evaluation of the peak distribution of the non-Gaussian time histories. This procedure, based on the work by Grigoriu [41], and presented in a paper by Gioffre et al. [42], was adapted by Sadek and Simiu [40] for a data-base-assisted design to estimate peaks of internal forces induced by wind in low-rise building frames.

The initial step for this procedure is to identify the appropriate marginal probability density function (PDF) of the parent time histories. The previous results by Tieleman et al. [11] have revealed that the gamma and the normal distributions are the most likely candidates for the representation of time histories of the pressure and loads in regions where the flow is separated. Application of these distributions requires acceptable estimates of their defining parameters including the shape, location and scale parameters. For the normal (two-parameter) distribution the location parameter is simply the mean of the time series and the scale parameter is equivalent to its standard deviation, while the shape parameter is zero. On the other hand, histograms of the pressure and load coefficients obtained in the separation regions over the prism demonstrate their skewness towards the negative side, making them suitable to be represented by the 3-parameter gamma function for $x \gg \mu$:

$$f(x) = \frac{[\frac{(x-\mu)}{\beta}]^{\gamma-1} exp(-\frac{x-\mu}{\beta})}{\beta\Gamma(\gamma)} \tag{5.1}$$

where β, γ, and μ are the scale, shape and location parameters respectively and $\Gamma(.)$ is the gamma function. The condition that $x \gg \mu$ requires that, for negative suction pressures, the time records be multiplied by -1. Estimates of the parameters describing the gamma distribution can be obtained with several methods such as the probability plot with the associated probability plot correlation coefficient (PPCC) and the method of moments. The routine estimation of the three parameters with the latter method involves the evaluation of the skewness, S, the standard deviation, $x^{'}$, and the mean, X, of the parent time history.

For the gamma distribution the estimates are given by the following equations:

Shape parameter:

$$\gamma = (\frac{2}{S})^{2} \tag{5.2}$$

Scale parameter :

$$\beta = \frac{x^{'}S}{2} \tag{5.3}$$

Location parameter:

$$\mu = X - (\frac{2x^{'}}{S}) \tag{5.4}$$

It should be noted that, for near-normal distributions, the skewness is low and therefore the value of γ becomes relatively large and $\Gamma(\gamma)$ approaches infinity. Tieleman et al. [39] showed that, invariably for other records, the differences between the distributions obtained with either the PPCC or the method of moments are negligibly small. Consequently, and because the PPCC method is inefficient in computational terms, the method of moments must be preferred because of its simplicity. Once the optimum marginal probability distribution and its parameters of the parent time history are established, the peak distribution can be obtained with the standard translation processes approach as described in detail by Sadek and Simiu [40]. From the obtained CDF of the peaks, the corresponding PDF can be obtained by differentiation. Moreover, the parameters for the CDF of the peaks can be used to obtain peak values for any level of non-exceedence with the expression for the Gumbel distribution written as

$$f(x) = exp(\frac{x-a}{b})exp(-exp(\frac{x-a}{b}))/b \tag{5.5}$$

Figure 5.32 shows the probability of non-exceedence for the time series presented in figures 5.12 and 5.13 and for one of the records obtained from pressure measurements at tap #8 in configuration 1 of the experiments by Tieleman et al. [11]. The results clearly show that the turbulent case yields a non-exceedence probability for the peak pressure coefficient that is

close to the one obtained from the measured data. It should be noted that a longer record for the turbulent inflow case should yield a larger intercept with the x-axis and adjust the slope to better match the slope of the probability calculated from the measured data.

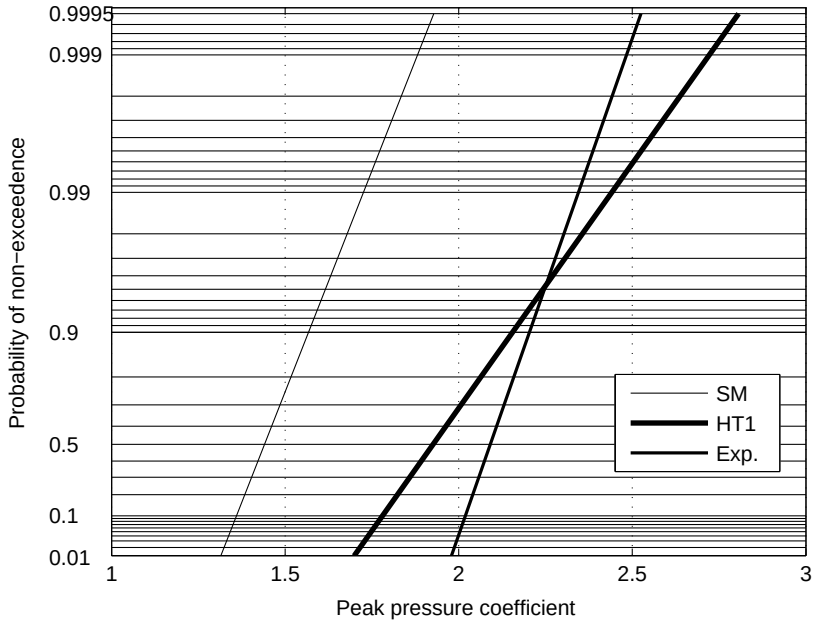

Figure 5.32: Comparison of probability of non-exceedence of peak pressure coefficient under smooth (SM) and turbulent inflow conditions (HT1) with probability estimated from experimental data (Exp.)

The results presented above show that the highest negative mean value of the pressure coefficient on the roof and the sides is about 30 % larger in the case of turbulent inflow and takes place closer to the windward edge of the prism. Moreover, the pressure coefficients on the roof and sides of the prism in the case of turbulent inflow show a higher level of variations in comparison with the case of smooth inflow conditions. The predicted mean characteristics of the pressure coefficients in the turbulent case match the experimental values in terms of both magnitude and location on the roof of the prism reported in Tieleman et al. [38].

Chapter 6

Linear/Nonlinear Velocity Pressure Relations

In this chapter, the wavelet, wavelet-based linear coherence and cross-bicoherence are introduced as effective tools to characterize short-time events such as the pressure peaks observed in chapter 5 in terms of their scales and their relation to different scales in associated velocity events. Definitions of a hierarchy of wavelet-based spectral moments are presented. Their applications to analytic signals show how these moments should be applied to obtain relevant physical insight. Finally, wavelet-based spectral moments are applied to time series of velocity components in the flow field and the surface pressure coefficients on the surface of the prism to investigate their linear and nonlinear relations.

6.1 Velocity-pressure Relation

The relation between the flow field and pressure fluctuations is of interest in the design and possibly control aspects of wind loads on structures. It is well known that this relation is governed by a Poisson's equation whereby the pressue fluctuations at a point are affected by

velocity fluctuations and flow structures in the whole flow field. Consequently, most studies have been concerned with relating turbulence structures in the flow field with specific pressure events. Our objective in this work is to statistically relate the wall pressure fluctuations to velocity fluctuations at different points in the flow field. In particular, the interest is in the linear and nonlinear relations between the different scales in the flow field and the scale that characterizes the pressure peaks as observed.

6.2 Analysis Procedure

Fourier-domain analysis is the most popular tool used for signal analysis. It is a technique used for transforming the signal from the time domain to a frequency domain. However, Fourier analysis is not suitable for the analysis of time varying characteristics of a signal. To overcome this shortcoming, one could use Gabor transform or short-time Fourier transform (STFT). The result is an analysis that yields information about both when and at what frequencies a signal event occurs. However, in the implementation of Short-Time Fourier transform, the size of the window is fixed for all frequencies and the time resolution is controlled by the size of the selected window. On the other hand, wavelet analysis is based on the use of windows whereby the time resolution increases with the central frequency of the window. As such, wavelet analysis presents a more efficient approach for the analysis of time varying phenomenon.

While frequency analysis is performed by projecting a signal onto a number of sinusoids which are infinite in extent, wavelet analysis is performed by projecting the signal onto a set of highly localized basis functions. These basis functions are called wavelets and are obtained from a single 'mother' wavelet by dilations and translations. Thus, in wavelet analysis, the notion of a scale replaces that of a frequency which leads to a time-scale representation (scalogram) with a high resolution. Since it is localized in time, a scale representation is more suitable than a frequency representation for examining the temporal characteristics of

the signal.

The continuous wavelet transform $W(a,\tau)$ of a function $h(t)$, is defined as:

$$W(a,\tau) = \int_{-\infty}^{\infty} h(t)\Psi^*_{a,\tau}(t)dt \tag{6.1}$$

where a and τ are scale and time variables, respectively, and $\Psi_{a,\tau}$ represents the wavelet family generated by continuous translations and dilations of the mother wavelet. These translations and dilations are obtained by

$$\Psi_{a,\tau} = \frac{1}{\sqrt{a}}\Psi(\frac{t-\tau}{a}) \tag{6.2}$$

Following [31] and [32], the Morlet wavelet [33] to be implemented in this study is defined as:

$$\Psi(t) = \pi e^{iw_o t}e^{(\frac{-t^2}{2})} \tag{6.3}$$

In this definition, w_o is chosen to be 6.0 to approximately satisfy the wavelet admissibility condition [34].

6.3 Definitions

The wavelet power spectrum is used to determine the energy of scale over a period of integration time T. It is defined by

$$P_{uu}(a) = \int_T W^*_u(a,\tau)W_u(a,\tau)d\tau \tag{6.4}$$

where $W_u(a,\tau)$ is the wavelet transform of the time series,$W^*_u(a,\tau)$ is its complex conjugate, and T is a finite time interval.

To study the relation between the same scale in two time series, one can define the wavelet cross-spectrum as [35, 36]

$$P_{uv}(a) = \int_T W^*_u(a,\tau)W_v(a,\tau)d\tau \tag{6.5}$$

where $W_u^*(a,\tau)$ is the complex conjugate of wavelet transform of the first time series and $W_v(a,\tau)$ is wavelet transform of the second time series.

It should be noted here that the results of the cross-spectrum depends on the fluctuations level of the individual signals in both amplitude and frequency. If one of the signals is less intense in terms of fluctuations than the other one, the signal with higher intensity dominates the resultant cross-spectrum [15].

The normalized wavelet-based cross-spectrum, namely the linear coherence (to have values between 0 and 1) is defined [35, 36] as:

$$Coh_{uv}(a) = \frac{|P_{uv}(a)|^2}{P_{uu}(a)P_{vv}(a)} \tag{6.6}$$

and is used as a measure of coherence between the same scale in two signals. A value near one for the linear coherence indicates that the two scales in the two signals are highly correlated over the time of integration. A near zero value indicates no coupling. Any value in between indicates partial coupling.

The wavelet cross-bispectrum is defined in [35, 36] as:

$$B_{vuu}(a_1,a_2) = \int_T W_v^*(a,\tau)W_u(a1,\tau)W_u(a2,\tau)d\tau \tag{6.7}$$

where

$$\frac{1}{a} = \frac{1}{a_1} + \frac{1}{a_2} \tag{6.8}$$

Where equation 6.8 represents the frequency sum rule. The wavelet cross-bispectrum measures the level of phase coupling in the interval T that occurs between wavelet components of scale lengths a_1 and a_2 in one signal and wavelet component a in a second signal [35].

The normalized squared wavelet cross-bicoherence with values between 0 and 1, defined as:

$$[b_{vuu}(a_1, a_2)]^2 = \frac{|B_{vuu}(a_1, a_2)|^2}{[\int_T |W_u(a_1, \tau)W_u(a_2, \tau)|^2 d\tau][\int_T |W_v(a, \tau)|^2 d\tau]} \tag{6.9}$$

is used as a measure of the quadratic coupling between scales a_1 and a_2 in one signal and scale a in the second one. A value of one indicates perfect coupling, a near zero value indicates no coupling. Any value in between indicates partial coupling.

Relation between Scale and Frequency

To determine the coupling between frequency components in the pressure and velocity signals, the scale is converted to frequency as suggested in [31] for Morlet wavelet, i.e.

$$f = \frac{d}{a} \tag{6.10}$$

where

$$d = \frac{w_o + \sqrt{2 + w_o^2}}{4\pi} \tag{6.11}$$

Hence, w_o is chosen to be 6.0 to approximately satisfy the wavelet admissibility condition [34]. Consequently, equations 6.10 and 6.11 yield a relation between f and a that is given by $f = \frac{0.97}{a}$

6.4 Test of Quadratic Relation between Two Signals

To test the use of the cross-bicoherence for the detection of the non-linearity between two signals, three sets of test signals are analyzed. The first set consists of two signals that have frequencies equal to 1.0 Hz, and 2.0 Hz as shown in figure 6.1. The computed wavelet scalogram presented in figure 6.2 of the two signals shows that applying the wavelet transform yields high energy levels over the frequency ranges, near 1 and 2 Hz. The linear coherence and wavelet bicoherence for different ranges of time integration are presented in Figures 6.3,

6.4, 6.5, and 6.6, respectively. The linear coherence plot in figure 6.3 shows the low level of coherence over both frequency ranges near 1 and 2 Hz, which is expected. One should also note the high level of coherence in the low frequency ranges when the integration time period is high. This is due to statistical noise as explained in [35]. It is obvious in figure 6.1 that the phase relation between the two frequency components of the two signals is constant. Consequently, one should expect a high level of coupling over any integration period. This is shown in figures 6.4, 6.5, and 6.6, which show high levels of cross-bicoherence between 1 Hz in the first signal and 2 Hz in the second one. It should be noted here also that the smaller the time of integration is, the higher the noise is at the lower frequencies.

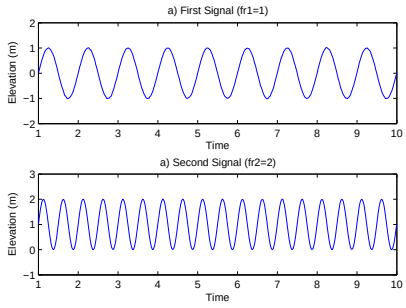

Figure 6.1: Two test signals with different frequency,($\Delta t = 0.02$)

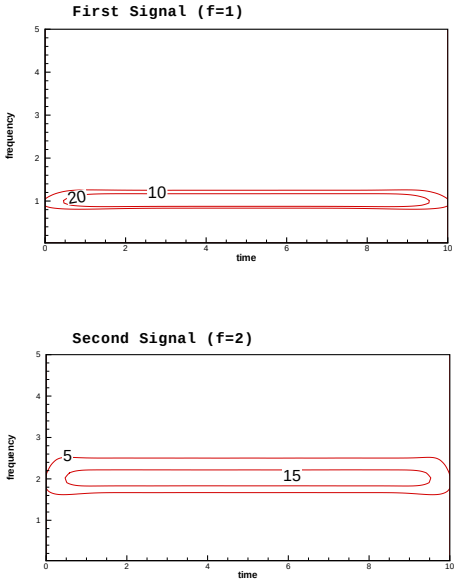

Figure 6.2: Wavelet transform of the test signals given in Figure 6.1

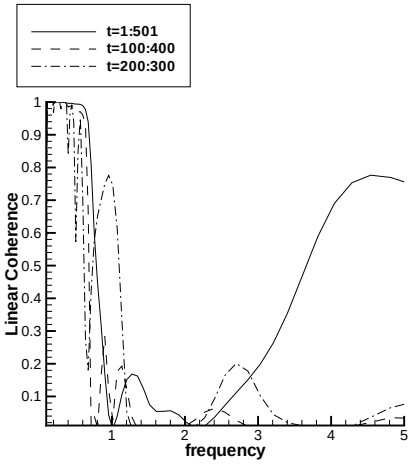

Figure 6.3: Linear coherence between the two signals given in Figure 6.1

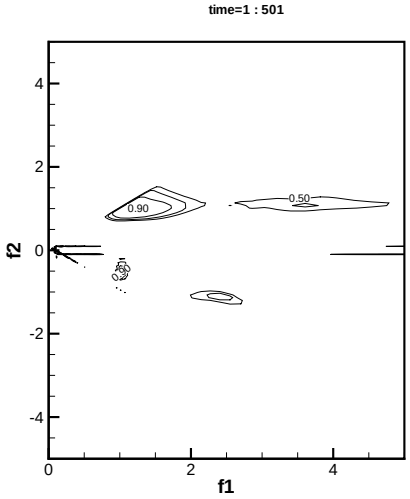

Figure 6.4: Bicoherence between the two signals given in Figure 6.1

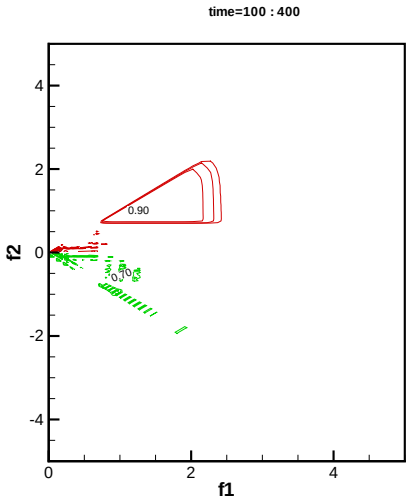

Figure 6.5: Bicoherence between the two signals given in Figure 6.1

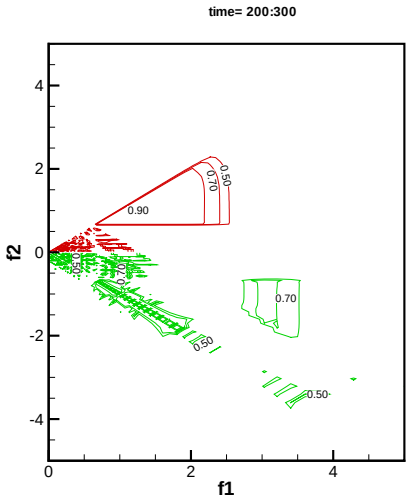

Figure 6.6: Bicoherence between the two signals given in Figure 6.1

A second set of two signals with frequencies equal to 10.0 Hz, 20.0 Hz (Figure 6.7) was used to demonstrate the capability of the wavelet-based cross-bicoherence in the detection of phase coherence between scales that satisfy the summation rule in different signals. The computed wavelet transform of the two time series is shown in Figure 6.8. The results clearly show the high level of energy in the first signal over the frequency range near 10 Hz and in the second signal over the frequency range near 20 Hz. The linear coherence and wavelet cross-bicoherence for different ranges of time integration are presented in Figures 6.9, 6.10, 6.11, and 6.12 respectively. Figure 6.9 shows low values of linear coherence over the frequency range above 10 Hz for all integration times. Figures 6.10, 6.11, and 6.12 show respectively the cross-bicoherence between the signals presented in Figure 6.7 estimated over three different integration times. The results show the high level of coupling ≥ 0.9 between 10 Hz and 10 Hz in the sum region. To be noted also, is significant increase in the level of noise at the low frequencies as the time of integration is decreased.

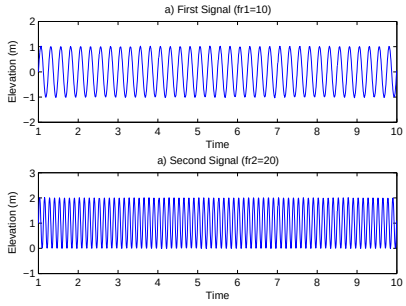

Figure 6.7: Two test signals with different frequency,($\Delta t = 0.002$)

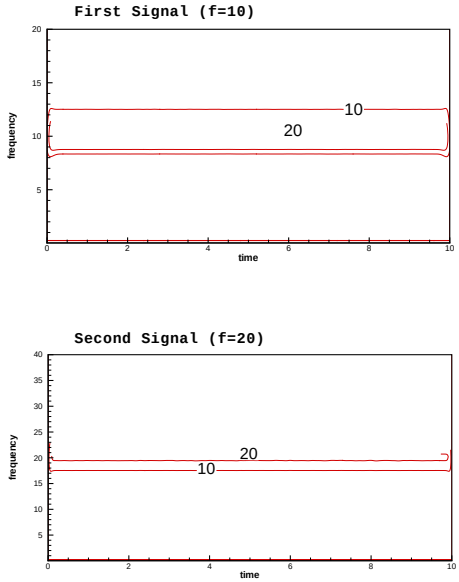

Figure 6.8: Wavelet transform of the test signals given in Figure 6.7

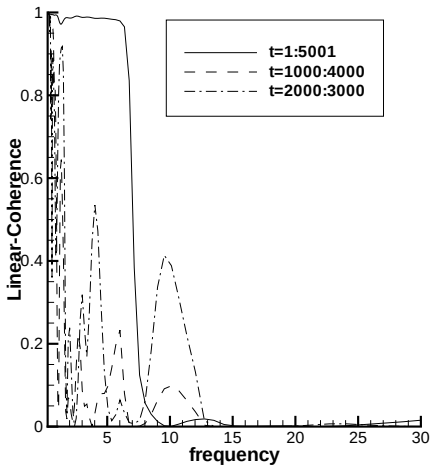

Figure 6.9: Linear coherence between the two signals given in Figure 6.7

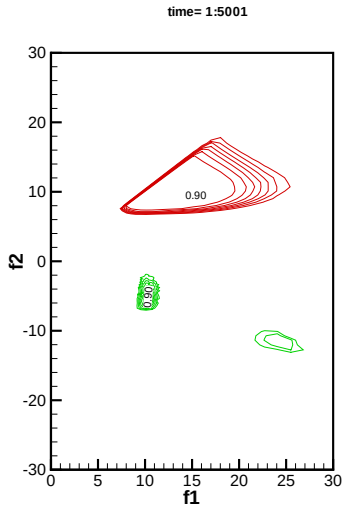

Figure 6.10: Bicoherence between the two signals given in Figure 6.7

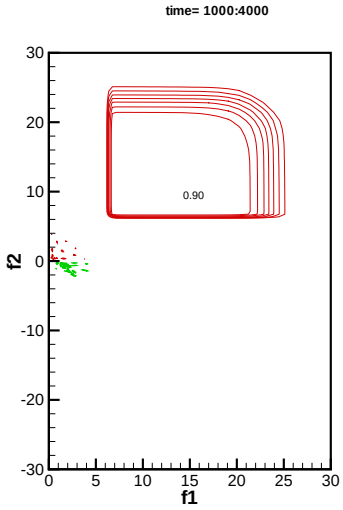

Figure 6.11: Bicoherence between the two signals given in Figure 6.7

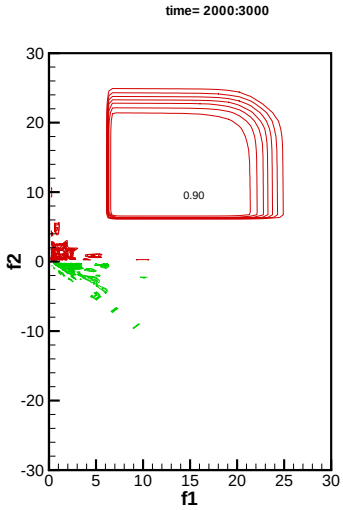

Figure 6.12: Bicoherence between the two signals given in Figure 6.7

The third set involves two signals with frequencies equal to 10.0 Hz, and 20.0 Hz. Yet, their phase coupling is established over separated time periods as shown in figure 6.13. Obviously, the two signals are coupled over the nondimensional time ranges between 0 and 1.2 and between 4 and 10. Additionally, one of the two signals or the other disappears between 1.2 and 4. The computed wavelet transform presented in figure 6.14, shows the high levels of

energy in the two signals over the frequency ranges near 10 Hz, in the first one, and near 20 Hz in the second one with intermittent disappearance of this energy over the times during which the signal disappeared.

The linear coherence and wavelet bicoherence for different ranges of time integration are presented in figures 6.15, 6.16, 6.17, and 6.18, respectively. For all integration times, the wavelet linear coherence shows low levels, which is expected since the two signals have different frequency components. Of interest is the comparison of the contour plots of the cross-bicoherence in figures 6.16, 6.17, and 6.18. These three plots represent, respectively, cross-bicoherence estimates by integration over the full record, over a time when either of the frequency components in the two signals disappears and over a time when both components were present. The results clearly show the high level of coupling (≥ 0.9) when the integration interval consisted of the time when frequency components existed in both signals. In comparison, Figure 6.17 shows no coupling and that should be the case since the time of integration covers a period when either of the two signals does not contain any frequency components. When the integration time is carried over the full record a partial coupling (≈ 0.7) is detected.

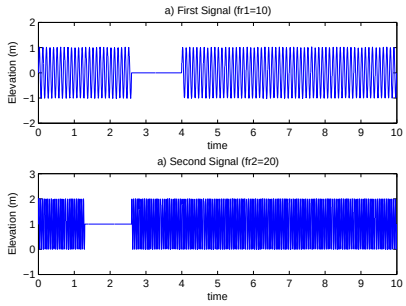

Figure 6.13: Two test signals with different frequency,($\Delta t = 0.002$)

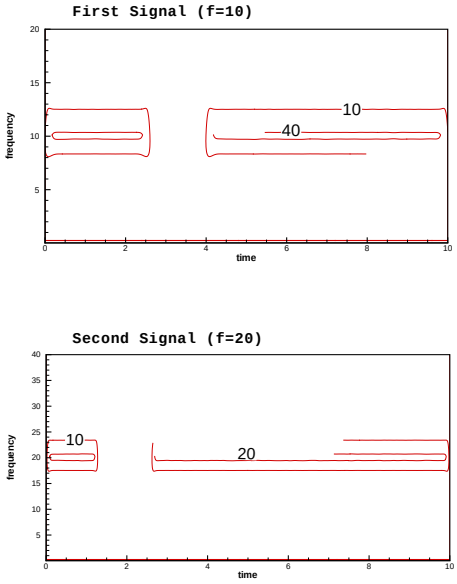

Figure 6.14: Wavelet transform of the test signals given in Figure 6.13

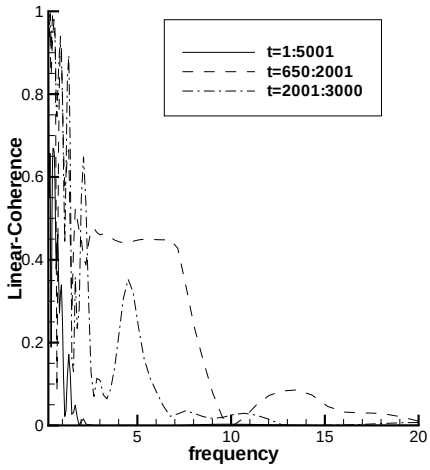

Figure 6.15: Linear coherence between the two signals given in Figure 6.13

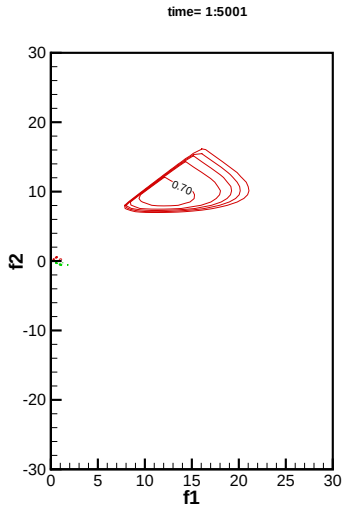

Figure 6.16: Bicoherence between the two signals given in Figure 6.13

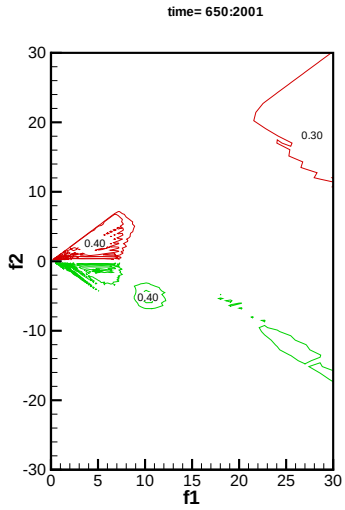

Figure 6.17: Bicoherence between the two signals given in Figure 6.13

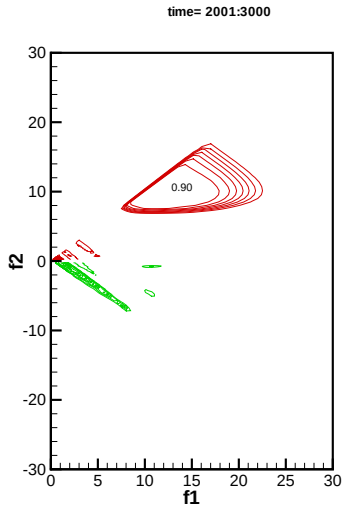

Figure 6.18: Bicoherence between the two signals given in Figure 6.13

6.5 Linear and Quadratic Coupling between Surface Pressure and Velocity Fluctuations

In this section, wavelet analysis is applied to time series of pressure coefficients on the surface and the three time series of velocity components at different points in the flow field. The objective is to investigate the relation between the pressure fluctuations and the velocity fluctuations. The time series of the pressure coefficients and the three velocity components (u,v,w) at $Z/H = 1.01$ are presented in figure 6.19. Of interest in the pressure time series is the peak observed near the arbitrary time $t = 10$. The scalogram of the wavelet transform shows a peak near that time over the frequency range around 0.25. Additionally, the plot shows a high level of energy in the frequency range around 0.12, over the time period t between 6 and 23. The scalogram of the u-component shows high energy levels over the frequency range around 0.3, approximately over the same time period over which the pressure peak takes place. While the v-component shows a high level of energy over the frequency range near 0.1, the w-component seems to have the best correlated, in time, event in that

it shows high energy levels in the frequency range near 0.45 around the time of occurance of the peak, $t = 10$. These results give an insight that the scale of the pressure peak is associated with certain scales in the velocity components.

The linear coherence and cross-bicoherence between the pressure coefficients and velocity components are calculated over two time periods. The first time period covers the whole time series, while, we choose a smaller time of integration in the second case to analyze the peak suction pressure as observed in the time series. The results are presented in figures 6.20, 6.21, 6.22, 6.23, respectively. The linear coherence between all velocity components and Cp, show a high value in the frequency range near 0.12. When the time of integration is reduced to cover only the peak duration, the linear coherence levels increase significantly, especially at the frequency ranges that showed high energy levels in the wavelet spectra. Figure 6.22 shows the cross-bicoherence for the three combinations u,u,p, v,v,p and w,w,p. For the combination u,u,p, there is a high value observed between 0.3 and -0.15, while in the case of v,v,p, there are regions of high values observed near the frequency ranges given by $(0.1, 0.1)$ and $(0.3, -0.1)$.For the combination w,w,p high values are observed in the frequency ranges given by $(0.2, -0.1)$ and $(0.1, 0.1)$. Lower levels are obtained in the range $(0.35, -0.1)$. On the other hand, the computed cross-bicoherence considering a shorter time of integration shows that the levels increase signficantly (Figure 6.23). The computed linear coherence and cross-bicoherence show that there are both linear and nonlinear relationships between the pressure coefficients and the three velocity components at surface ($Z/H = 1.01$) of the low-rise building. In particular, the scale of the pressure peak can be related linearly to the u-component and nonlinearly to the w-component.

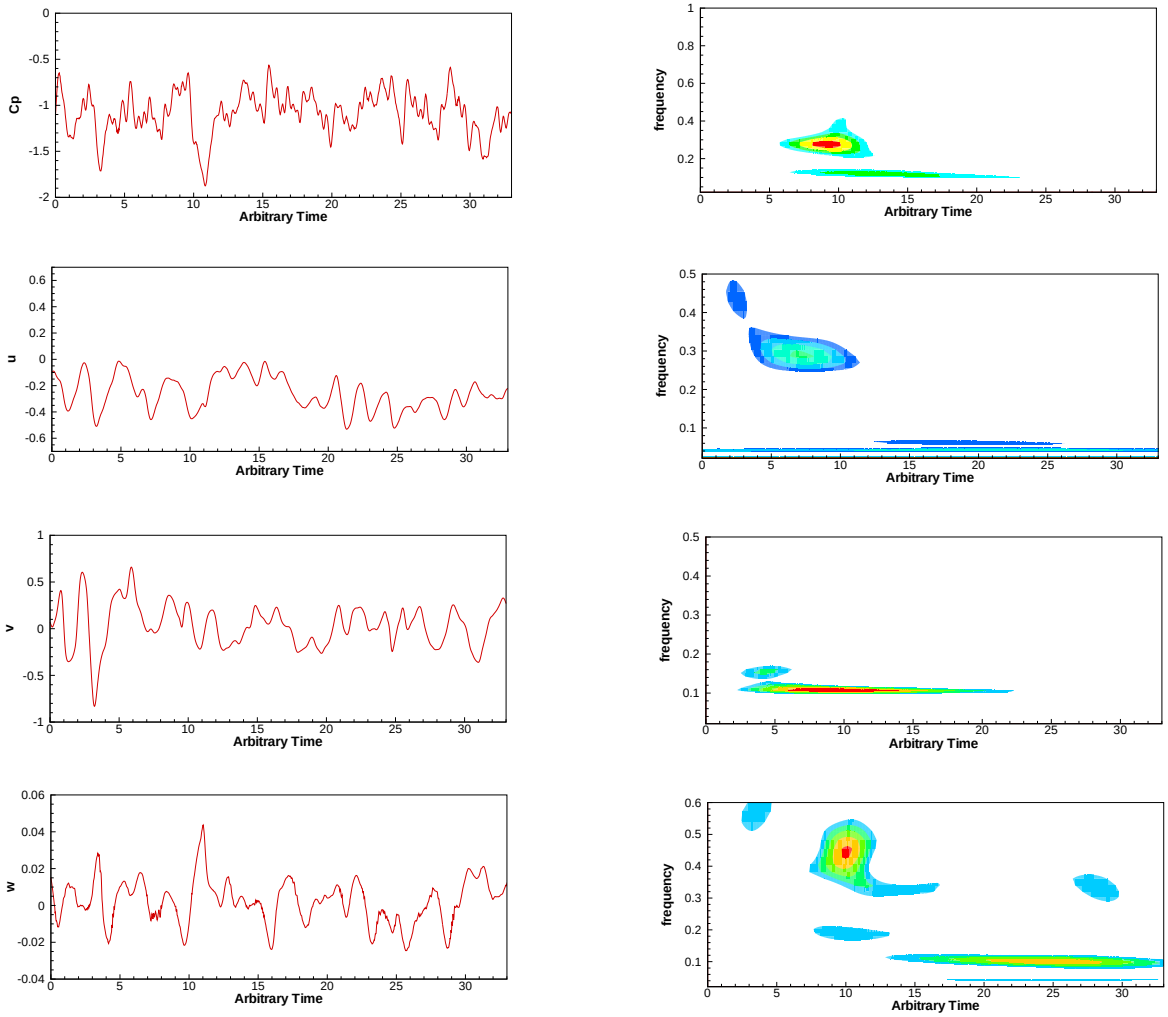

Figure 6.19: Pressure (Z/H=1.01) and velocity field (Z/H=1.01) and their wavelet transforms. Contour levels are set at 4, 4.833, 6.667, 6.5

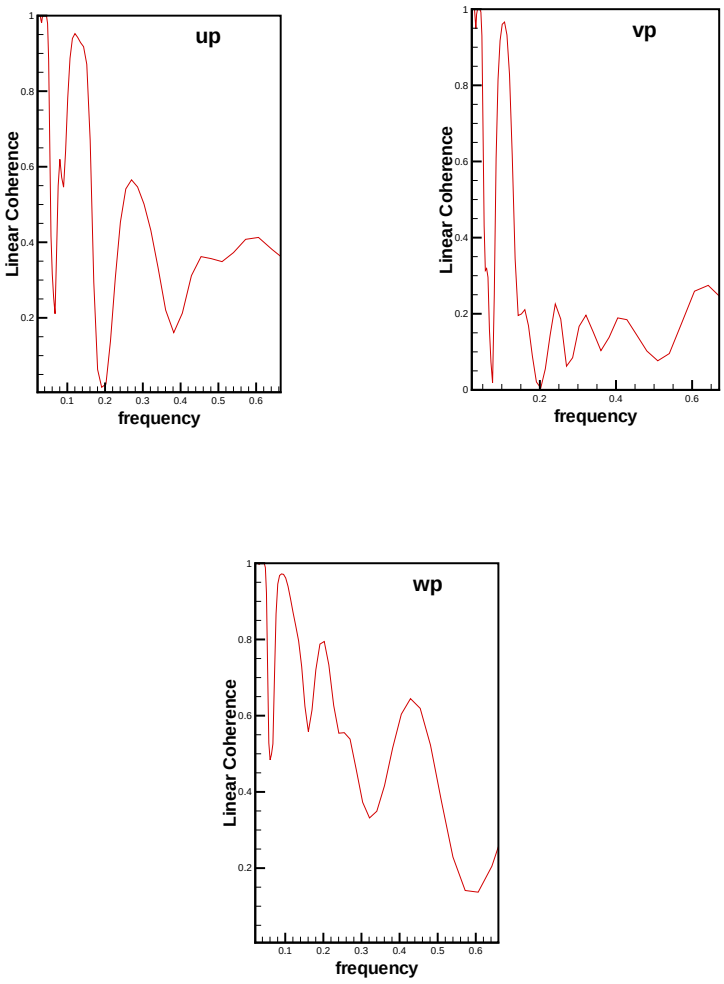

Figure 6.20: Wavelet linear coherence between velocity vectors (Z/H=1.01) and pressure (Z/H=1.01), time of integration=2.36:30.68

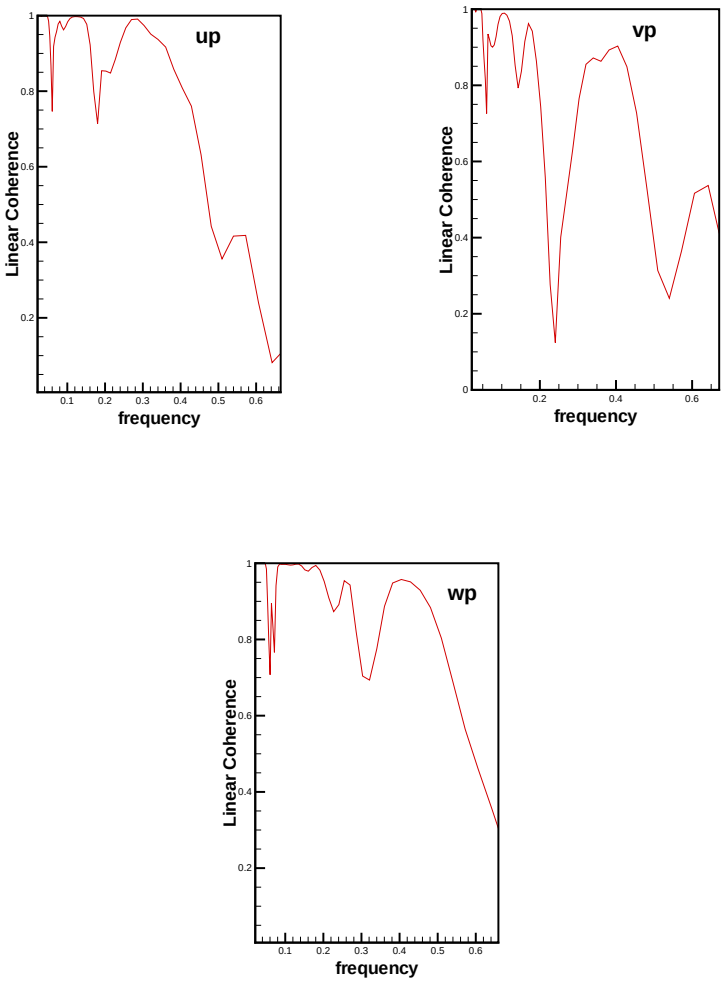

Figure 6.21: Wavelet linear coherence between velocity vectors (Z/H=1.01) and pressure (Z/H=1.01), time of integration=7.08:14.16

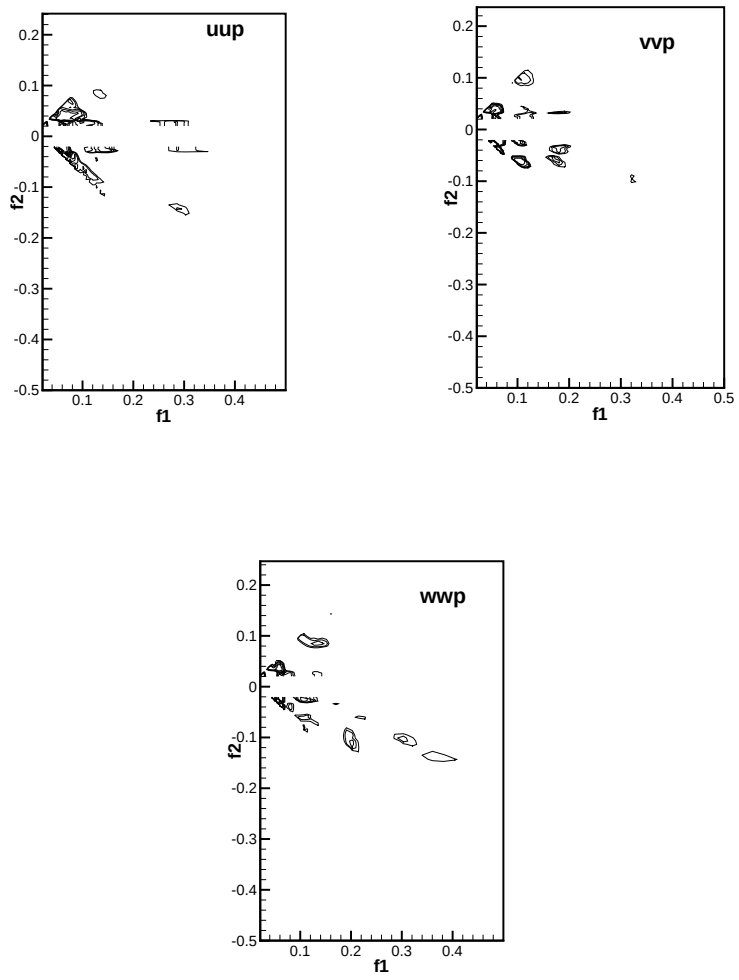

Figure 6.22: Wavelet cross-bicoherence between velocity vectors (Z/H=1.01) and pressure (Z/H=1.01), time of integration=2.36:30.68. Contour levels are set at 0.7, 0.7625, 0.825, 0.8875, 0.95

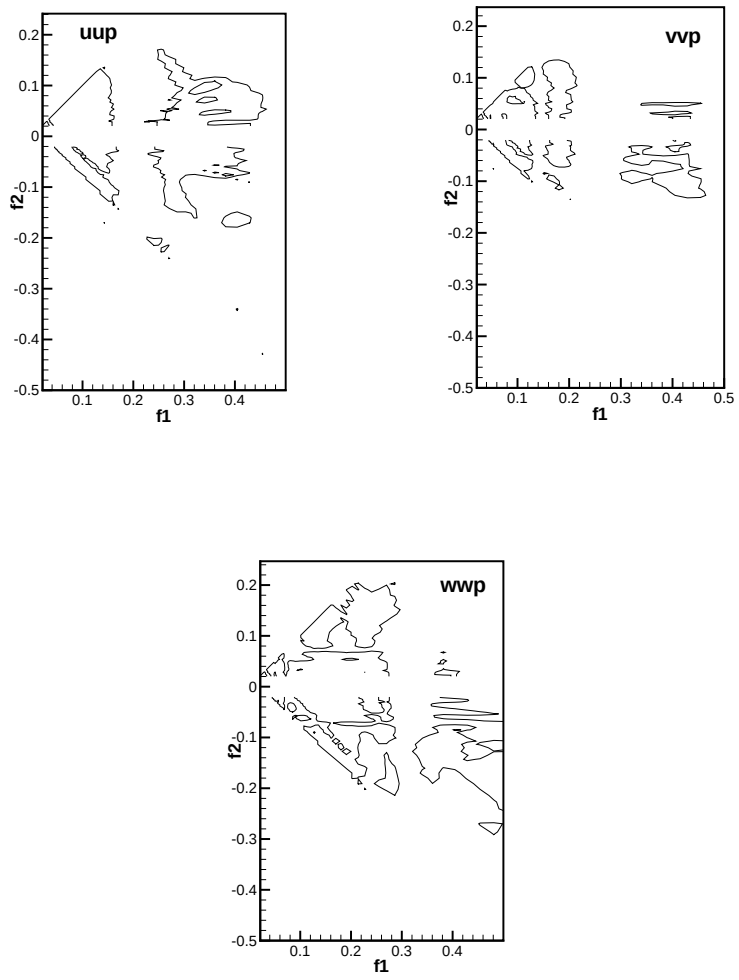

Figure 6.23: Wavelet cross-bicoherence between velocity vectors (Z/H=1.01) and pressure (Z/H=1.01), time of integration=7.08:14.16. Contour level is set at 0.90

In this section the linear and nonlinear relations between the surface pressure fluctuations and the different velocity components at $Z/H = 1.04$ are determined. A plot of the time series considered and their respective scalograms are presented in figure 6.24. Only the u-component shows a clear relation in terms of scale and time period between the pressure peak and a velocity event. The relation with the v- and w- components is less clear. The linear coherence and cross-bicoherence between the pressure coefficients and velocity components

considering two ranges of time integration are then obtained. The first time of integration covers the whole time series, while, we chose a smaller time of integration in the second case that covers the peak suction pressure as observed in the pressure coefficient time series. The results are presented in figures 6.25, 6.26,6.27, 6.28 respectively. Linear coherence between the pressure coefficient and the three velocity components is presented in figure 6.25. The results show a relatively high peak near the frequency range of 0.25 which corresponds to the scale of the pressure peak. Figure 6.26 shows a higher level of coherence among all frequency components in comparison with levels obtained in figure 6.25.Yet, of interest to note is the fact that the level of linear coherence remains relatively small at the scale of the pressure peak, 0.25. This implies a certain level of nonlinear coupling. Figure 6.27 gives the computed cross-bicoherence for u,u,p; v,v,p and w,w,p. For u,u,p, there is a high value observed over the frequency range $(0.3, -0.1)$. In the case of v,v,p, regions of high values are observed near $(0.1, 0.1)$ and $(0.2, -0.05)$. For w,w,p the high value is observednear $(0.1, 0.15)$ and $(0.2, -0.1)$. Yet of particular interest is the relatively high level of coupling between 0.38 and -0.15 which sums to the frequency associated with the pressure peak.The computed cross-bicoherence over a shorter time of integration shows that the levels increase signficantly (Figure 6.28). The computed linear coherence and cross-bicoherence show that there are both linear and nonlinear relationships between the pressure coefficients at $Z/H = 1.01$ and the three velocity components at $Z/H = 1.04002$.

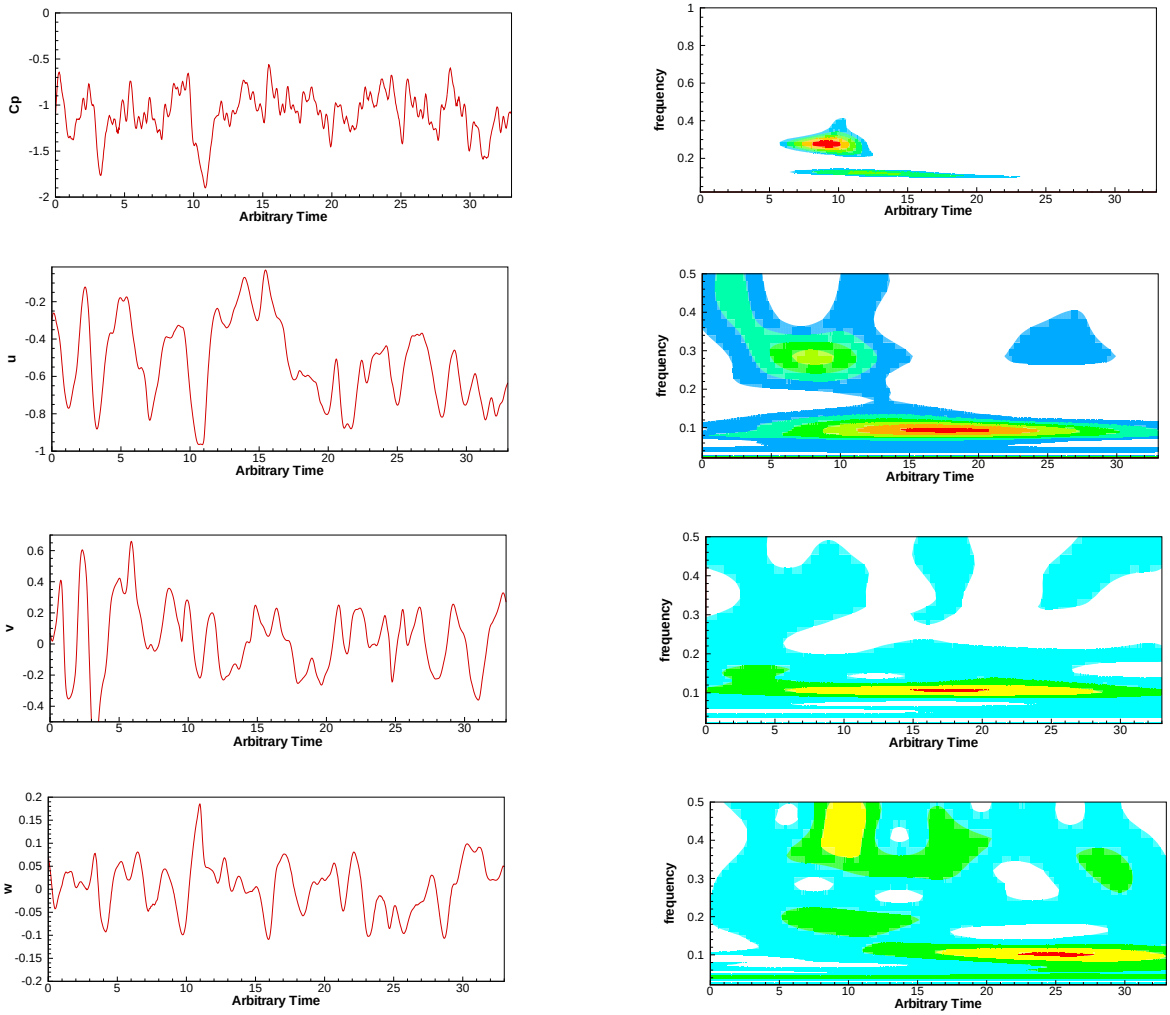

Figure 6.24: Pressure (Z/H=1.01) and velocity field (Z/H=1.04002) and their wavelet transforms. Contour levels are set at 4, 4.833, 6.667, 6.5

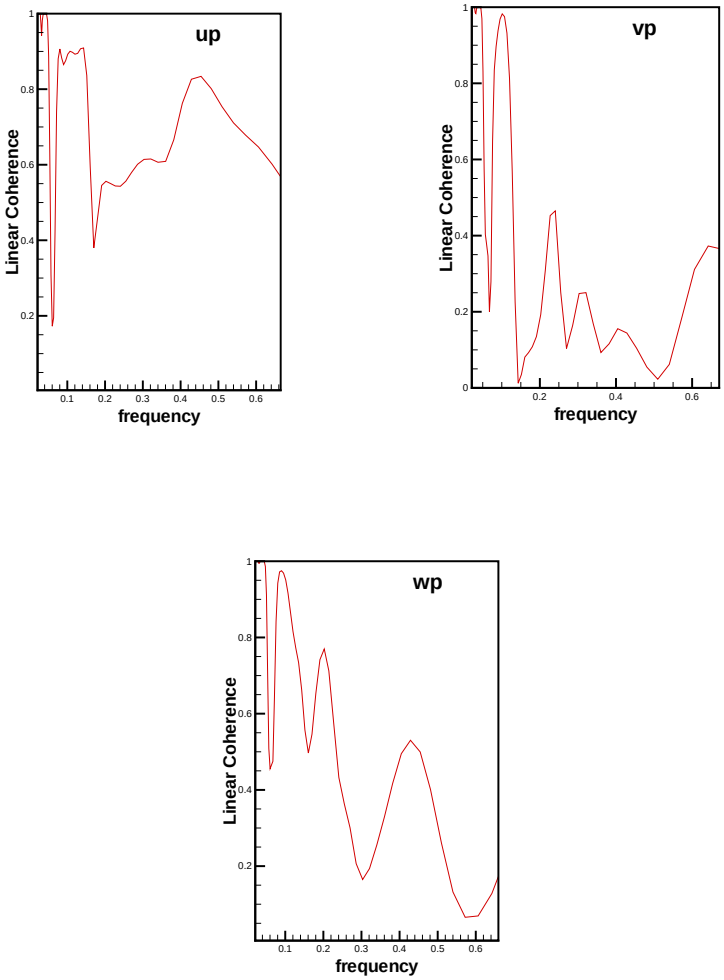

Figure 6.25: Wavelet linear coherence Coherence between velocity vectors (Z/H=1.04002) and pressure (Z/H=1.01), time of integration=2.36:30.68

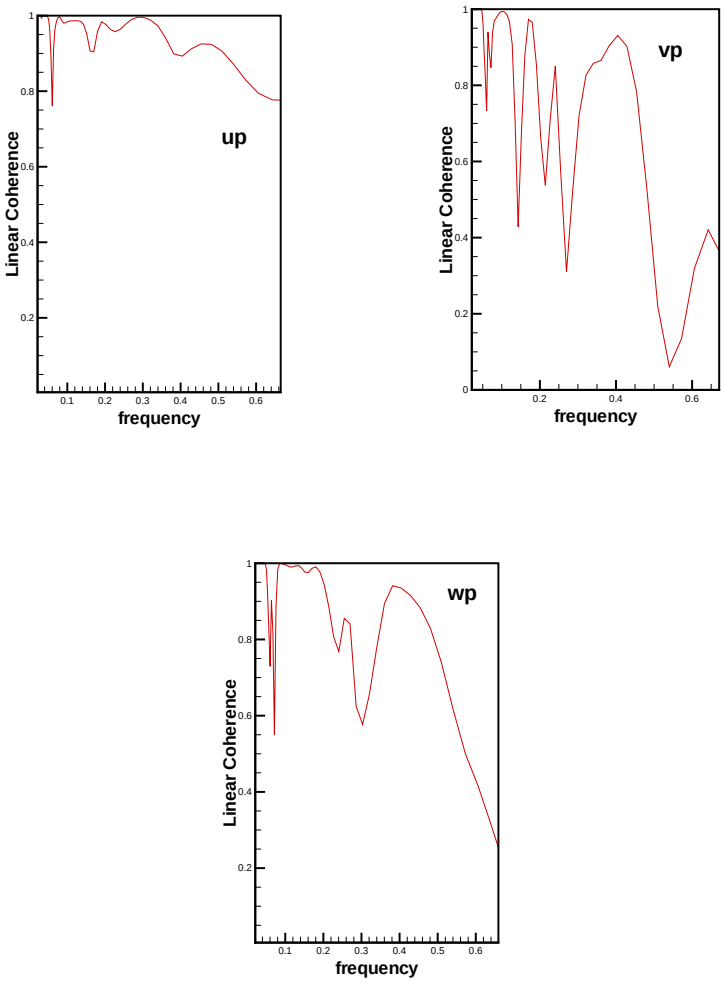

Figure 6.26: Wavelet linear coherence Coherence between velocity vectors (Z/H=1.04002) and pressure (Z/H=1.01), time of integration=7.08:14.16

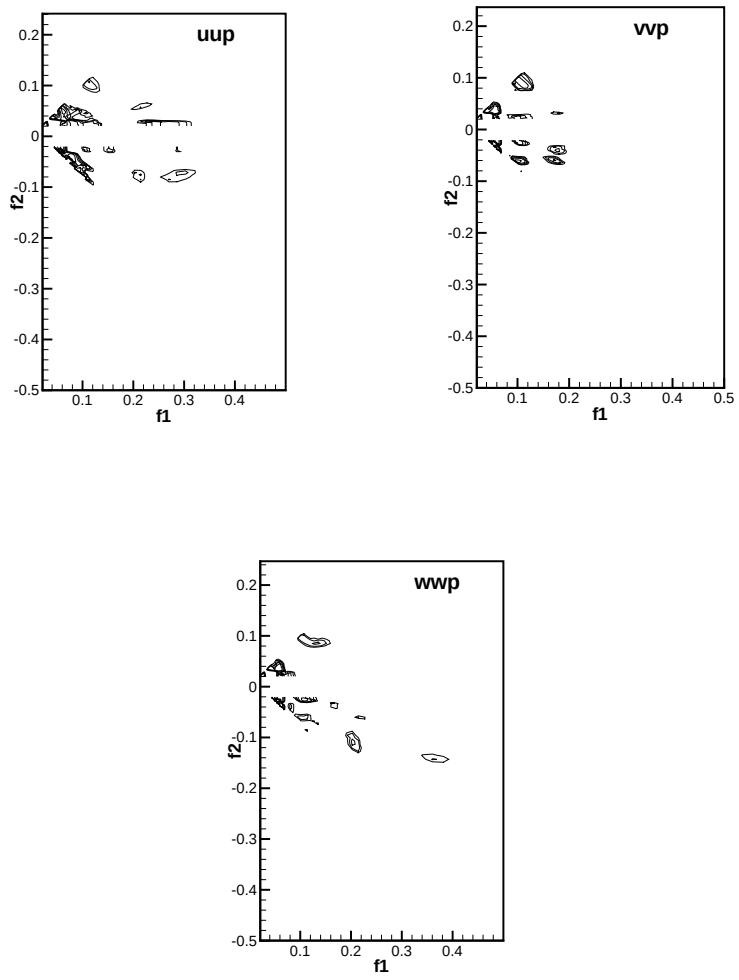

Figure 6.27: Wavelet cross-bicoherence between velocity vectors (Z/H=1.04002) and pressure (Z/H=1.01), time of integration=2.36:30.68. Contour levels are set at 0.7, 0.7625, 0.825, 0.8875, 0.95

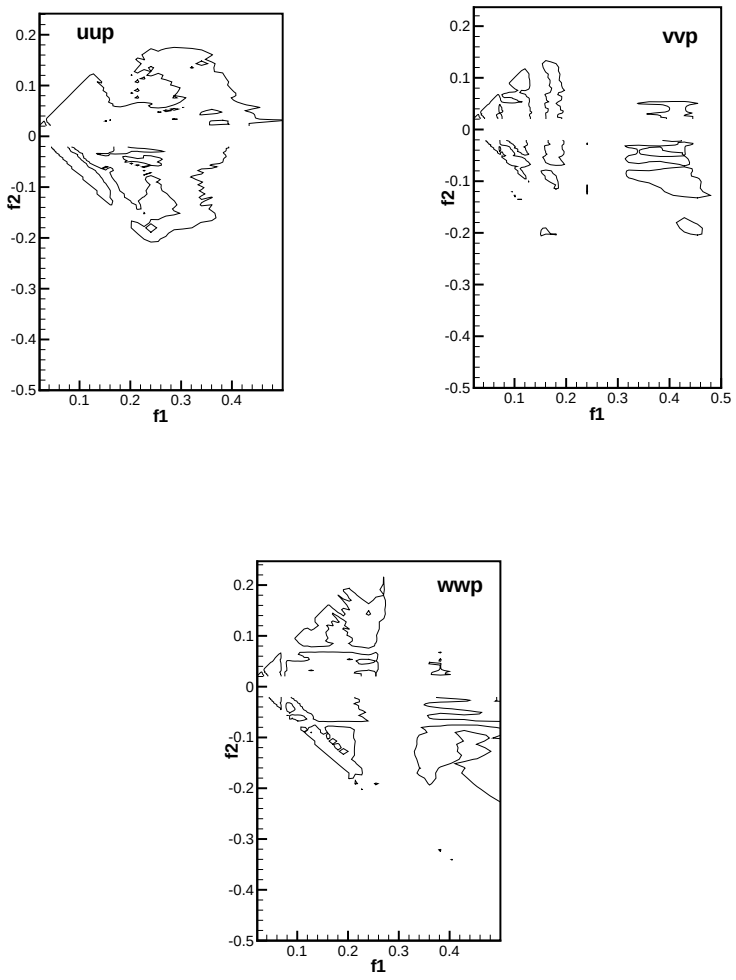

Figure 6.28: Wavelet cross-bicoherence between velocity vectors (Z/H=1.04002) and pressure (Z/H=1.01), time of integration=7.08:14.16. Contour level is set at 0.90

Analysis of the linear and quadratic relation between surface pressure fluctuations and the three components of the velocity fluctuations in the near field (up to $Z/H = 1.65$) revealed the same mechanisms discussed above. The results are presented in figures 6.29-6.43.

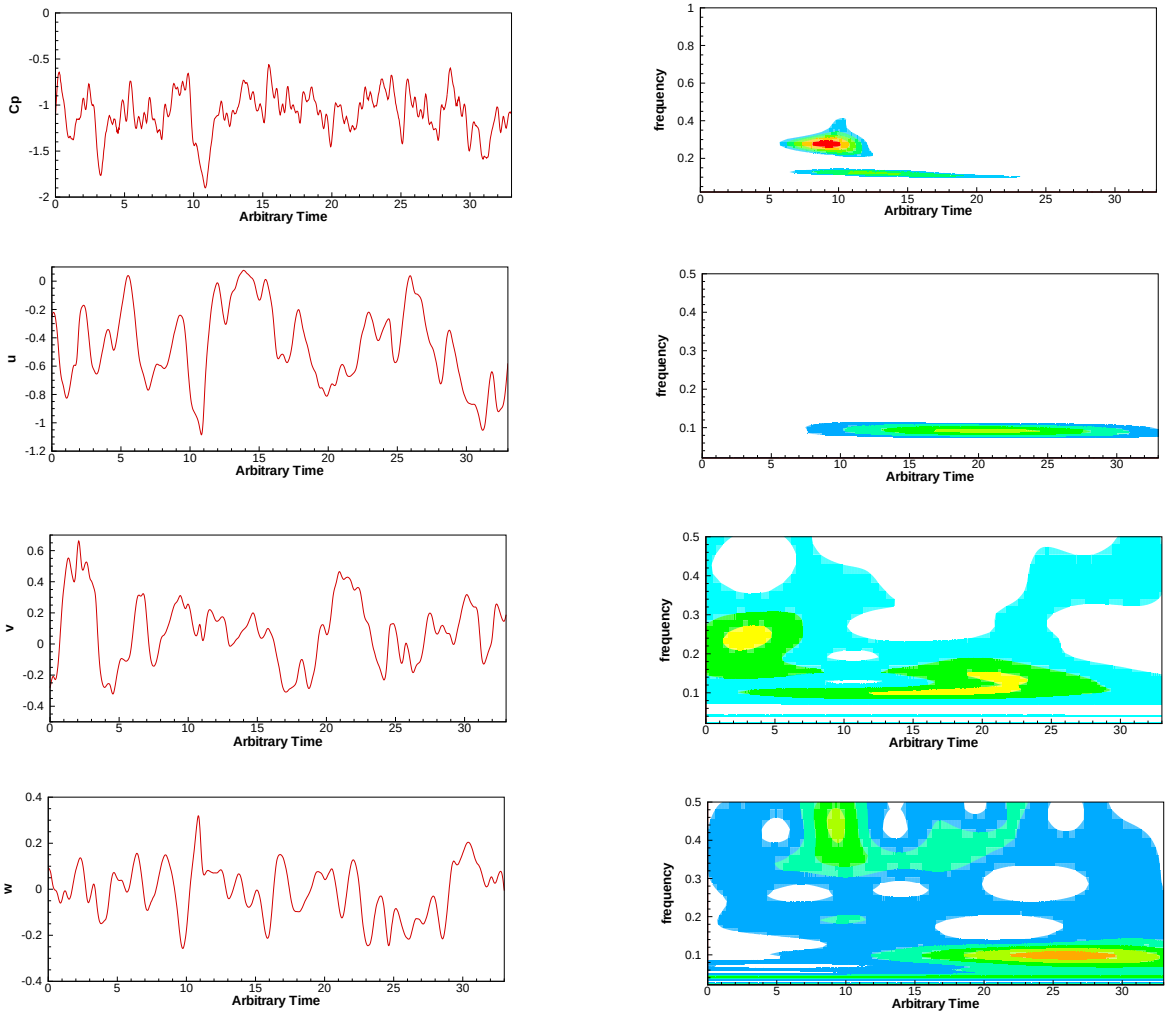

Figure 6.29: Pressure (Z/H=1.01) and velocity field (Z/H=1.08095) and their wavelet transforms. Contour levels are set at 4, 4.833, 6.667, 6.5

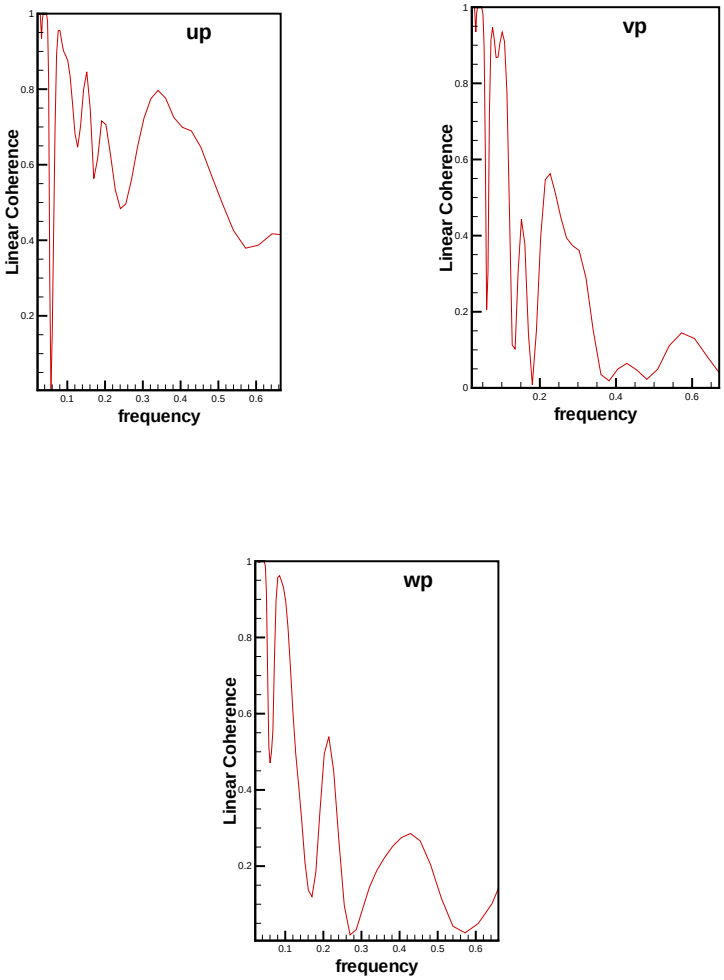

Figure 6.30: Wavelet linear coherence between velocity vectors (Z/H=1.08095) and pressure (Z/H=1.01), time of integration=2.36:30.68

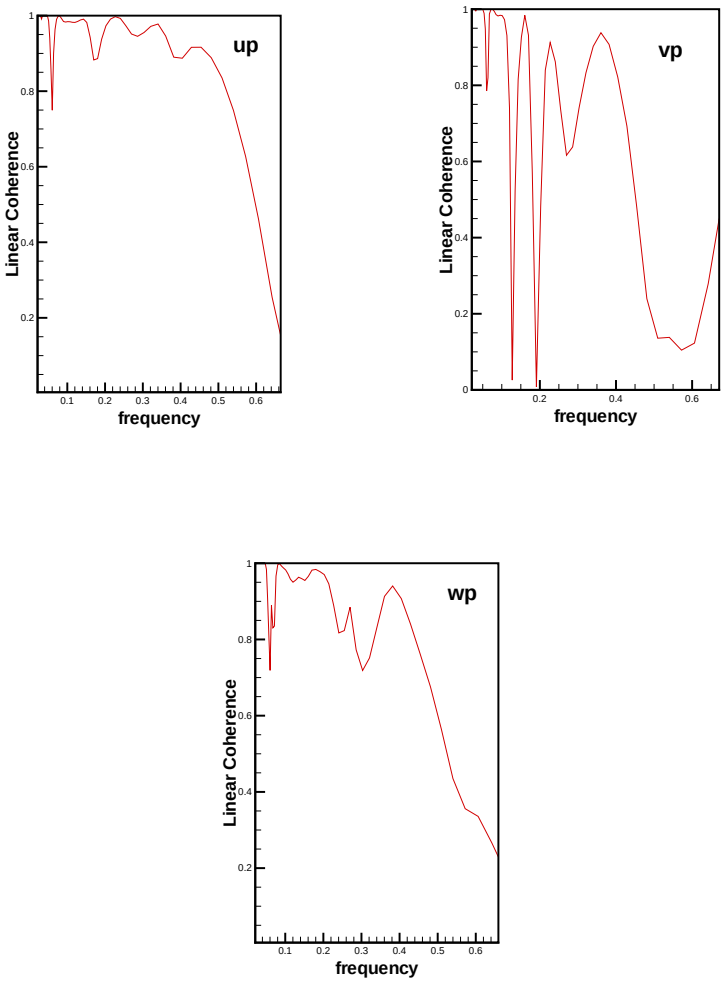

Figure 6.31: Wavelet linear coherence between velocity vectors (Z/H=1.08095) and pressure (Z/H=1.01), time of integration=7.08:14.16

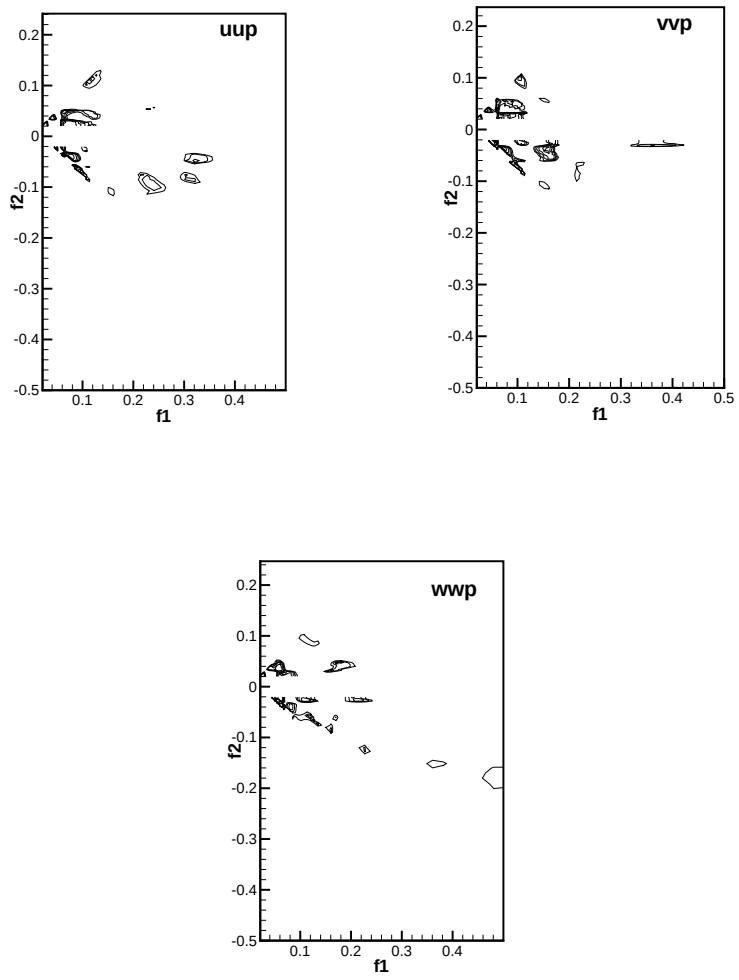

Figure 6.32: Wavelet cross-bicoherence between velocity vectors (Z/H=1.08095) and pressure (Z/H=1.01), time of integration=2.36:30.68. Contour levels are set at 0.7, 0.7625, 0.825, 0.8875, 0.95

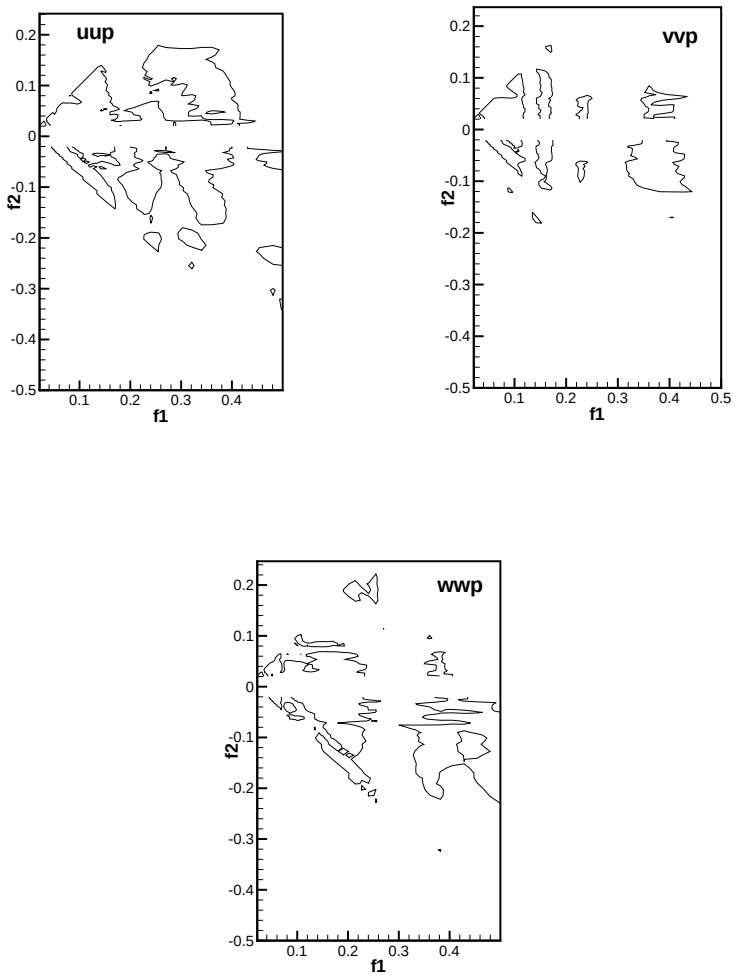

Figure 6.33: Wavelet cross-bicoherence between velocity vectors (Z/H=1.08095) and pressure (Z/H=1.01), time of integration=7.08:14.16. Contour level is set at 0.90

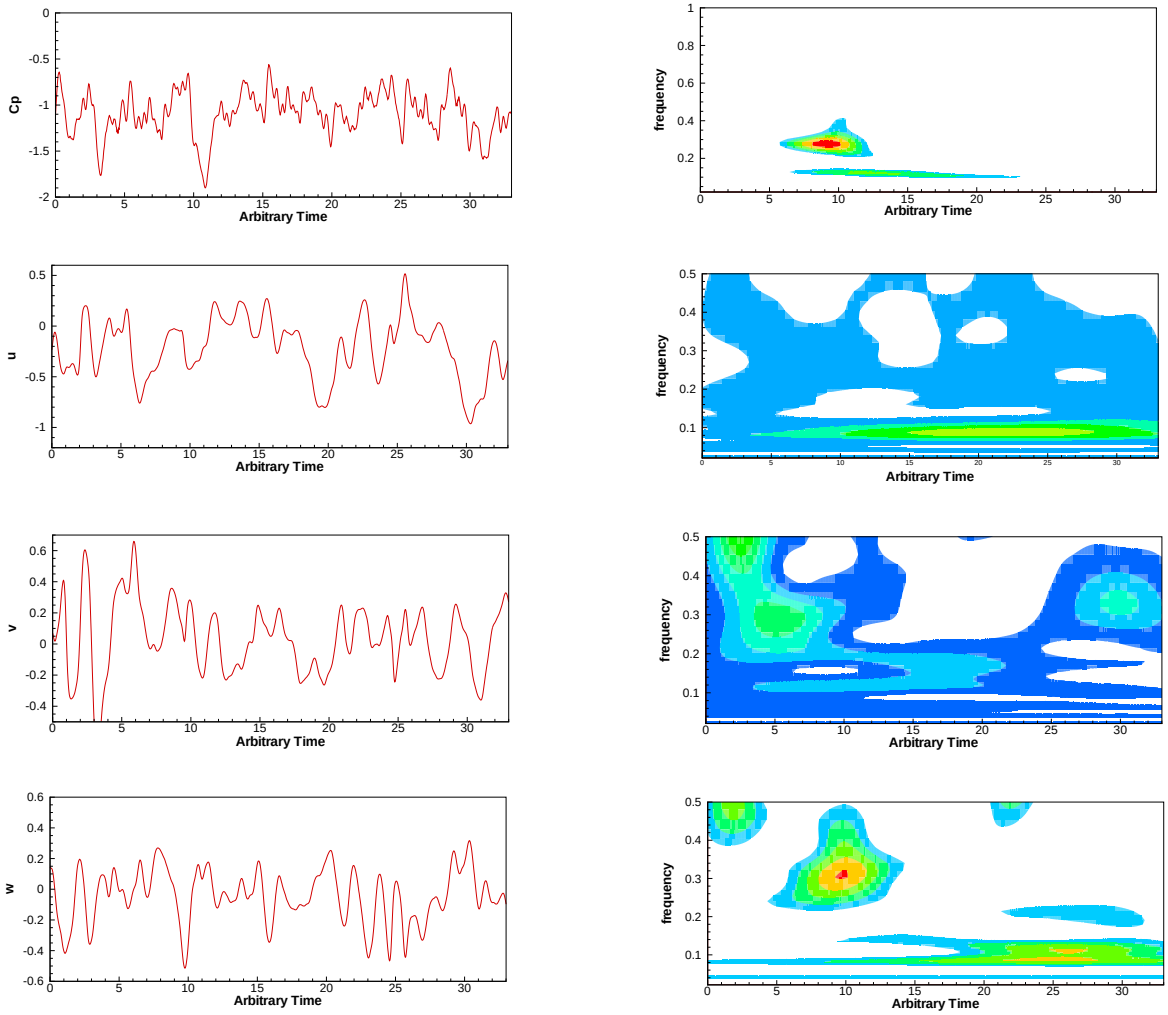

Figure 6.34: Pressure (Z/H=1.01) and velocity field (Z/H=1.18090) and their wavelet transforms. Contour levels are set at 4, 4.833, 6.667, 6.5

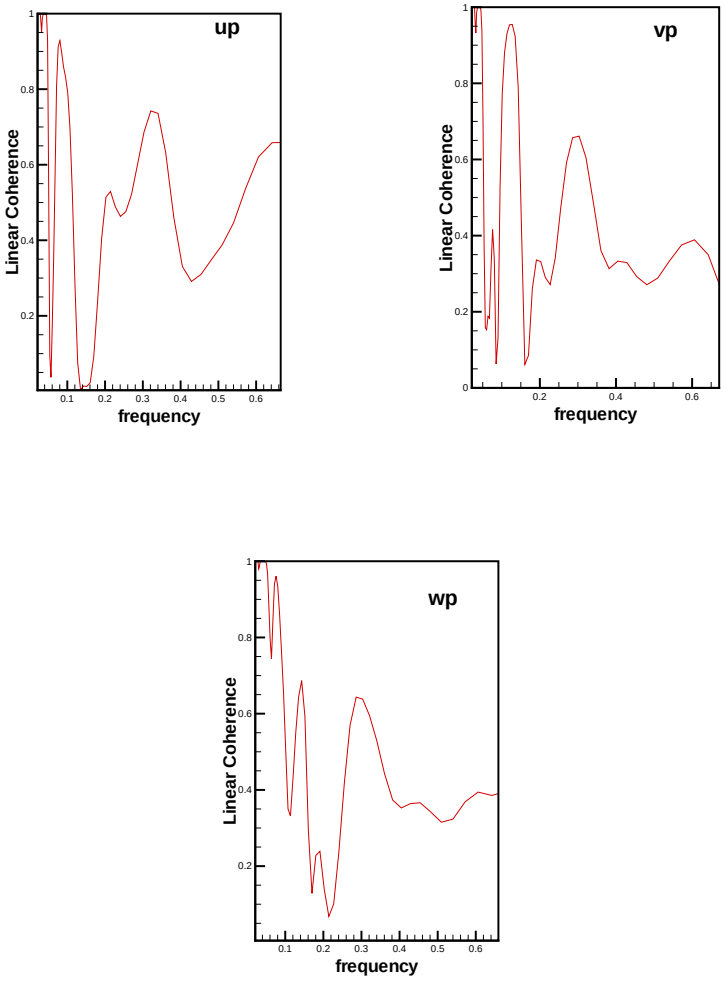

Figure 6.35: Wavelet linear coherence between velocity vectors (Z/H=1.18090) and pressure (Z/H=1.01), time of integration=2.36:30.68

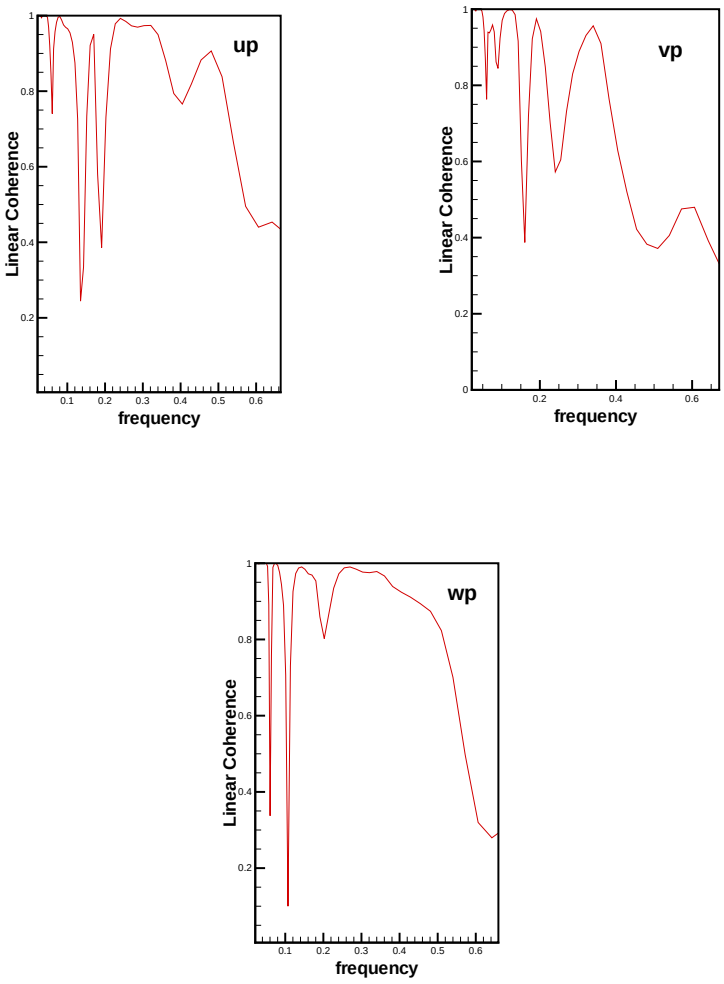

Figure 6.36: Wavelet linear coherence between velocity vectors (Z/H=1.18090) and pressure (Z/H=1.01), time of integration=7.08:14.16

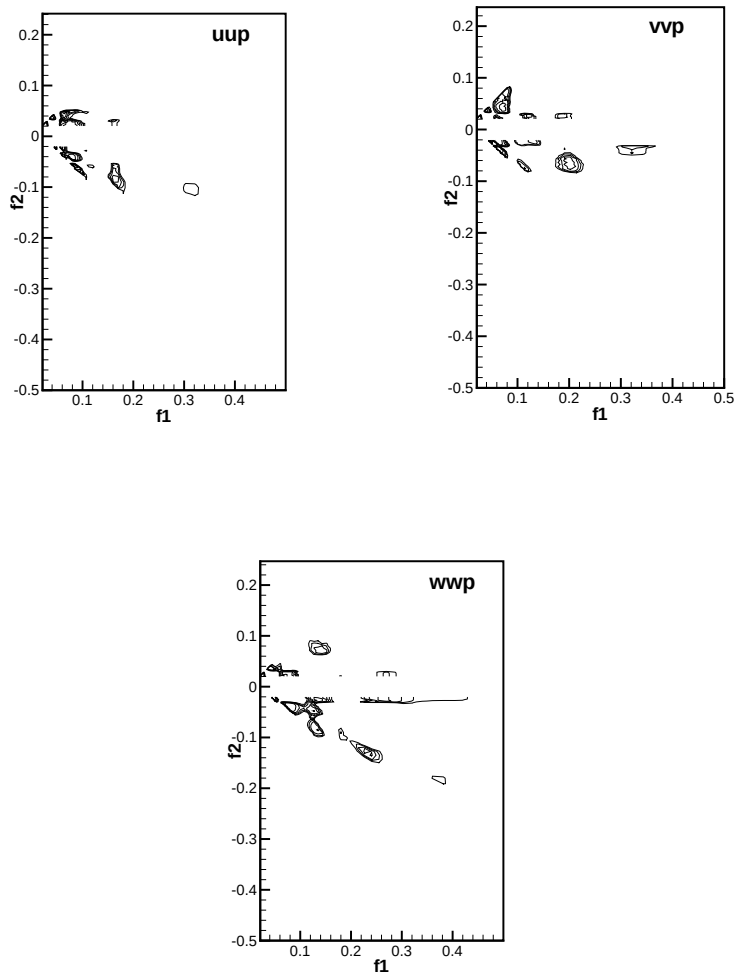

Figure 6.37: Wavelet cross-bicoherence between velocity vectors (Z/H=1.18090) and pressure (Z/H=1.01), time of integration=2.36:30.68. Contour levels are set at 0.7, 0.7625, 0.825, 0.8875, 0.95

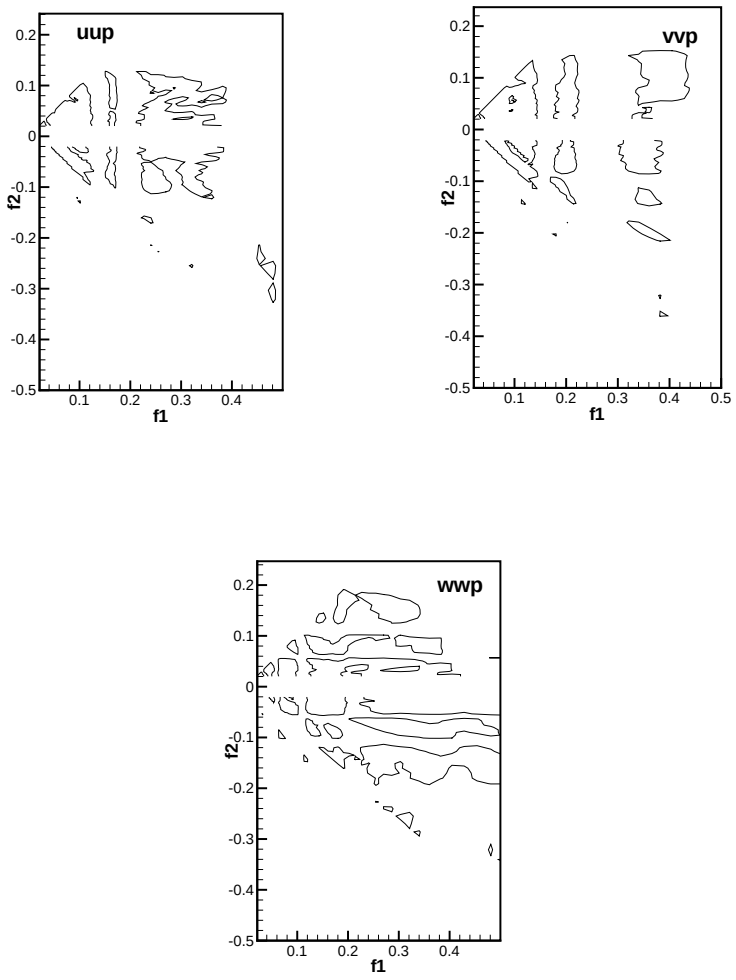

Figure 6.38: Wavelet cross-bicoherence between velocity vectors (Z/H=1.18090) and pressure (Z/H=1.01), time of integration=7.08:14.16. Contour level is set at 0.90

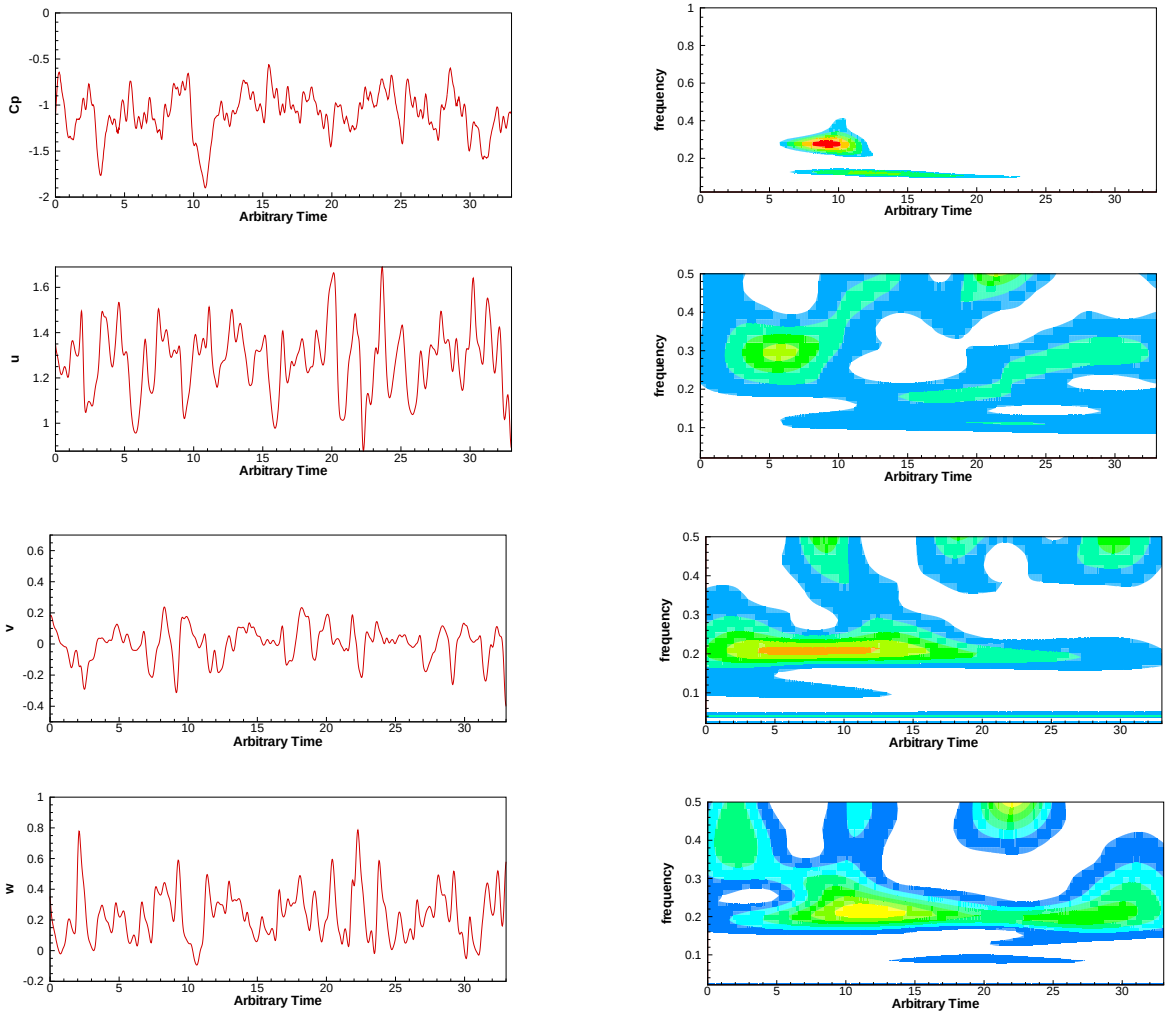

Figure 6.39: Pressure (Z/H=1.01) and velocity field (Z/H=1.65613) and their wavelet transforms. Contour levels are set at 4, 4.833, 6.667, 6.5

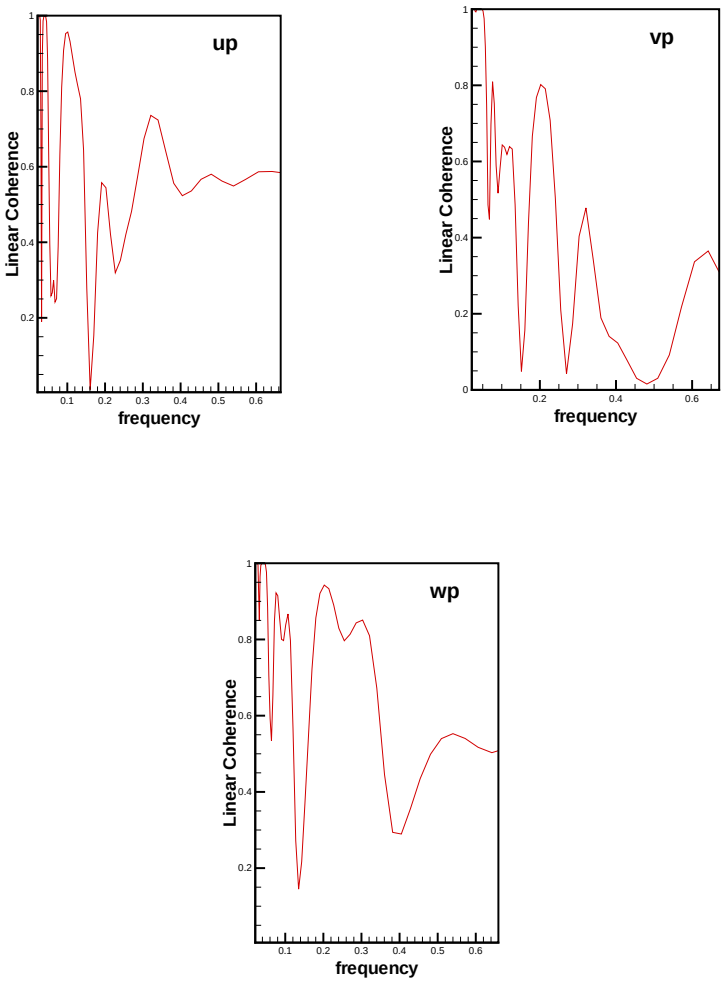

Figure 6.40: Wavelet linear coherence between velocity vectors (Z/H=1.65613) and pressure (Z/H=1.01), time of integration=2.36:30.68

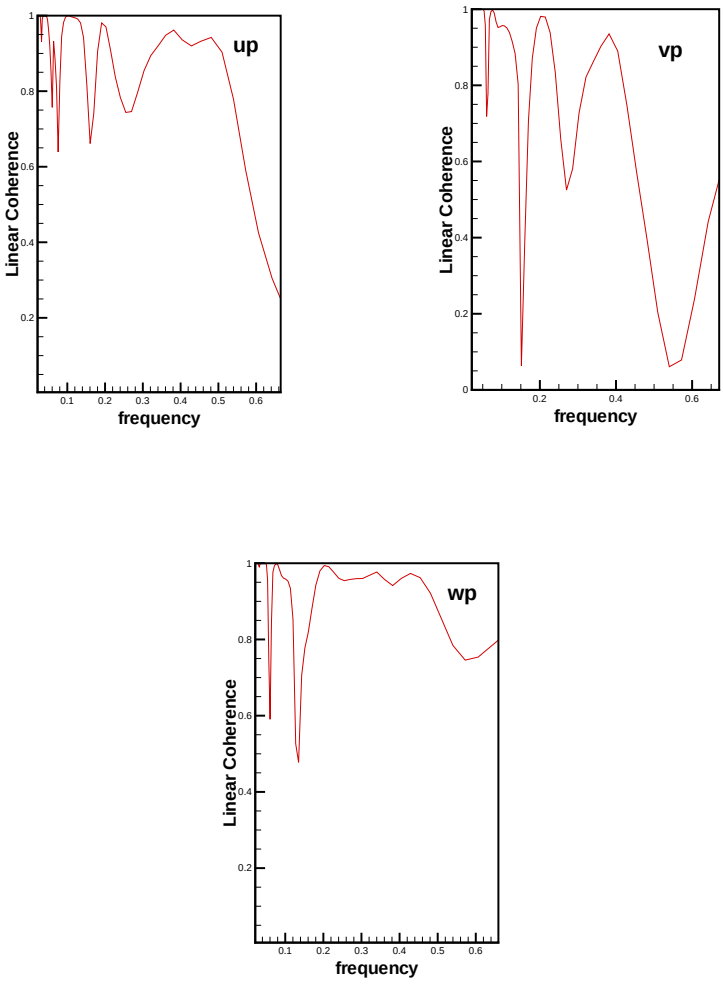

Figure 6.41: Wavelet linear coherence between velocity vectors (Z/H=1.65613) and pressure (Z/H=1.01), time of integration=7.08:14.16

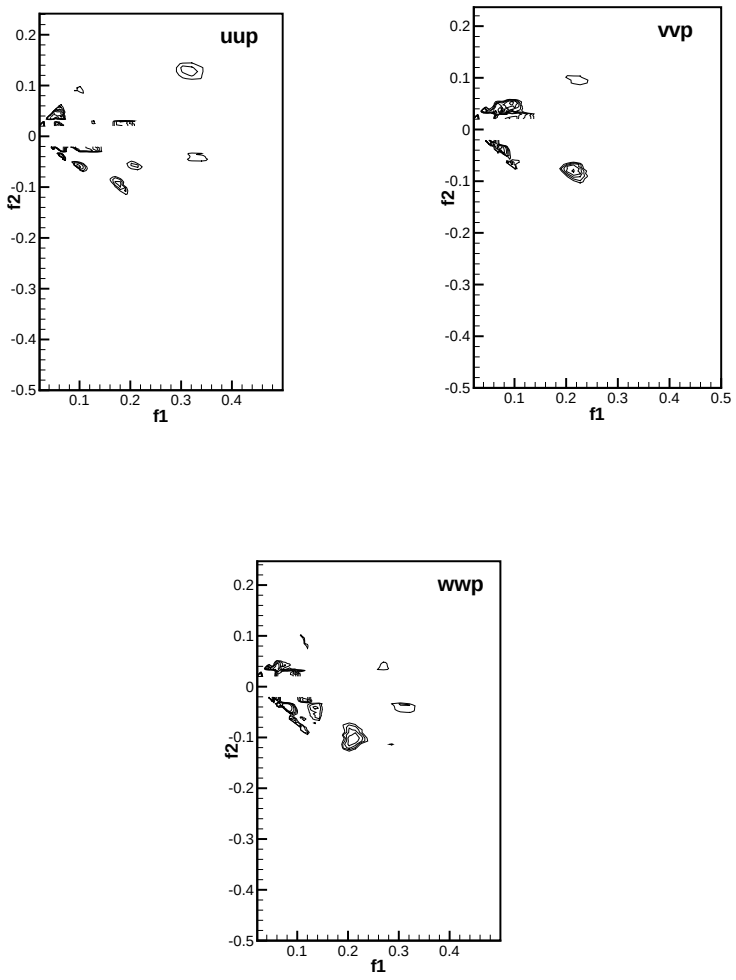

Figure 6.42: Wavelet cross-bicoherence between velocity vectors (Z/H=1.65613) and pressure (Z/H=1.01), time of integration=2.36:30.68. Contour levels are set at 0.7, 0.7625, 0.825, 0.8875, 0.95

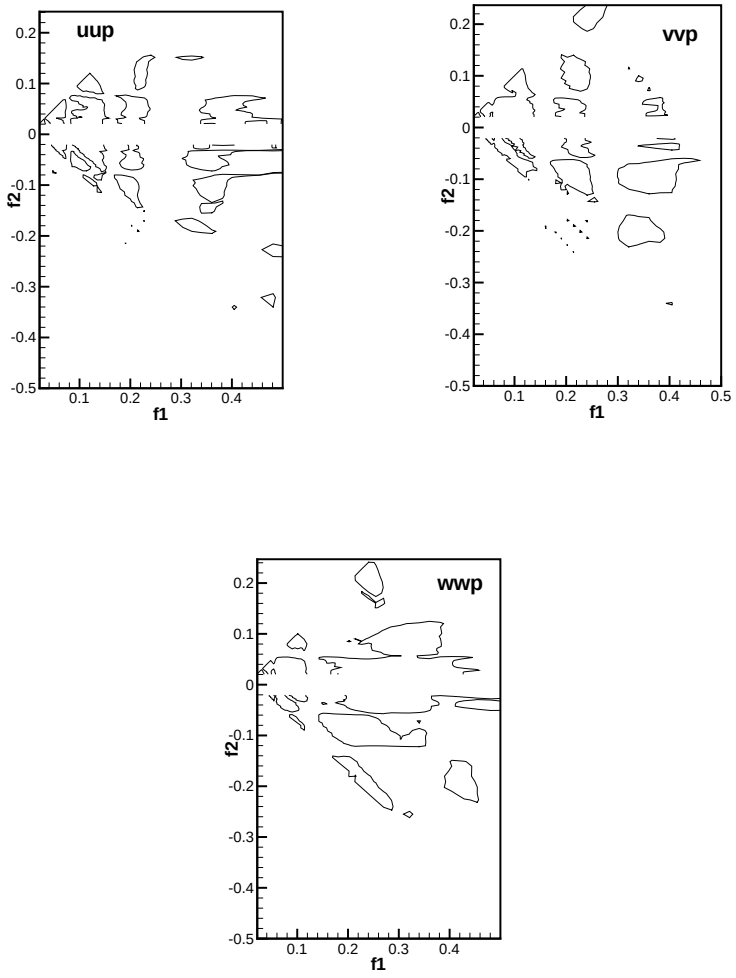

Figure 6.43: Wavelet cross-bicoherence between velocity vectors (Z/H=1.65613) and pressure (Z/H=1.01), time of integration=7.08:14.16. Contour level is set at 0.90

Next, the linear and quadratic relation between the surface pressure and the outer field is examined. As such time series along with wavelet scalograms of the pressure fluctuations are presented in figure 6.44. The time series of v- and w- velocity fluctuations show periodic variations with two distinctive frequencies. The wavelet scalogram show a low frequency component around 0.1 in all time series and higher ones near 0.2 and 0.25 in the u- and v-components and near 0.4 in the w- component. The linear coherence plots estimated from

the full record and plotted in figure 6.45 show high levels of coherence in the frequency ranges near 0.1, 0.2 and 0.3 between the surface pressure and velocity fluctuations. As the time of integration is decreased to only cover the part of the time series that includes the peak, the linear coherence analysis shows higher levels of coupling among previously noted components along with a high level near 0.4; particularly for the linear coherence between the pressure and w-component (see figure 6.46). The cross-bicoherence plots presented in figure 6.47 and obtained over the full record show high level of quadratic coupling between the frequency components in the ranges near 0.3,0.2 and 0.1, especially in the difference region. This implies a coupling whereby low frequency components in the pressure fluctuations are enhanced by interaction of higher frequency components in the velocity fluctuations. Of particular interest, however, is the interaction over the range of frequencies in the w- component of velocity fluctuations between 0.42 and -0.18 which yields coupling with the frequency range near 0.25 in the surface pressure fluctuations. This mechanism is very important because it was not clearly observed when considering the coupling between the near flow field and the surface pressure fluctuations.

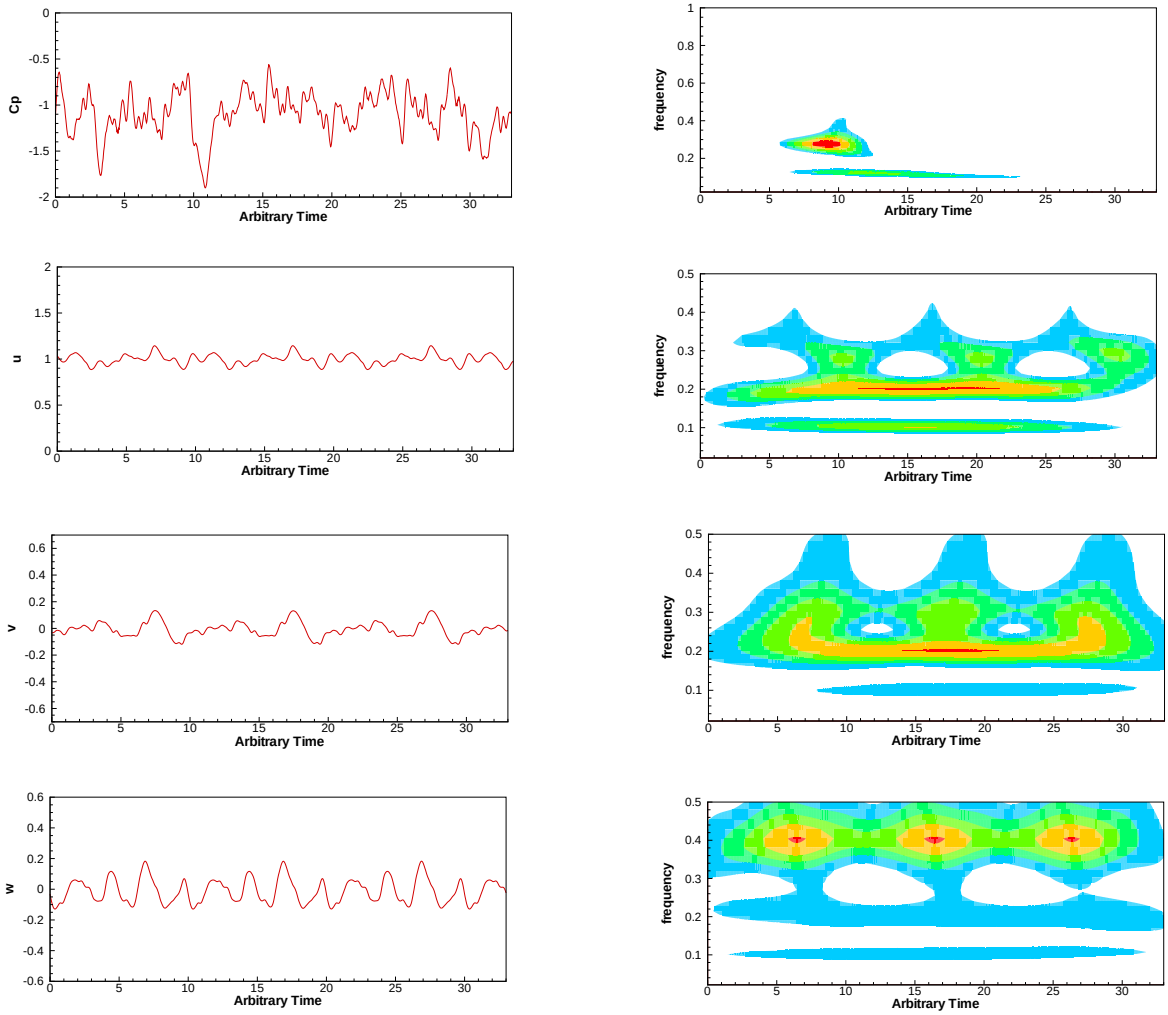

Figure 6.44: Pressure (Z/H=1.01) and velocity field (Z/H=7.00613) and their wavelet transforms. Contour levels are set at 4, 4.833, 6.667, 6.5

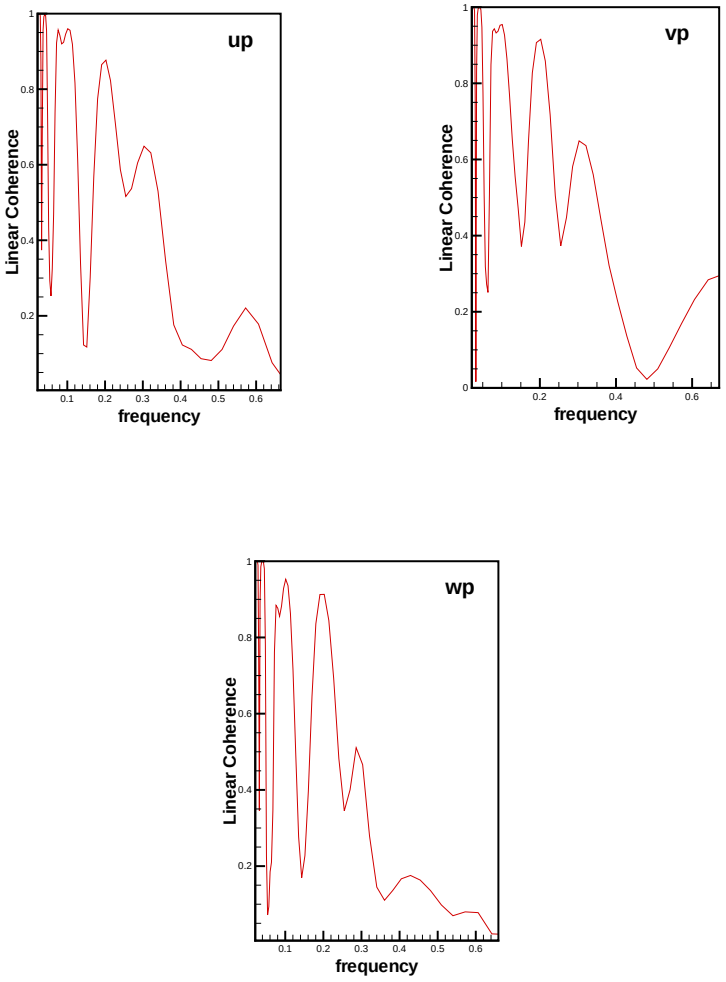

Figure 6.45: Wavelet linear coherence between velocity vectors (Z/H=7.00613) and pressure (Z/H=1.01), time of integration=2.36:30.68

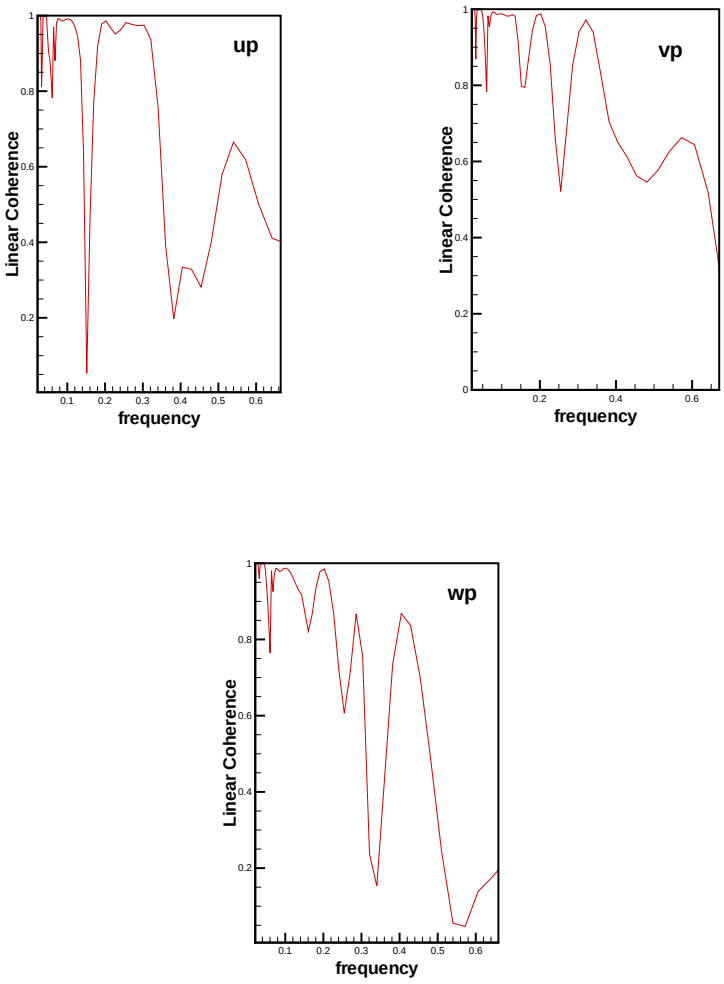

Figure 6.46: Wavelet linear coherence between velocity vectors (Z/H=7.00613) and pressure (Z/H=1.01), time of integration=7.08:14.16

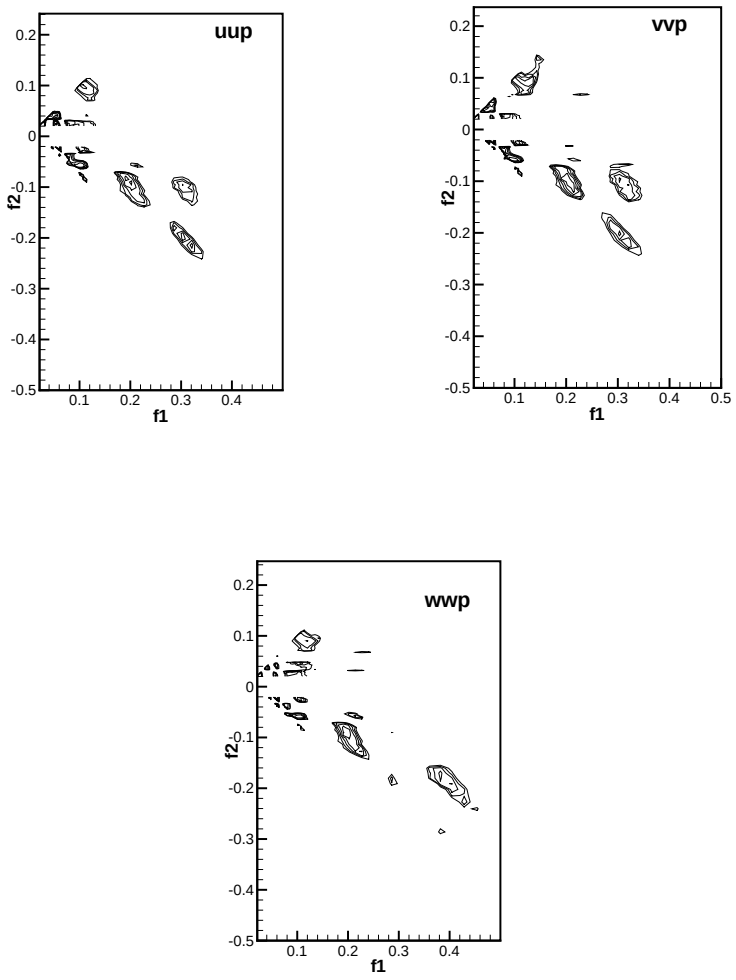

Figure 6.47: Wavelet cross-bicoherence between velocity vectors (Z/H=7.00613) and pressure (Z/H=1.01), time of integration=2.36:30.68. Contour levels are set at 0.7, 0.7625, 0.825, 0.8875, 0.95

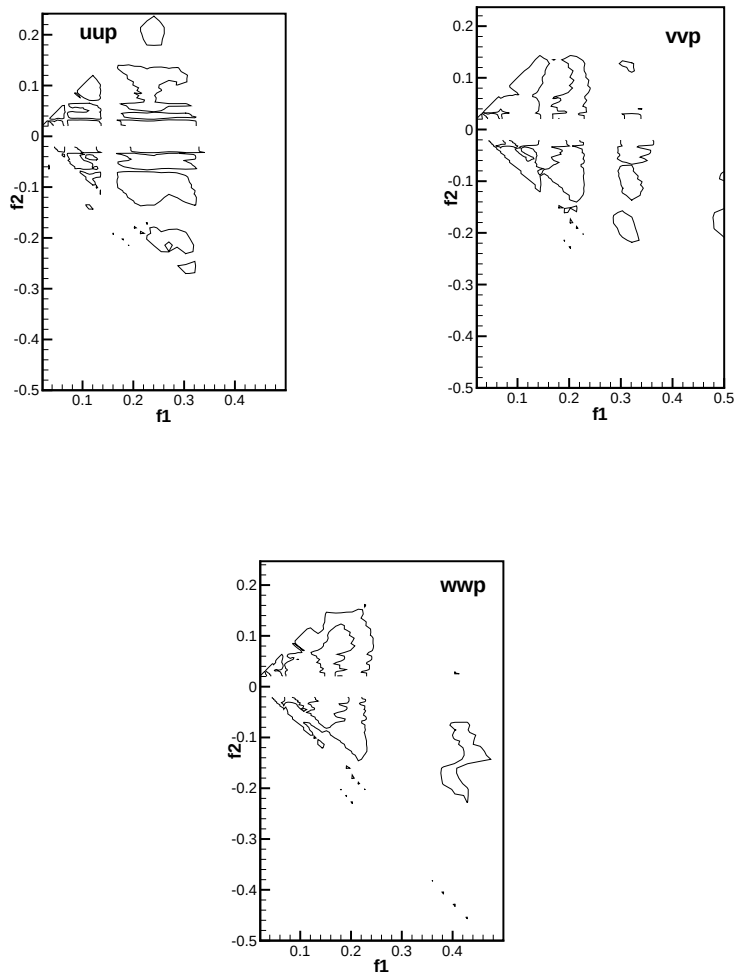

Figure 6.48: Wavelet cross-bicoherence between velocity vectors (Z/H=7.00613) and pressure (Z/H=1.01), time of integration=7.08:14.16. Contour level is set at 0.90

Chapter 7

Conclusions

In this dissertation, large-eddy simulations are conducted to study the effects of introducing homogeneous turbulence in the incident flow over a surface-mounted prism on pressure characteristics. A compact fifth-order upwind difference scheme is used to effectively and accurately perform the simulations. Three cases of incident flow are considered. In one case, the prism is placed in a smooth uniform flow. In the other two cases, homogeneous isotropic turbulence with von Karman spectrum is superimposed on the uniform flow at the inflow boundary. In one of these cases, the integral length scale of the incoming turbulence is set at one-half the prism height. While, in the second case, the integral length scale is set equal to the prism height. Velocity and pressure fluctuations data from the numerical simulations are used to determine the linear and nonlinear relations between the different scales in the flow field and the scale that characterizes the pressure peaks as observed.

The numerical results are compared with experimental measurements reported by Tieleman et al.[11]. The results show that the highest negative mean value of the pressure coefficient on the roof and the sides is about 30 % larger in case two of turbulent inflow and takes place closer to the windward edge of the prism. Moreover, the pressure coefficients on the roof and sides of the prism in the case of turbulent inflow show a higher level of variations in comparison with the case of smooth inflow conditions. The predicted mean characteristics

of the pressure coefficients in the turbulent case match the experimental values in terms of both magnitude and location on the roof of the prism reported in Tieleman et al.[38] and Tieleman et al.[11].

As for the peak value, the peak value of -2 obtained in the turbulent inflow case two is about 20% smaller than the values measured experimentally. On the other hand, it is stressed that the peak value in the simulations would increase as the duration of the simulation is increased to match that of the experimental measurement. The results also show that the turbulent case yields a non-exceedence probability for the peak pressure coefficient that is closer to the one obtained from the measured data than the smooth case data.

The wavelet-based analysis of the linear and nonlinear relations between the three components of the velocity fluctuations at different points in the near flow field and surface pressure fluctuations reveals a linear relation with the u- component and a nonlinear relation with the w- component.

Bibliography

[1] Y. Dahai and A. Kareem, Two-dimensional simulation of flow around rectangular prisms, *Journal of wind engineering and industrial aerodynamics*, 62, 131-161, 1996.

[2] Y. Dahai and A. Kareem, Numerical simulation of flow around rectangular prism, *Journal of wind engineering and industrial aerodynamics*, 67 & 68, 195-208, 1997.

[3] Y. Dahai and A. Kareem, Parametric study of flow around rectangular prisms, *Journal of wind engineering and industrial aerodynamics*, 77 & 78, 653-662, 1998.

[4] S. Kawamoto, Improved turbulence models for estimation ofwind loading, *Journal of wind engineering and industrial aerodynamics*, 67 & 68, 589-599, 1997.

[5] T.G. Thomas and J.J.R. Williams, Large eddy simulation of vortex shedding from cubic obstacle, *Journal of Aerospace Engineering*, 12, 113-121, 1999.

[6] K. Nozawa and T. Tamura, Large eddy simulation of the flow around a low-rise building in a rough-wall turbulent boundary layer, *Journal of wind engineering and industrial aerodynamics*, 90, 1151-1162, 2002.

[7] T. Tamura and Y. Ono, LES analysis on aeroelastic instability of prisms in turbulent flow, *Journal of wind engineering and industrial aerodynamics*, 91, 1827-1846, 2003.

[8] K. C. Kim, H. S. Ji, and S. H. Seong, Flow structure around a 3-D rectangular prism in a turbulent boundary layer, *Journal of wind engineering and industrial aerodynamics*, 91, 653-669, 2003.

[9] M. Yamada, Y. Uematsu, and R. Sasaki, A visual technique for the evaluation of the pedestrain-level wind environment around buildings by using infrared thermography, *Journal of wind engineering and industrial aerodynamics*, 65, 261-271, 1996.

[10] P. P. Vlachos and M. R. Hajj, A time-resolved DPIV study of the unsteady character of the flow over a surface-mounted prism, *Journal of wind engineering and industrial aerodynamics*, 90, 543-553, 2003.

[11] H. W. Tieleman, Z. Ge, M. R. Hajj, T. A. Rienhold, Pressures on a surface-mounted rectangular prism under varying incident turbulence, *Journal of wind engineering and industrial aerodynamics*, 90, 1095-1115, 2003.

[12] H. W. Tieleman, Wind tunnel simulation of wind loading on low-rise structures: a review, *Journal of wind engineering and industrial aerodynamics*, 90, 1627-1649, 2003.

[13] M. R. Hajj, I. M. Janajreh, H.W. Tieleman, and T. A. Rienhold, On frequency-domain analysis of the relation between incident turbulence and fluctuating pressures, *Journal of wind engineering and industrial aerodynamics*, 69 & 71, 539-545, 1997.

[14] H. W. Tieleman, M. R. Hajj, I. M. Janajreh, T. A. Rienhold, and C. P. W. Geurts, Velocity-pressure correlation in stagnation and separation regions on surface-mounted prisms, *Journal of wind engineering and industrial aerodynamics*, 77 & 78, 567-578, 1998.

[15] M. R. Hajj, H. W. Tieleman, L. Tian, Wind tunnel simulation of time variations of turbulence and effects on pressure on surface-mounted prisms, *Journal of wind engineering and industrial aerodynamics*, 88, 197-212, 2000.

[16] G. Erlebacher, M. Y. Hussaini, C. G. Speziale, and T. A. Zang, Toward the large eddy simulation of compressible turbulent flows, *Journal of fluid mechanics*, 238, 155-185, 1992.

[17] S. A. Ragab, and S. Sheen, *Large Eddy Simulation of a Mixing Layer: Large Eddy Simulation of Complex Engineering and Geophysical Flows*, B. Galperin, and S. A. Orszag (Editors), Cambridge University Press, Cambridge, 1993.

[18] J. Smagorinsky. General circulation experiments with the primitive equations. I. The basic experiment. *Monthly Weather Review*, 91(3),99-163, 1963.

[19] M. Germano, Ugo Piomelli, P. Moin, and W. H. Cabot. A dynamic subgrid-scale eddy viscosity model. *Physics of Fluids*, 3(7),1760-1765, 1991.

[20] P. Moin, K. Squires, W. Cabot, and S. Lee. Dynamic subgrid-scale model for compressible turbulence and scalar transport. *Physics of Fluids*, 3(11),2746-2757, 1991.

[21] D. K. Lilly. A proposed modication of the germano subgrid-scale closure method. *Physics of Fluids*, 4(3),633-635, 1992.

[22] W. Zhang and Q. Chen. A new ltered dynamic subgrid-scale model for large eddy simulation of indoor airow. *Proceedings of Building Simulation '99*, Kyoto, Japan, 1999.

[23] W. Zhang and Q. Chen. Large-eddy simulation of indoor airow with a l- tered dynamic subgrid scale model. *International Journal of Heat and Mass Transfer*, 43(17),3219-3231, 2000.

[24] W. Zhang and Q. Chen. Large eddy simulation of natural and mixed convection airow indoors with two simple ltered dynamic subgrid scale models. *Numerical Heat Transfer, Part A : Applications*, 37(5),447-463, 2000.

[25] M. P. Martin, U. Piomelli, and G. V. Candler. Subgrid-scale models for compressible large-eddy simulations. *Theoretical and Computational Fluid Dynamics*, 13,361-376, 2000.

[26] P.A. Durbin, and B.A.P. Reif. Statistical Theory and Modeling for Turbulent Flows, *John Wiley, Sons Ltd.*, 2001.

[27] J. Jeong, and F. Hussain. On the Identification of a Vortex, *Journal of Fluid Mechanics*, 285, 69-94, 1995.

[28] A.I. Tolstykh. High Accuracy Non-Centered Compact Difference Schemes For Fluid Dynamics Applications, *World Scientific*, 1994.

[29] M.H. Carpenter, and C.A., Kennedy. Fourth-Order, 2N-Storage Runge-Kutta Schemes, *ICASE, NASA Langley Research Center, NASA TM 109112*, 1994.

[30] Y. M. El-okda. *Experimental and Numerical Investigations of the Effects of Incident Turbulence on the Flow over a Surface-mounted Prism*. Blacksburg, VA,USA, Virginia Polytechnic Institute and State University, Ph.D. Dissertation, 2005.

[31] C. Torrence and G.P. Compo, G.P., A practical guide to wavelet analysis., *Bulletin of the American Meteorological Society*, 79, 61-77, 1998.

[32] P.S. Addison. *The Illustrated Wavelet Transform Handbook: Introductory Theory and Applications in Science*. Bristol, UK, Institute of Physics Publishing, 349page, 2002.

[33] J., Morlet. Sampling theory and wave propagation. *Proceedings of the 51st Annual Meeting of the Society of Exploration Geophysics*, (Los Angeles, USA), 1981.

[34] M., Farge. Wavelet transforms and their application to turbulence. *Annual Review of Fluid Mechanics*, 24, pages 395-457, 1992.

[35] B.P.V, Milligen, E., Sanchez, T., Estrada,C., Hidalgo, B., Branas, B., Carreras, and L., Garcia. Wavelet bicoherence: A new turbulence analysis tool. *Physics of Plasmas*, 2,pages 3017-3032, 1995.

[36] B.P.V., Milligen, C., Hidalgo, E., Sanchez, M.A., Pedrosa, R., Balbin, I., Garcia-cortes, and G.R., Tynan. Statistically robust linear and nonlinear wavelet analysis applied to plasma edge turbulence. *Review of science Instruments*, 68,pages 967-970, 1997.

[37] M.R., Hajj, D.A., Jordan, and H.W., Tieleman. Analysis of atmospheric wind and pressures on a low rise building. *Journal of Fluids and Structures*, 12,pages 537-547, 1998.

[38] H. W. Tieleman, M.A.K. Elsayed, Z. Ge, M. R. Hajj, Extreme Value Distributions for Peak Pressure and Load Coefficients, *Journal of wind engineering and industrial aerodynamics*, submitted for review, 2005.

[39] H. W. Tieleman, M. R. Hajj, T.A. Reinhold, Wind Tunnel Simulation Requirements to Assess Wind Loads on Low-rise Buildings, *Journal of wind engineering and industrial aerodynamics*, 74-76,pages 675-685, 1998.

[40] F. Sadek, and E. Simiu, Peak Non-Gaussian Wind Effects for Data-Base-Assisted Low-rise Building Design, *Journal of Engineering Mechanics*,5, pages 530-539, 2002.

[41] M. Grigoriu, Applied Non-Gaussian Processes, *Englewood Cliffs*, Prentice Hall, New Jersy, 1995.

[42] M. Gioffre, M. Grigoriu, M. Kasperski, and E. Simiu, Wind-induced Peak Bending Moments in Low-rise Building Frames, *Journal of Engineering Mechanics*,126, pages 879-881,2000.

Vita

Mohamed Aly Khamis Elsayed comes from Egypt. He completed his primary, secondary and pre-university education in Alexandria, Egypt. After receiving his B.Sc. degree in Civil Engineering from Alexandria University in Egypt, he worked as a coastal engineer in the Egyptian shore protection authority and enrolled in a part-time master's degree program at Alexandria University, Egypt. He obtained his second master in coastal engineering from IHE, Delft, The Netherlands in April 1999. He began his PhD. program in Engineering Mechanics in the Department of Engineering Science and Mechanics at Virginia Tech in Spring 2003. He will return to Egypt after completing his PhD. program.